The Dissertation Committee for Thomas Charles Brothers certifies that this is the approved version of the following dissertation:

Morphology of the Planum Boreum basal unit, Mars, and constraints on the origin and timing of icy circumpolar deposits

Committee:

John W. Holt, Supervisor

Lesli J. Wood

Kenneth Tanaka

Gary Kocurek

David Mohrig

Morphology of the Planum Boreum basal unit, Mars, and constraints on the origin and timing of icy circumpolar deposits

by

Thomas Charles Brothers, B.A.

Dissertation

Presented to the Faculty of the Graduate School of

The University of Texas at Austin

in Partial Fulfillment

of the Requirements

for the Degree of

Doctor of Philosophy

The University of Texas at Austin

May 2015

Acknowledgements

The work presented in this dissertation took more energy and time to produce than I had imagined. Without a strong support network I don't know that I would have been able to remain focused and scientifically rigorous. There is no specific order to these acknowledgements, only genuine appreciation. I would first like to thank Isaac Smith. As my officemate and fellow Jack Holt student, the two of us were able to share many of the same joys and sorrows. Isaac and I never approached a problem the same way and that is perhaps why we made a strong office duo. While our different approach to martian science was helpful, it resulted in several hour long heated discussions about planetary processes and ultimately helped me to understand my research.

I would also like to thoroughly thank my wife Sarah. Writing does not always come easy and she was able to help me with that struggles. Thank you for your editing, your input, and your inquisitive nature. I would also like to recognize and thank my advisor Jack Holt. As a young graduate student I had him working to edit some horrendous Lunar and Planetary Science Conference abstracts. Perhaps the best part was that in my ignorance I took offense to the editing process and tried to prove my methods were superior. It took several years for me to appreciate Jack's editing, it was different from the type of editing I had grown accustomed to as an undergraduate, but was invaluable. My work is much stronger now as a result of verbal and written interaction with Jack. Thank you both for helping me progress.

In addition to scientific help it would be unfair to not mention the amazing staff support given to students at the University of Texas Institute for Geophysics (UTIG). Compliments of Mark Wiederspahn and Scott Kempf I have never once been without

computer support. These two keep the system running for the cryosphere researchers at UTIG. Trips were virtually handled for me, visiting scientist accommodations were arranged as well. Provided I had an account number for the bills Stephanie Jackson and the UTIG staff took care of the arrangements. Additionally, unlike a few of my colleagues I never once missed an appointment deadline with the university thanks to the work of Judy Sansom. Philip Guerrero is also perhaps the best graduate student coordinator I could ask for. I cannot count the number of emails and questions I have asked Philip, all of which were replied to. I know I missed several names, but the staff at both UTIG and within the department have made my degree experience at UT Austin much more enjoyable.

As a final note I would like to thank my family. My sister and mother provided me with endless hours of phone support. The two of you have helped me more than I can adequately express. While I cannot always thank you for the situations you bring into my life, I can thank you for all of the experiences that we have shared. Thank you. Without the support network of staff, friends, advisor and family this might have been a lonely and difficult seven years. While it was certainly difficult, I did not once suffer from a lack of support. I am very thankful for all of the help and support that allowed me to complete this project.

Morphology of the Planum Boreum basal unit, Mars, and constraints on the origin and timing of icy circumpolar deposits

Thomas Charles Brothers, Ph.D.

The University of Texas at Austin, 2015

Supervisor: John W. Holt

Data from the Shallow Radar instrument on Mars Reconnaissance Orbiter have enabled detailed scientific exploration of martian ice. Orbital ground penetrating radar enabled scientists to study subsurface ice stratigraphy, to uncover the geologic structure of ice on Mars with remarkable results for the north pole. On the north pole of Mars sits a massive, approximately two kilometer thick, deposit of pure water ice. This deposit is underlain with a sand and ice mixture that reaches 1.5 km maximum thickness. This dissertation examines the nature of the old sand/ice mixture on Mars' north pole. We use this ice to identify early trends in deposition and erosion on Mars' north pole and ultimately to link ice rich deposits that are not part of the polar cap. This multi-part study endeavors to understand and constrain the drivers of Mars' polar ice deposition. With careful stratigraphic analysis we hypothesize that depositional regime has not changed drastically since the upper part of the sand and ice mixture was emplaced in Middle Amazonian time. Sediment supply became limited and ice more plentiful with respect to sand; however, deposition remained aeolian in nature.

Additionally, our work finds evidence that circumpolar landforms are related to the central mass of ice on Planum Boreum. We present evidence supporting a coeval evolution of the circumpolar deposits and central Planum Boreum. We also present

evidence that refutes these features being part of a more extensive ancient ice cap. This indicates that the processes occurring at Planum Boreum are likely mirrored in nearby landforms such as small craters and isolated ice wedges. This is fundamental to polar science, the processes occurring on Planum Boreum and the processes responsible for deposition of the north polar layered deposits can be analyzed at additional locations. Furthermore, we find that if a climate signal exists in the ice deposits, as has been postulated, these circumpolar features are likely to contain the same climate signal as the central ice cap. Thus, this work unifies the complexity of martian polar processes and suggests future avenues of research.

Table of Contents

List of Tables

List of Figures

INTRODUCTION

This dissertation is a detailed study of martian polar ice. Since before the influx of Viking I orbital data, martian polar ice has been hypothesized to contain a record of the planet's climate signal [*Cutts*, 1973]. More specifically it has been theorized that accumulation patterns, and therefore stratigraphy, will respond to Milanković orbital cycles: obliquity, eccentricity, and precession. While this work does not attempt to reconstruct climate, it does analyze ice stratigraphy both on Planum Boreum and in nearby circumpolar deposits. A primary goal of this work is to understand the relationship between circumpolar ice and Planum Boreum. We attempt to ascertain the relationship between depositional processes on and away from Planum Boreum. The study also as investigates an older ice unit, attempting to uncover evidence for a climate shift within this older deposit's morphology and stratigraphy.

The study of Mars' polar ice has been punctuated by new mission data. As additional instruments are launched into orbit around Mars, new perspectives that weren't previously possible are introduced. Great advances in scientific understanding were made with the imagery provided by Viking 1 launched in 1975, including the reiteration that martian climate signal may in fact be preserved in the polar layered deposits on Mars north pole [*Cutts*, 1973; *Cutts and Lewis*, 1982; *Howard et al*., 1982]. In search of a climate signal, polar stratigraphic work has continued to the present. While the work performed by this study does not directly investigate the purported existence of a climate signal, it does carefully analyze depositional patterns and resulting morphology and

stratigraphy in order to provide new constraints on Mars' ice. It is hoped that these constraints will aid understanding of martian polar conditions, climatologically and sedimentologically, both ancient and modern, by providing critical context and a new understanding of the processes involved in the deposition and erosion of polar ice.

Modern Mars' polar science has most recently benefited immensely from the use of orbital radar sounders. Two such instruments have been sent to Mars. The first was Mars Advanced Radar for Subsurface and Ionospheric Sounding (MARSIS) on Mars Express, and the second was Shallow Radar (SHARAD) on Mars Reconnaissance Orbiter. These two instruments are similar, but different enough to enable unique science accomplishments. MARSIS is a lower bandwidth and lower operating frequency radar sounder while SHARAD has a larger bandwidth and higher operating frequency [*Picardi et al*., 2004; *Seu et al*., 2007]. This results in SHARAD having a higher resolution but less depth of penetration when compared to MARSIS. However, both of these radars established subsurface exploration on Mars with promising results over ice deposits. In particular, the radar data returned from Mars' north pole has shown us a wealth of complexity in the ice stratigraphy [*Phillips et al*., 2008; *Putzig et al*., 2009; *Holt et al*., 2010; *Smith and Holt*, 2010], verified that the north polar layered deposits (NPLD) are greater than 95% water ice [*Grima et al*., 2009], and allowed rheology calculations indicating a very thick, approximately 400 km, crust [*Phillips et al*., 2008].

The work in this dissertation analyzes the stratigraphy of both Planum Boreum and two circumpolar ice-rich deposits; however, instead of focusing on the recent pure water ice, we shift focus to an older unit, called the basal unit (BU), which is a mixture of

sand and ice. Stratigraphically, this unit is below the pure water ice and is representative of an older depositional environment, one in which abundant sand was mobile and accumulating in a martian polar erg. The decision to study the more ancient ice mixture is based on our goal of constraining ice deposition patterns and process. In order to understand modern polar depositional environment, one must first have an understanding of the processes that gave rise to current conditions. Hence, knowledge of the BU morphology, extent, and any variations that exist are crucial for constraining the transition to modern ice deposition.

This work will be presented in three chapters. The first chapter will focus on a large mapping effort using SHARAD orbital radar coverage to reveal the buried morphology of the BU. The BU work operates as the foundation for proceeding chapters. Conveniently, the BU is also the oldest feature analyzed in this dissertation and therefore comes first chronologically. Results from the interpretation and modeling of the basal unit deposit are used to constrain depositional processes occurring for ancient Planum Boreum and early north polar layered deposits.

Following the large-scale basal unit study are two chapters focusing on smaller features. The second chapter analyzes Abalos Mensa (Figure 1), a wedge of ice material nearby but offset from Planum Boreum, completely isolated. As this feature is proximal to Planum Boreum it is expected to have similar, if not identical, ice deposits. We use multiple data sources and analysis techniques to assess the origin

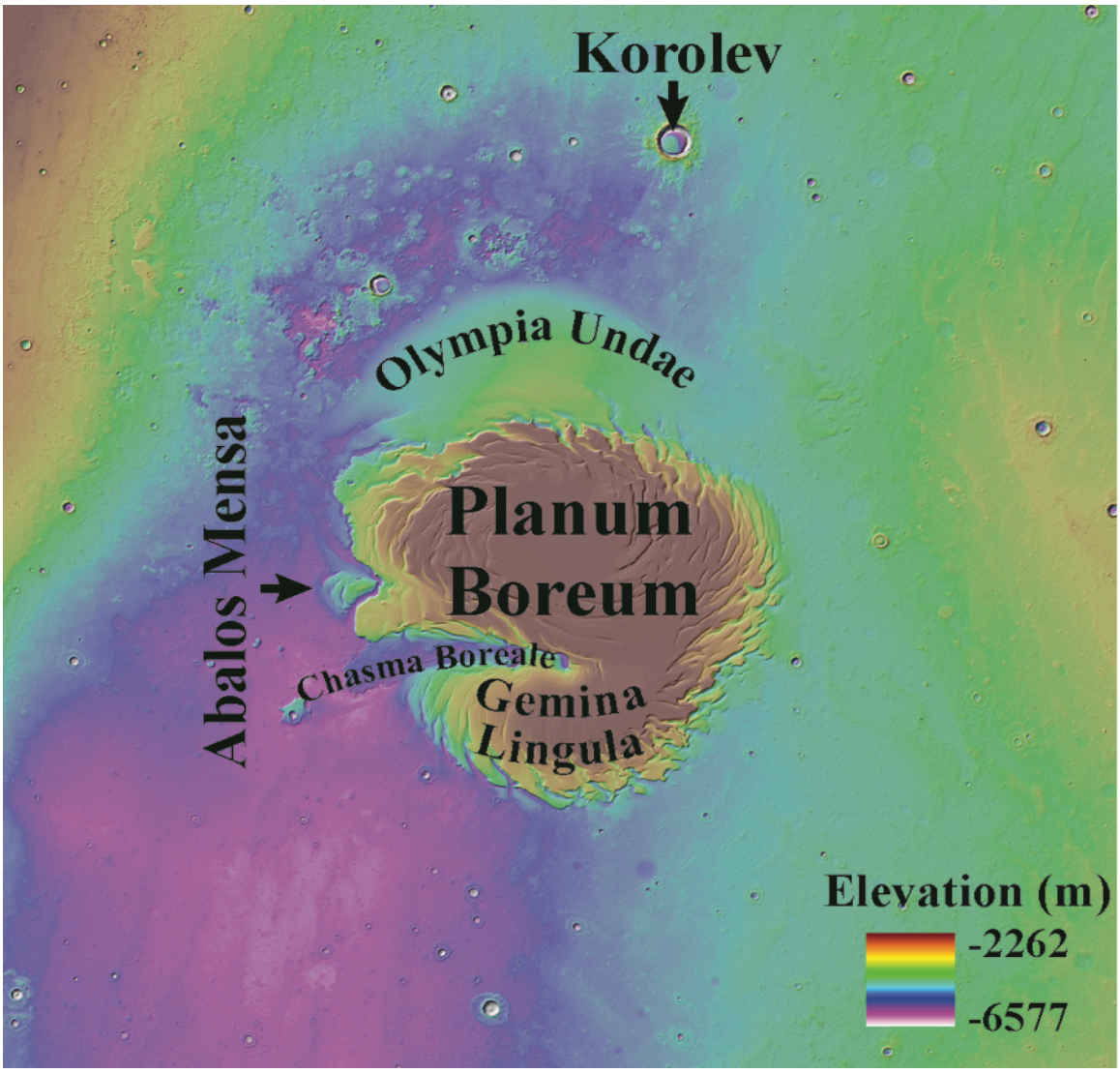

Figure 1. Mars Orbiter Laser Altimeter color shaded elevation map of Mars' north pole. Large features of interest have been labeled.

of this circumpolar feature. Abalos Mensa offers a unique opportunity to investigate how an ice rich deposit adjacent to Planum Boreum can be isolated. This deposit also offered an opportunity to apply BU results to a circumpolar feature.

The last chapter of this dissertation moves farther away from the pole. We study Korolev crater using the same methodology employed for Abalos Mensa. While Abalos

Mensa is only a few kilometers separated from Planum Boreum, Korolev is approximately 600 km south at 72.7° N 164.5° E. The crater itself contains a large central mound of water ice [*Armstrong et al*., 2005; *Conway et al*., 2012] and has layered stratigraphy reminiscent of the north polar layered deposits on Planum Boreum. However, there has been no link made between Planum Boreum's and Korolev's icy deposits. The origin of the ice in Korolev is still unknown. Using SHARAD we analyze the stratigraphy of that ice and make comparisons with Planum Boreum. The SHARAD stratigraphy allows us to infer how water ice has filled Korolev crater, providing data to analyze both a regional ice sheet hypothesis and an in-situ deposition hypothesis.

This dissertation attempts to establish a link between widely separated water-ice features on Mars' north pole. From Planum Boreum to Abalos Mensa and Korolev we will assess similarities in depositional style, thickness and radar-derived stratigraphy. Each of the features analyzed in this study is presented as an independent chapter in the dissertation; however, it is the relationship between all three chapters that provides context for the timing of ice deposition and the relationship of seemingly disparate deposits.

Chapter 1: Planum Boreum basal unit topography, irregularities and insight from SHARAD[1]

1.1 INTRODUCTION

The "basal unit" (BU) is a low albedo, sand and ice deposit on the north pole of Mars [*Malin and Edgett*, 2001; *Byrne and Murray*, 2002] that lies stratigraphically between the Vastitas Borealis Formation below and the relatively pure water ice north polar layered deposits (NPLD) above [*Grima et al*., 2009]. Here we use data from the Shallow Radar (SHARAD) on Mars Reconnaissance Orbiter to analyze the morphology and extent of the BU in order to better understand the deposit and its implications for climate. Where prior investigations focused on the homogeneity of BU material [*Byrne and Murray*, 2002; *Fishbaugh and Head*, 2005; *Selvans et al*., 2010], this work concentrates on the inhomogeneity of this deposit to study depositional, and perhaps erosional, processes during and after BU growth. In addition, we also readdress the extent of BU material and present data supporting its continuity with Olympia Undae. Here we present the most detailed BU radar mapping to date including new, higher-resolution views of enigmatic features detected in an earlier SHARAD-based mapping effort [*Putzig et al*., 2009].

This work also provides evidence that BU topography has affected the evolution of overlying ice material via aeolian processes. This supports the interpretations of

[1] The material presented in this chapter is a modified version of a publication submitted to the Journal of Geophysical Research - Planets: Brothers, T. C., J. W. Holt, and A. Spiga (2015), Planum Boreum basal unit topography, Mars: irregularities and insights from SHARAD, Journal of Geophysical Research Planets manuscript number 2015JE004830.

Howard [2000] and recent discoveries that aeolian processes have played a critical role in the evolution of spiral troughs [*Smith and Holt*, 2010; *Smith et al*., 2013], in the growth of Abalos Mensa [*Brothers et al*., 2013] and likely in the long-term evolution of Chasma

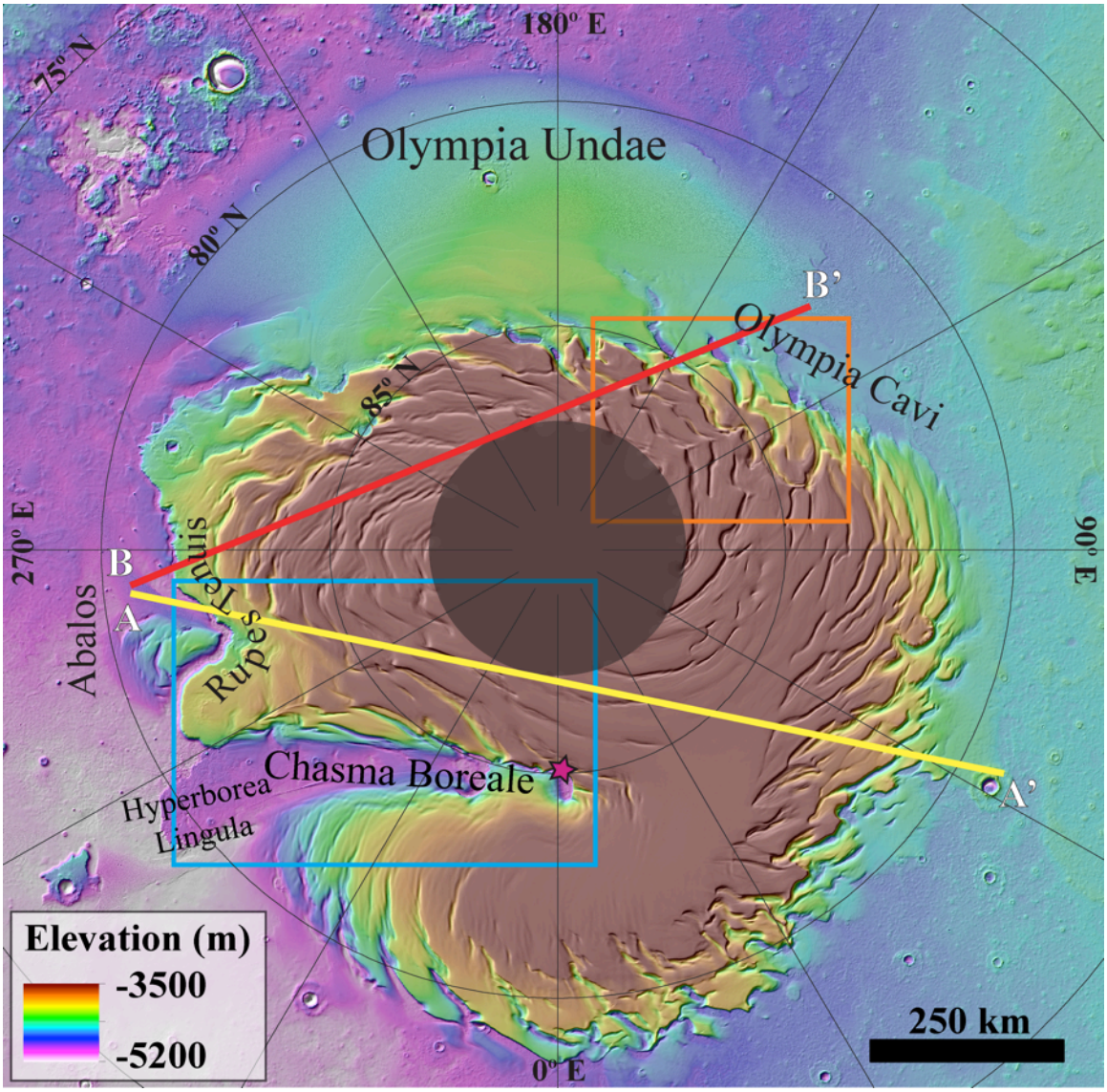

Figure 2. Color shaded elevation map of modern Planum Boreum with location for radargrams in **Figure 4** (yellow line, observation 804402000) and **Figure 6** (red line, observation 521402000). The blue box is the location for **Figure 14**a,b while the orange box is the location for **Figure 14**c,d. The magenta star in Chasma Boreale gives the location of **Figure 3**. Image is a combination of colorized MOLA topography with an overlain semi-transparent shaded-relief image.

Boreale (Figure 2) [*Holt et al*., 2010]. If the deposition of ice on Mars' north pole has been controlled by the same climatic processes from the BU epoch into the modern, then topography at the base of the deposit would have influenced winds and therefore played a strong role in the deposition of overlying ice. We therefore use our new SHARAD map of the BU topography as an input for mesoscale atmospheric modeling in order to qualitatively evaluate the depositional environment and evolution of both the BU and the early NPLD.

1.2 BACKGROUND

1.2.1 Visible Observations

An expansive deposit of low-albedo material beneath the NPLD of Mars was first revealed by Mars Orbiter Camera (MOC) [*Malin and Edgett*, 2001] and subsequent investigations indicated that this low albedo lithic- and ice-rich unit likely underlies most of the NPLD [*Byrne and Murray*, 2002; *Fishbaugh and Head*, 2005]. The material's low albedo, a stark contrast with the overlying high-albedo north polar layered deposits (NPLD) material, was the primary reason for its separation into a new geologic unit. The name "basal unit" (BU) [*Byrne and Murray*, 2002], derived from its stratigraphic position below the polar layered deposits and above the Vastitas Borealis unit.

The similarity of BU and circumpolar dune albedo spurred a hypothesis that the dune fields were sourced from the BU [*Byrne and Murray*, 2002]. This early hypothesis described the BU as a large, uniform mound of sand cemented by ice and posited that

erosion of this deposit contributed to the circumpolar dune fields. In addition, it was posited that the sand material was deposited during an ancient climate regime different from the modern regime which favors deposition of water ice [*Byrne and Murray*, 2002]. Hence, the BU material may represent a different climate than the NPLD and is therefore significant in understanding polar ice processes.

While initial BU studies only offered a generalized extent of the deposit [*Byrne and Murray*, 2002], *Fishbaugh and Head* (2005) undertook detailed image-based mapping to further resolve the aerial extent of the BU deposit, making use of data from Mars Orbiter Camera (MOC) on Mars Global Surveyor. Their analyses indicated that BU underlay nearly all of Planum Boreum, the main exception being Gemina Lingula. *Fishbaugh and Head* (2005) also discovered that the BU is locally separated from the overlying NPLD material by an unconformity that is evident as both as an angular unconformity and disconformity. This demonstrated that the BU was distinct from the overlying NPLD and not simply a transition from dust-prevalent to dust-starved ice deposition.

Following the launch of Mars Reconnaissance Orbiter (MRO) in 2005, new data were available to the scientific community by late 2006. Included on this spacecraft was a new camera with resolution approximately one order of magnitude greater than narrow angle MOC images, the High Resolution Imaging Science Experiment (HiRISE) [*McEwen et al*., 2007]. Making use of these high-resolution images, it became evident that more than one geologic unit is associated with the low albedo material underlying the

NPLD [*Herkenhoff et al*., 2007; *Tanaka et al*., 2008]. Optical mapping and careful unconformity delineation by *Tanaka et al*. (2008) divided the BU into two members, an older rupes unit and a younger Planum Boreum cavi unit (Figure 3).

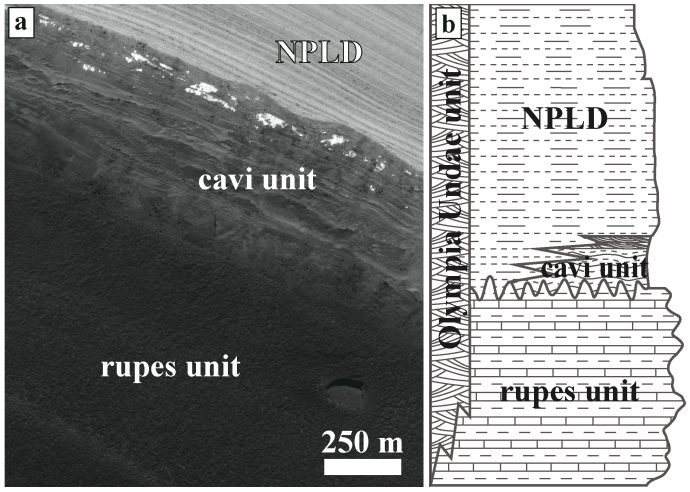

Figure 3. (a) HiRISE image ESP_0018975_2650 showing the stratigraphic units of this study. Uphill is to the right. Location is given in **Figure 2**. (b) Simplified stratigraphic column modified from the work of Tanaka et al. 2008. The two BU members (rupes unit and cavi unit) as well as the overlying north polar layered deposits are of primary interest.

The rupes unit has nearly planar bedding, a strong resistance to erosion, and can be found with outcrops exceeding 1 km thickness [*Tanaka et al*., 2008]. In contrast, the cavi unit contains aeolian bedforms including cemented dunes and cross-strata, and is highly susceptible to modern erosion and slope failure [*Herkenhoff et al*., 2007; *Russell et al*., 2008; *Tanaka et al*., 2008]. An unconformity with hundreds of meters of erosional relief [*Tanaka et al*., 2008] separates the two BU members. At the Rupes Tenuis scarp the erosional relief of the rupes unit nears 1 km. While the rupes unit appears markedly different from overlying NPLD, the cavi unit has a laterally transgressive contact with the NPLD [*Tanaka et al*., 2008]. Perhaps more accurately, the contact between cavi and NPLD can best be described as gradational with both a compositional and morphologic change. The base of the cavi unit has concentrated sandy

deposits; however, a transition from sand sheet style accumulation to dune accumulation occurs in upper cavi. Upper cavi also contains relatively pure ice layers that alternate with sandy layers. At the very top of the cavi unit the sand concentration lessens and there are examples of cemented dunes (Figure 3). Eventually both the sand and dunes disappear and a transition into NPLD is made. The gradational contact between cavi unit and overlying NPLD indicates that the large unconformity separating the two BU members is not present between cavi and NPLD. It is likely that the largest depositional hiatus in Planum Boreum's extant volatile-rich material is the gap between rupes and cavi basal unit members.

1.2.2 Age

A maximum age of ~ 1 Ga (Early Amazonian) is estimated for the rupes unit based on geologic mapping and crater density [*Tanaka et al*., 2008]. Therefore, it was deposited during early, and perhaps middle, Amazonian Mars and is the oldest volatile-rich material on Mars' north pole. The major unconformity at the top of the rupes unit represents a depositional hiatus of unknown duration and reaffirms that the overlying cavi unit is likely much younger. Additional evidence for the young age of the cavi unit come from its relative lack of preserved craters and gradational contact with the NPLD. While likely much younger than rupes unit, the cavi unit must be older than overlying NPLD based on the principle of superposition. During the past 5 million years, Mars' mean obliquity has remained relatively low, and close to that of today; however, prior to that,

average obliquity was higher [*Laskar et al*., 2004]. Ice growth models that incorporate orbital forcing are not able to accumulate lasting ice reserves at the north pole prior to the obliquity shift ~5 million years ago [*Levrard et al*., 2007; *Greve et al*., 2010]. This means that while the BU (at least the rupes unit) likely persisted for perhaps hundreds of Myr, the overlying NPLD is likely younger than 5 Ma.

1.2.3 Radar Observations

Orbital sounding radar has been able to extend geologic mapping into the subsurface, and has been shown to be effective for both polar ice and volcanic stratigraphy on Mars [*Phillips et al*., 2008; *Carter et al*., 2009; *Putzig et al*., 2009; *Holt et al*., 2010; *Morgan et al*., 2013]. In Planum Boreum, the data provide a clear contrast between the lithic-rich BU and the overlying nearly pure water-ice NPLD (Figure 4). Both SHARAD and the Mars Advanced Radar for Subsurface and Ionospheric Sounding (MARSIS) on Mars Express have successfully mapped the regional BU topography with varying degrees of coverage and precision [*Putzig et al*., 2009; *Selvans et al*., 2010]. These prior studies provide both a foundation for, and a comparison to, the work we report here.

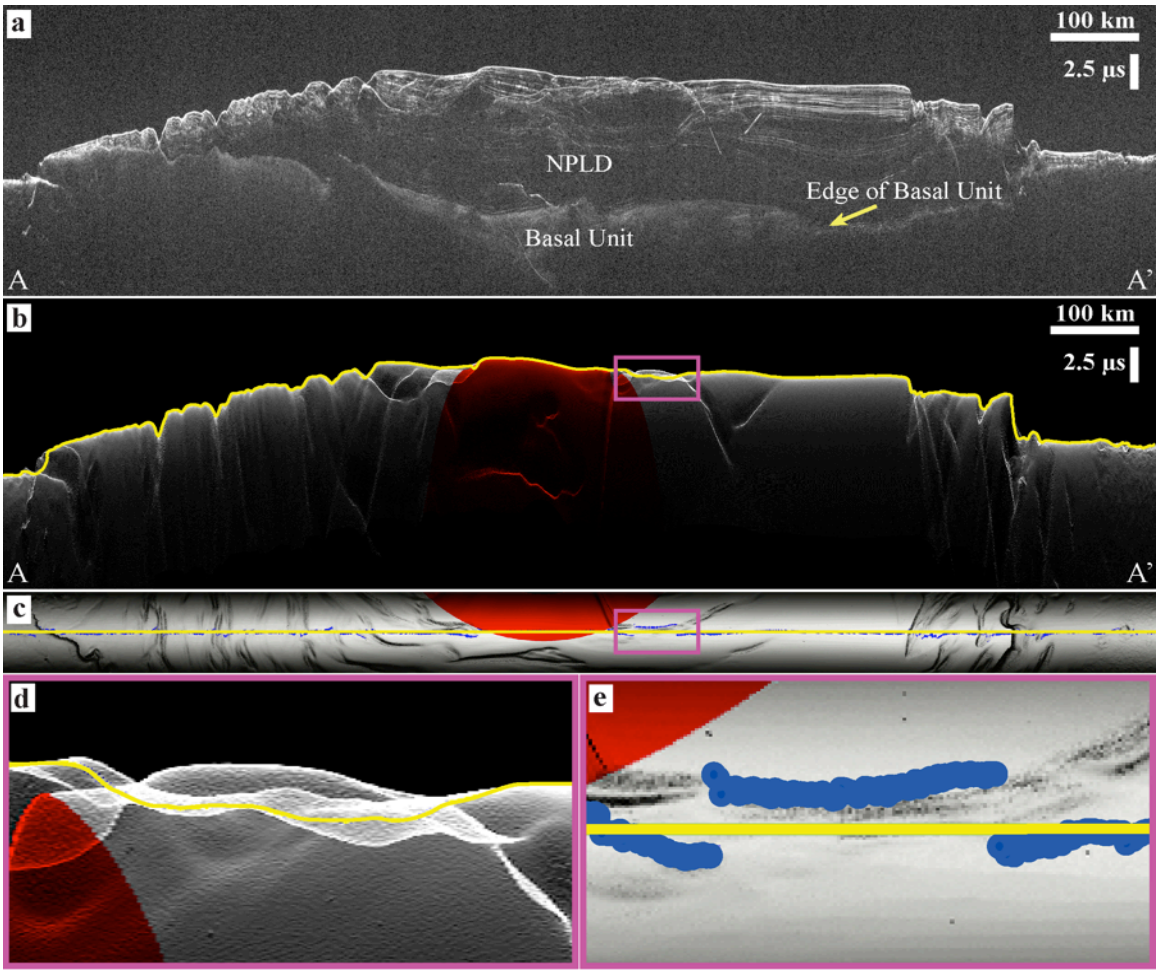

Figure 4. Radar observation 804402000. Location is shown on **Figure 2**. Vertical scale is one-way travel time. (a) FPB processed radar data shown in time delay. BU return changes from diffuse to sharp near Rupes Tenuis scarp. This radargram also highlights the smooth transition from BU to Vastitas Borealis marked "edge of basal unit". (b) UT Clutter Simulation. Yellow line on the simulation marks the time delay of the nadir location. Note the edges of Planum Boreum where interpretation becomes more difficult as clutter increases. (c) Echo power map for the radar return. Blue dots give the first return location while the yellow line is nadir. (d) Expanded view of clutter simulation. This section has a large difference between nadir and first radar return. (e) Expanded view of the echo power map covering the same region as in (d). Note the trough and resulting offset between nadir and first return locations.

An early SHARAD study [*Putzig et al.*, 2009] confirmed the first-order BU distribution and morphology as derived from optical methods [*Fishbaugh and Head*, 2005] and gave a first glimpse at the three dimensional structure of the deposit. A later study used MARSIS data to map the BU and calculate its volume [*Selvans et al.*, 2010]. The vertical resolution of MARSIS is approximately 100 m in water ice, an order of magnitude larger than the vertical resolution of 8.4 m for SHARAD [*Picardi et al.*, 2004;

Seu et al., 2007]. However, unlike SHARAD, MARSIS excels at penetrating to the base of Planum Boreum allowing it to map the contact between the BU and the underlying Vastitas Borealis Formation for most of Planum Boreum. While the resolution of MARSIS data was lower than the SHARAD study, *Selvans et al*. (2010) work confirmed speculations about the BU. Namely, the material composing Olympia Undae appears consistent with the BU mapped beneath Planum Boreum [*Selvans et al*., 2010]. In addition, MARSIS data gave the first volumetric constraints for the BU using radar data [*Selvans et al*., 2010]. Both of these radar studies found that the BU contains enigmatic features that cannot be easily explained, including the location of its maximum thickness offset from the north pole and specific locales that radar does not easily penetrate regardless of frequency.

Our study focuses on BU morphology from radar in a similar manner; however, the high resolution of SHARAD combined with dense BU radar mapping reveals additional features that may provide important insights into the early evolution of Planum Boreum.

1.3 DATA AND METHODS

1.3.1 SHARAD data, processing and corrections

SHARAD on Mars Reconnaissance Orbiter (MRO) acquired the primary data used for this study. SHARAD is a radar sounder with a 10 MHz bandwidth and a 20 MHz center frequency [*Seu et al*., 2007]. Mars Reconnaissance Orbiter has a polar,

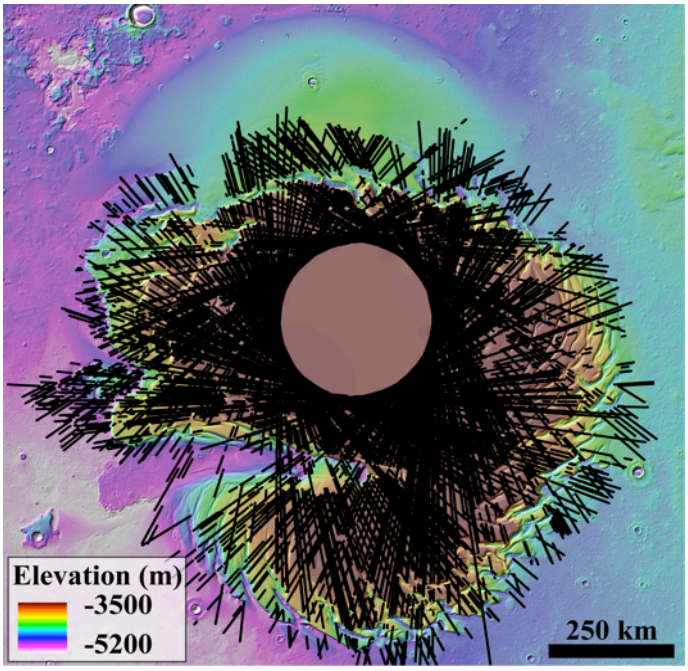

Figure 5. SHARAD mapping coverage used to generate gridded data products is shown as black dots. The SHARAD data is on top of colorized MOLA elevation data.

nearly circular orbit with an altitude of approximately 300 km [*Zurek and Smrekar*, 2007]. This, combined with focused processing, results in a signal footprint measuring ~3-6 km cross track and ~0.3-1 km along track. The bandwidth of SHARAD provides a 15 m free-space resolution and a theoretical vertical resolution of ~ 8.4 m in water ice [*Seu et al.*, 2007].

Two different processors were used for SHARAD analysis and interpretation. One of the processors ("FPB") makes use of an autofocus routine for correction of ionosphere delays [*Campbell et al.*, 2011]. This processor permits user-defined change of individual parameters such as aperture length, focusing Doppler bandwidth, weighting methods, and ionosphere correction. For mapping of BU deposits, it was qualitatively determined that a long aperture and large bandwidth gave optimal resolution, thus the FPB product used here has a 6400 length aperture and 0.6 MHz Doppler bandwidth. Comparatively, the additional processors used herein, "FPA" and its successor "QDA", employ a shorter aperture and smaller bandwidth. Radar data presented in this work are labeled to indicate which processor they were derived from. A total of 652 radar

observations, or orbital crossings of Planum Boreum, were used to generate the mapping results shown in this paper. Those 652 radargrams provide a total of ~645,000 points that span Planum Boreum and provide high-density coverage of the BU (Figure 5).

1.3.2 Interpretation of SHARAD data

Radar-based mapping was performed in commercial seismic interpretation environments, both Landmark's DecisionSpace and Schlumberger's GeoFrame. For interpretation, the processed data were converted from binary files into industry-standard SEG-Y files that were then loaded into seismic interpretation environments, map projected, and analyzed. Interpretation of the radar data used reproducible picking algorithms. Both software packages use manually-selected reflector locations to locate amplitude peaks present within a customizable time window; this methodology produces consistent results across radargrams and between interpreters. In displayed radargrams the brightness of a reflector is proportional to its amplitude.

Off-nadir echoes, or "surface clutter," challenge orbital radar sounding interpretations. Radar returns from surface features tens of kilometers from the orbit track are often visible in radargrams. While this problem is not as prevalent on the smooth areas of Planum Boreum as in areas with greater topographic relief, it can nevertheless confuse interpretations, especially near steep scarps and polar troughs. A clutter simulation algorithm was developed at the University of Texas Institute for Geophysics that generates synthetic radargrams based on surface topography and MRO

orbital geometry [*Choudhary et al*., in prep.; *Holt et al*., 2008]. This simulation generates a "cluttergram" that predicts the location of all possible surface echoes (rather than attempting to reproduce the radar data), and is used in combination with the radargram to ascertain which signals are from the surface and which are from the subsurface (Fig. 3b).

A particular difficulty when mapping a reflector across large regions in two-dimensional data is ensuring that the same reflector is consistently picked. In order to accomplish this, line ties and crossing radargrams were crucial for accurate mapping. Line ties exist where two radargrams intersect. The exact point of intersection is used to continuously interpret two different radargrams as a single observation. In theory, if the radar is penetrating the same location, the subsurface data at that point should be identical between the two radargrams. With crossing SHARAD observations, it is possible to stitch together radargrams creating a complete image that is no longer bound by the path of a single satellite orbit [Christian et al., 2013; their Fig. 4]. It is the tying together of different radargrams that enables accurate and robust subsurface mapping. With this technique, complex features can be analyzed from multiple viewing geometries to verify their existence and perhaps uncover their origin.

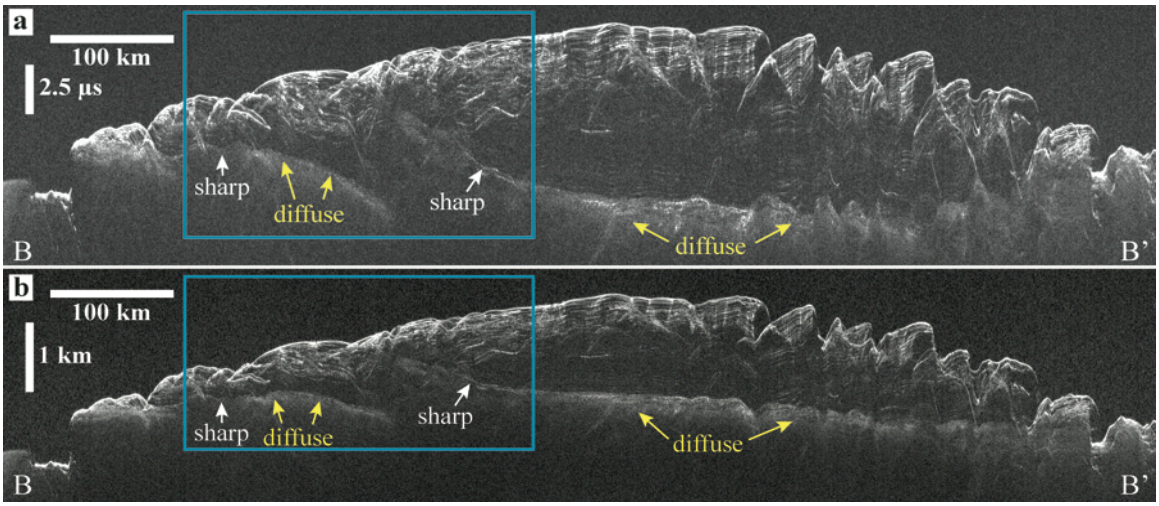

Figure 6. Radar observation 521402000. Location is given by the red line in **Figure 2**. This radargram crosses the BU high and shows the transition from a diffuse BU return to a sharp return. These data are products of the QDA processor and time is given in one-way travel. (a) Time-delay radar data. (b) Depth-corrected radar data using the real permittivity of water ice (εr = 3.15).

While specific radar reflectors within the NPLD are difficult to correlate with layers visible in outcrop [*Christian et al*., 2013], the BU's distinct characteristics offer a unique correlation between radar and imagery. In radar, the transition from NPLD to the BU is generally marked by a change from sharp, well-defined and laterally continuous reflectors to a diffuse zone of radar scattering with few to no internal reflectors. Where this is true, BU is easily differentiable from overlying NPLD. However, in some places the transition to BU is a sharp reflector, similar to overlying NPLD reflectors. In these cases the NPLD/BU transition is assumed to be the lowermost continuous reflector observed. Even though the signature of the BU can change from diffuse to sharp, correlation across and within radargrams supports our BU interpretation of this lowermost reflector (Figure 6).

1.3.3 Data gridding

Reflector interpretations or "picks" are exported from seismic software packages in ASCII format as along-track sample with time delay, and then processed by a series of scripts that convert the reflector time delays into aeroidal elevation with latitude and longitude. This requires registration of the associated surface echo (interpreted in the same manner as the subsurface reflectors) to a known surface elevation. We use the Mars Orbiter Laser Altimeter (MOLA) gridded surface for this [*Smith et al*., 2001].

The final conversion step provides two exported data products for gridding, each with a different assumption about the location of the first and subsequent echoes [as in Christian et al., 2013]. The *nadir* product positions all of the radar reflectors directly beneath the spacecraft. In contrast, the *first return* product uses MOLA topography and a model of the radar beam pattern to calculate the likely origin of the first signal returned to SHARAD, a location that often, but does not always, coincide with the maximum amplitude return. Individual points are then corrected to this "first return" location and all subsurface data assume a vertical signal propagation path from the first return location (Fig. 3c and 3e). A comparison of gridded data products is shown herein (Fig. 6).

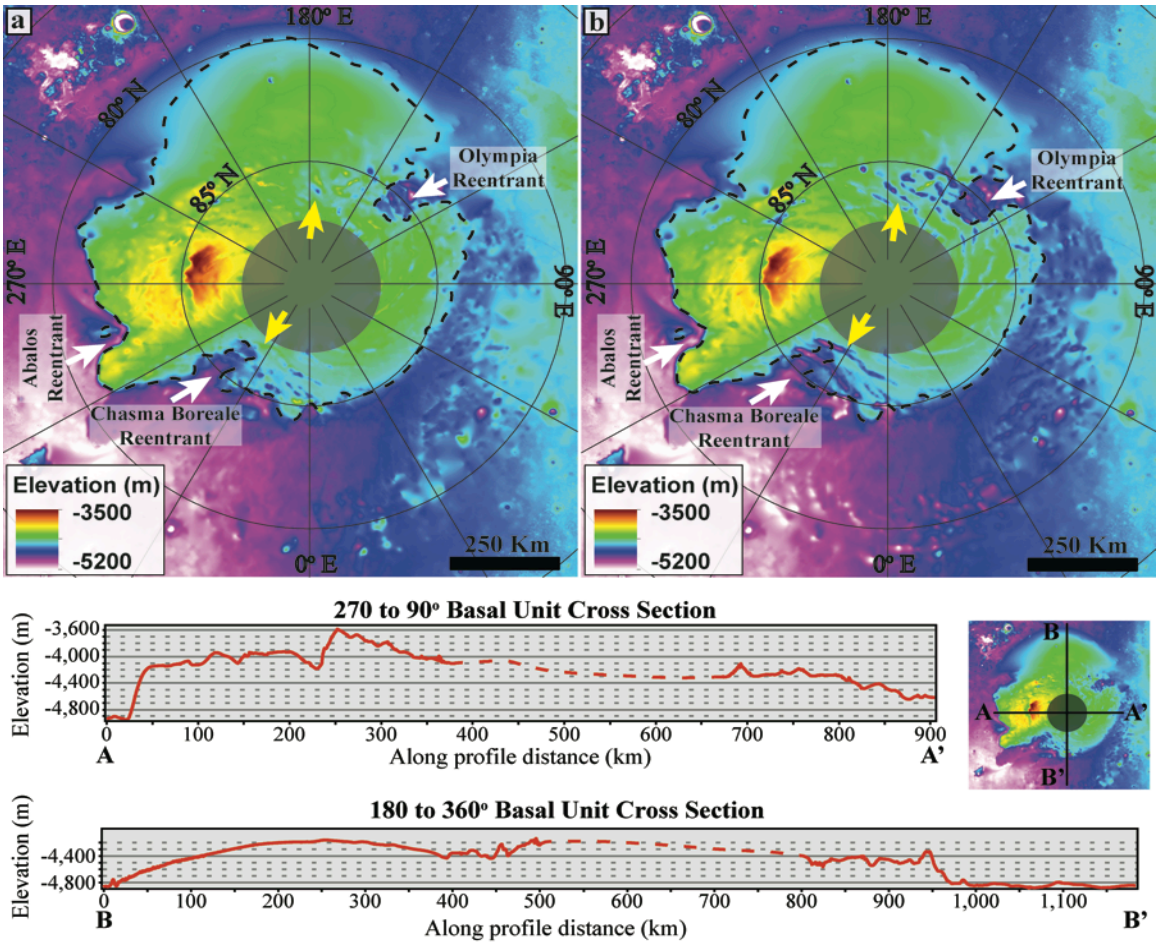

Figure 7. Colorized BU elevation results derived from gridded SHARAD data. Two different data positioning algorithms are shown. (a) Data corrected using the first return technique as discussed in text (preferred version). (b) Data left at nadir location and not corrected. Notice the troughs in the nadir data. These are the result of depth correction without moving the radar data. Yellow arrows point to regions with significant difference between first return and nadir mapping results. In both figures a black dashed line represents the radar-derived extent for BU material. (bottom) Two BU cross sections generated from the first return product. These cross sections highlight the inhomogeneity of the BU deposit.

Neither approach is perfect for mapping BU structure, as each has strengths and weaknesses. For example, the nadir approach creates artificial peaks in the data directly beneath spiral troughs while the first return approach generates artificial troughs at this same location (Figure 7). From the stratigraphic mapping of trough structures throughout hundreds of radargrams [*Smith and Holt*, 2010, 2015], we know that most troughs

originate within the NPLD, not at the BU/NPLD transition. Additionally, trough mapping revealed that these structures migrate polewards. Thus, the surface expression of a trough is typically greater than 30 kilometers northwards of where the trough originated, not directly above [*Smith and Holt*, 2010]. Preliminary testing of the first return approach and its use in gridding NPLD stratigraphy indicated it to be nearly perfect for reflectors in the top few hundred meters [*Christian et al*., 2013]. However, the accuracy of the method appears to degrade with depth, which may be due to a signal propagation path that is more complex than either assumption alone. Both methods assume the radar data travels vertically downward below the point of surface penetration, and this assumption is likely to produce small errors. The errors generated from the nadir assumption in the BU topography are more pronounced (Figure 7). Therefore, it is our preference to use the first return assumption for positioning radar data acquired over Planum Boreum.

After data extraction and positioning, the interpreted data were gridded. Gridding was performed using ESRI's ArcGIS (Geographic Information System) software. The ASCII files containing reflector interpretations were loaded directly into the program, converted into an ESRI-compatible format and interpolated using a natural neighbor algorithm. This method interpolates using weights, similar to an inverse distance weighted approach, but different in that distances used for the weighted mean are calculated from the overlap of Voronoi polygons instead of from a source point [*Sibson*, 1981]. A resolution of 256 pixels per degree was assigned for the output raster products. SHARAD does not acquire data north of 87.5° latitude due to its polar orbit; however, we

do interpolate across the polar data gap. Our mapping products cover this data gap with a dark oval to emphasize the uncertainty of SHARAD gridding north of 87.5°.

Gridded data were used for analysis of the BU and for all volumetric calculations pertaining to BU and overlying NPLD. For the purposes of volumetric BU calculations, the Vastitas Borealis base was assumed smooth, created by the interpolation of a small number of MOLA shotpoint data in conjunction with SHARAD interpretations of the Vastitas Borealis surface (Figure 8).

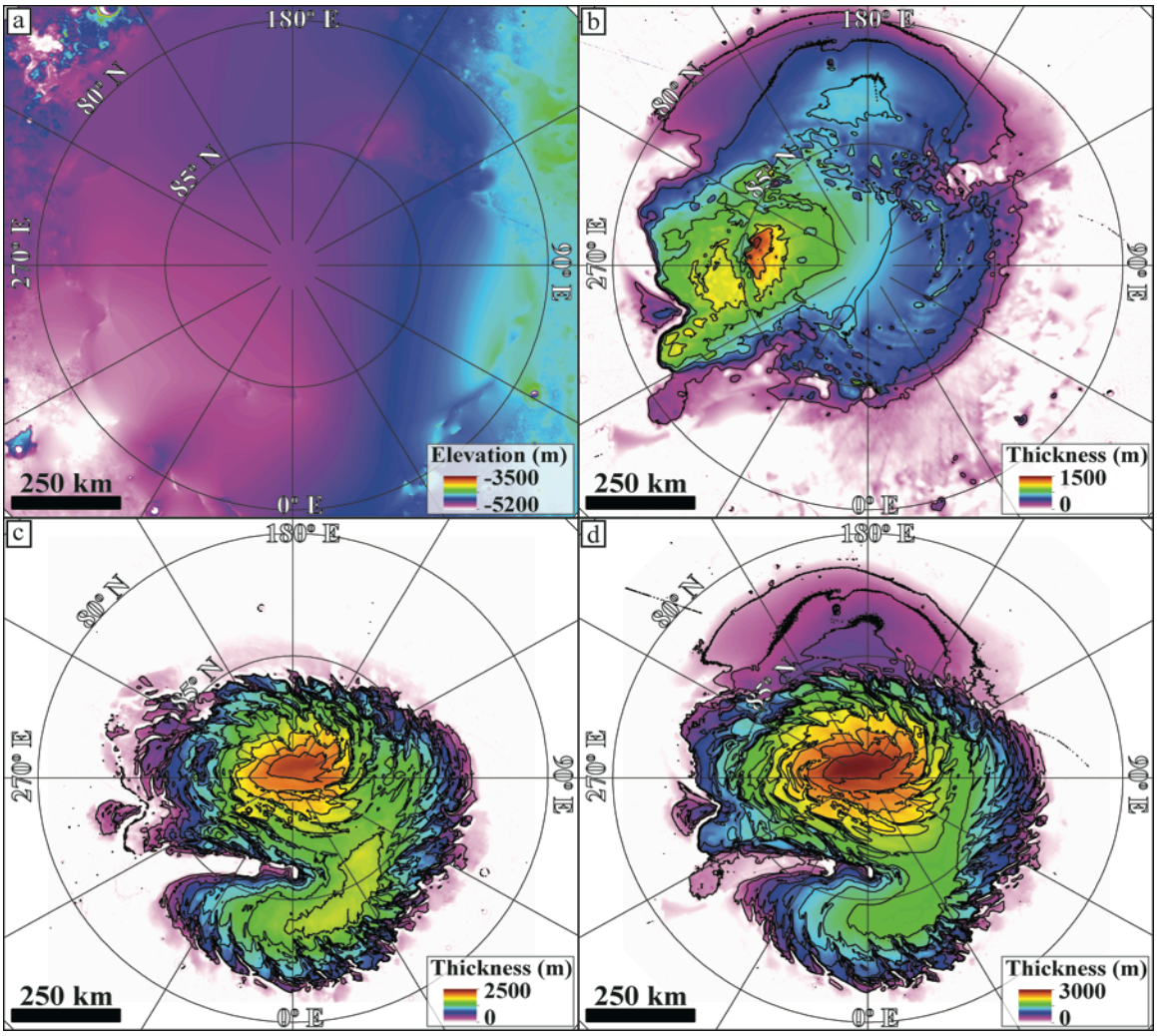

Figure 8. Isopach maps for BU and NPLD material. Contours are at 200 meter intervals. (a) Topography of Vastitas Borealis after removal of all overlying material including both BU and NPLD. This grid was generated by combination of SHARAD and MOLA shotpoint data and is used as the base of our subsequent thickness maps. (b) BU isopach map. The Vastitas Borealis grid was subtracted from the 1st return BU grid to create this product. Note the maximum thickness is approximately 1500 m. (c) Thickness map of NPLD material. (d) Isopach map for the entire deposit, all material above the generated Vastitas Borealis grid (a) is included in these thickness values.

1.3.4 Reentrant volume estimations

To estimate the volume of eroded BU material we first created a BU topography without any reentrant morphology. This surface is the hypothesized pre-reentrant configuration of basal unit material. To accomplish this, interpolation was done across each reentrants using only boundary elevation values. From the newly created surface, we subtracted the elevation of the modern BU topography resulting in a thickness raster for eroded material. Within ESRI's ArcGIS we were able to use these constructed isopach maps to calculate the hypothesized missing BU volume from each reentrant.

Calculation of the surrounding terrains' dune volume was done using a similar methodology. Equivalently, we interpolated across the landforms of interest using boundary elevation values. However, unlike with the reentrants, this resulted in a lower surface whereas the MOLA elevation created the upper surface. Once again, subtracting the lower surface from the upper surface gave us isopach maps which were then used for volumetric calculation and comparison.

1.3.5 Mesoscale wind modeling

In cooperation with the Laboratoire de Météorologie Dynamique (LMD) University Pierre and Marie Curie, the BU topography was used for modeling the atmospheric properties over the north pole of Mars. While our initial gridded topography was created at 256 pixels per degree (ppd) resolution, topography used by the model was down sampled to 64 ppd (~920 m resolution) using the nearest neighbor algorithm to

derive cell values. At its outer boundaries, the 64 ppd BU topography was merged with 64 ppd gridded MOLA topography generating a complete northern hemisphere of Mars for input into the LMD mesoscale model [*Spiga and Forget*, 2009]. To account for the polar data gap north of 87.5° latitude, we interpolated across this void using values consistent with those at the boundary. We then generated wind maps at 6 km resolution for Planum Boreum over a complete diurnal cycle, assuming present atmospheric properties.

1.4 RESULTS

This study has produced the most detailed subsurface map of BU topography yet available (Figure 7). The results here are significantly different from early Planum Boreum BU maps [*Byrne and Murray*, 2002; *Tanaka et al*., 2008; *Selvans et al*., 2010] and improved from the previous SHARAD mapping study [*Putzig et al*., 2009]. An important consideration is that due to the orbital inclination of MRO, no radar data exists north of 87.5° latitude; therefore our gridded maps have been masked north of that latitude.

Our results for BU extent show a highly asymmetric, ~700-km-wide deposit (Figure 7). The thickest mapped portion of this deposit is located at 85.7° N and 265° E, offset from the center of Planum Boreum. There, the BU has a thickness much greater than 1 km, assuming a smooth base for Vastitas Borealis (Figure 8). From our gridded

isopach maps we calculate volumes for BU, NPLD, and Planum Boreum material (Table 1).

	BU Volume (10^6 km^3)	NPLD Volume (10^6 km^3)	Planum Boreum Volume (10^6 km^3)
SHARAD	0.38	0.79	1.17
MARSIS	0.45	0.78	1.3
MOLA			1.14

Table 1. Volumetric results from this study, SHARAD, compared to MARSIS and MOLA results. The MARSIS results are from *Selvans et al*. 2010 while the MOLA results are from *Smith et al*. 2001. The *Smith et al*. 2001 MOLA study did not analyze the BU and NPLD separately.

There is a geographic pattern to the differing BU radar return properties discussed in Section 3.2. Near the BU topographic high, the return is sharp and bright (Figure 4). This indicates a strong dielectric contrast with a relatively smooth surface, resulting in low scattering losses. However, near the periphery of the BU at the east, the NPLD – BU transition is a diffuse radar interface. This style of return is hypothesized to result from scattering of the radar signal and is easily distinguished from sharp radar reflections. A more detailed analysis of the significance of this dualistic BU radar reflection character will be addressed in the discussion section.

With the BU high as our point of reference, the eastern and western hemispheres (in polar projection) express markedly different morphologies. In terms of longitude, this referencing corresponds to a separation of 0° to 180° as the eastern half and 180° to 360° as the western half. The east half is characterized by a low, smooth slope that makes a gradual and continuous transition from the BU high onto Vastitas Borealis. The west has a steep slope following the BU high, a trough, and then a flat, broad deposit (Figure 7).

At the edge of the western BU is the Rupes Tenuis scarp, where the BU is abruptly truncated.

Three features resembling reentrants are evident in the BU (Figure 7). Two of these features are found in the vicinity of, but not coincident with, present-day Chasma Boreale while the third is found near present-day Olympia Cavi. These reentrants are variable in size ranging from 50 km to over 100 km long. In addition, the general morphology of these features is variable with no obvious correlation.

Wind maps generated via mesoscale modeling and BU topography (Figure 9) show strong topographic control, with flow away from the BU high. The winds move outward with Coriolis deflection, similar to the modern wind flow [*Howard*, 2000] and modern modeling results [*Spiga et al*., 2011a]. The weakest winds are south of the BU high trough, directly over Olympia Undae, and over the north pole data gap where topography was smoothly interpolated across (Figure 9). In addition, weak winds are located at the periphery of Planum Boreum following their sharp acceleration over the deposits edge. Consistent winds are found south of Planum Boreum, with a nearly constant 4-5 m/s wind velocity, in stark contrast to central Planum Boreum's spatially variable winds (Figure 9).

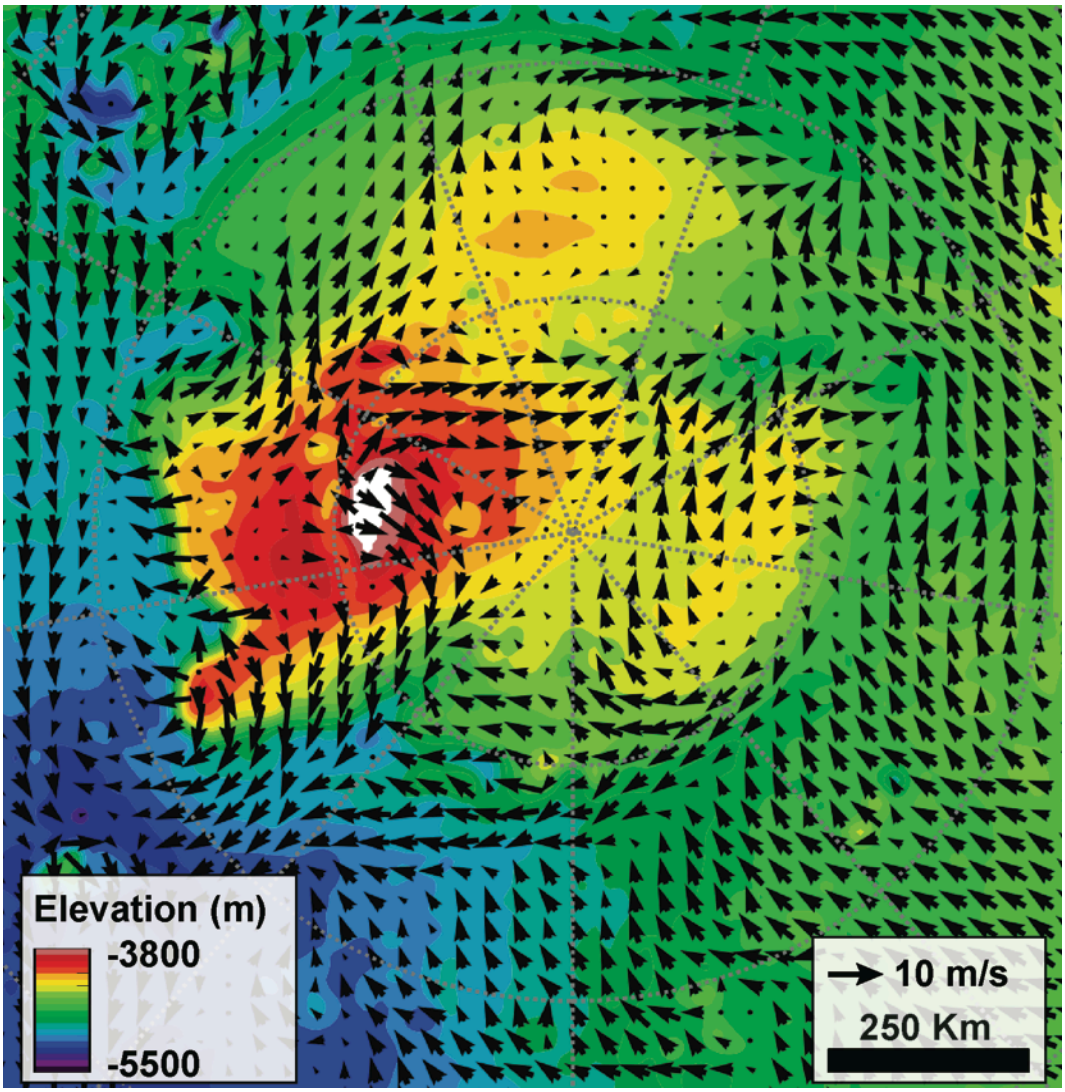

Figure 9. Mesoscale wind modeling results using SHARAD paleotopography. Topography is color shaded by elevation and vectors show wind magnitude and direction. The modeled winds for Planum Boreum are largely consistent with time. Shown here is a midday timestep.

1.5 DISCUSSION

1.5.1 BU extent

In the west, the only surface exposures of the BU margin are along the Rupes Tenuis scarp and within Chasma Boreale. The Rupes Tenuis scarp creates the edge of the modern BU extent in the Abalos region (see Figure 2). Elsewhere, BU is covered by NPLD, preventing direct optical-based determinations of the BU margin location [*Byrne and Murray*, 2002; *Herkenhoff et al*., 2007; *Tanaka et al*., 2008; *Warner and Farmer*, 2008b; *Kneissl et al*., 2011]. *Tanaka et al*. (2008) hypothesize a vertical kilometer of BU erosion at Rupes Tenuis, the location of rupes unit exposure. Kilometer-scale erosion in combination with crater counting supports hypotheses that the BU is significantly older than the overlying NPLD [*Tanaka et al*., 2008]. However, optical mapping could not verify the buried extent of the BU's truncated edge. Subsurface stratigraphy revealed by the SHARAD dataset and mapped in this study allows us to expand upon these initial observations of BU extent and morphology. In addition, we compare the results of our study to the earlier SHARAD study [*Putzig et al*., 2009] to ascertain the impact of increased data coverage on mapping results.

While the BU boundary from approximately 240ºE to 300ºE exhibits a steep scarp and widespread erosion, this study reaffirms that the erosional character of the Rupes Tenuis scarp is a localized feature. Elsewhere beneath Planum Boreum the BU transition to Vastitas Borealis is a smooth or gradual transition (see Figure 4). The deposit maintains a low slope (less than 2º) and eventually downlaps onto Vastitas Borealis

Formation at its periphery. Note that a smooth transition does not mean that the BU on the eastern edge is without erosion; it only indicates that erosion on the eastern edge, if present, was a different process and did not result in the same morphology as that on the western edge. Impact craters and associated, armored surfaces have been observed on the western side and may be responsible for the distinct erosional properties there. Impact ejecta and resultant armoring have not been observed along the basal unit edge from 0ºE to 180ºE. Impact ejecta armoring may have resisted erosion [*Arvidson et al*., 1976], creating the large relief of Rupes Tenuis [*Tanaka et al*., 2008], whereas the eastern half was not armored, and eroded with a smooth transition to Vastitas Borealis. The remaining margins, toward Olympia Undae and Gemina Lingula, exhibit smooth edges and transitions to the Vastitas Borealis Fm., with only minor irregularities in specific regions. As presented by *Selvans et al*. (2010), we also find that the BU is smoothly contiguous with Olympia Undae, and that the dune field there is likely composed of, and underlain by, BU material. Thus, the Olympia Undae dune field is included in our work as part of the current BU extent.

1.5.2 Depocenters

In previously published radar studies, BU mapping indicated that the thickest BU deposit is offset from 90º latitude [*Putzig et al*., 2009; *Selvans et al*., 2010]. As the thickest portion of Planum Boreum is very near 90º (Figure 8), if the BU and overlying NPLD were formed from similar processes in a similar climatic and orbital configuration,

one would expect the thickest BU deposit to also be near 90°. Our work establishes that the offset is to the south along the N 265° E meridian, with the BU maximum thickness located at approximately 85.7° N 265° E (Figure 8). This result is similar to the previous SHARAD study [*Putzig et al*., 2009] but significantly different from MARSIS results [*Selvans et al*., 2010].

In this work we hypothesize that the mapped BU maximum thickness corresponds to the location of the BU's depocenter. This assumption is supported by the presence of isolated rupes unit material south of Planum Boreum between 240° and 330° longitude [*Tanaka and Fortezzo*, 2012], the steep nearby Rupes Tenuis scarp which directly contrasts the transition from BU to Vastitas Borealis Formation mapped from 0° to 180° longitude, and that lack of data supporting additional highs within the polar data gap. In fact, the SHARAD data contain no evidence that the basal unit elevation increases north of 87.5° latitude. The BU maximum thickness' proximity to the Rupes Tenuis scarp both supports the claim that this area is the depocenter and reinforces the need for large-scale BU erosion from the scarp. Without erosion, the basal unit should have extended much farther past Rupes Tenuis than it does currently, assuming coarsely symmetrical deposition. Therefore, the offset center found in SHARAD mapping agrees with hypothesized erosion of BU from Rupes Tenuis, the mapped BU outlier material, and the nearly flat-lying bedding in Rupes Tenuis [*Tanaka et al*., 2008; *Tanaka and Fortezzo*, 2012].

While the location of the thickest BU mapped in this work agrees with that of *Putzig et al*. (2009), other features associated with the high point are revealed in our

study; in particular, a linear depression south of the BU high is apparent that mimics the morphology of a nearby modern trough (Figure 10). Although most polar troughs originated within the NPLD [*Smith and Holt*, 2015] it appears possible that at least in this location, the morphology of a trough-like feature in the BU may have propagated into the NPLD and migrated northward similar to other trough migration patterns [*Smith and Holt*, 2015]. However, SHARAD data have shown no conclusive link between the linear depression and overlying spiral troughs. Reflectors directly above the BU trough are virtually nonexistent in SHARAD data and trough migration path tracing here requires large assumptions about migration path.

Using our BU mapping results we generated isopach maps for the overlying NPLD material. This result will help provide constraints to water budget estimations when modeling deposition of the NPLD. The MARSIS-based radar study of *Selvans et*

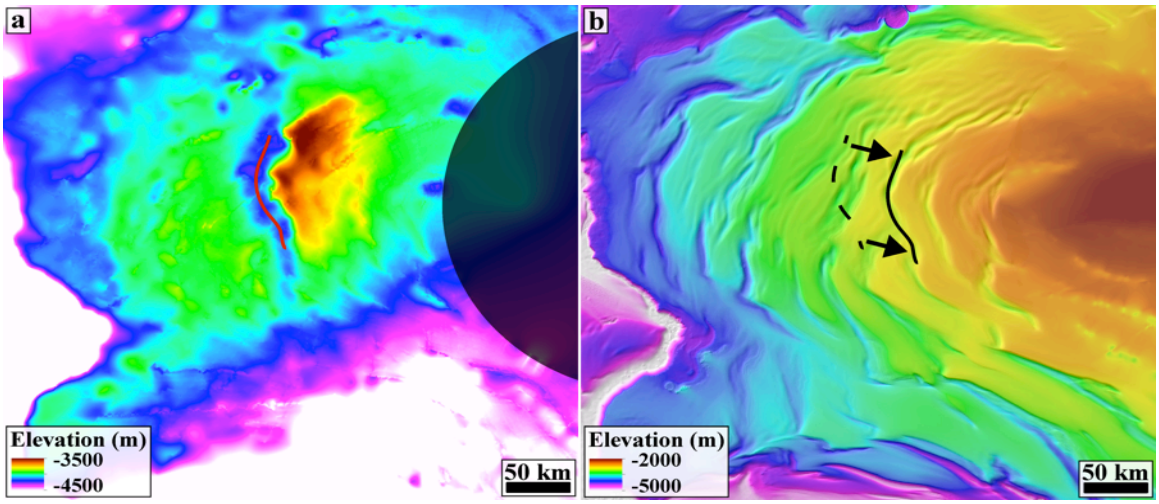

Figure 10. (a) Expanded view of the BU color shaded topography centered on the depression near the high. A red line is drawn on this feature for comparison with part (b). (b) MOLA topography over the BU high. The dashed black line gives the position of the BU depression. Arrows are drawn from the BU depression to a modern trough with similar morphology.

al. (2010) indicated that the thickest region of NPLD deposition was at 30° E longitude and ~1800 m in thickness. Both the location and thickness in our study differ significantly. Our study finds the maximum NPLD thickness to be ~2350 m and located at 105° E longitude and 87.5° latitude; however it is likely that there is additional thickness north of 87.5° based on trends in our isopach maps with respect to the gap in data coverage above 87.5°latitude. It is important to note that the theoretical resolution of SHARAD and MARSIS differ by an order of magnitude. In practice, the two radars have even greater difference due to the ionospheric interference suffered by MARSIS with its lower operating frequency, and it is therefore our preference to rely on SHARAD results.

The difference in locations for BU and NPLD maximum thicknesses emphasizes that different patterns of accumulation likely dominated each deposit. We posit that the shift of depocenter from the 240° longitude line for the BU toward the pole for the NPLD is the result of atmospheric influences, although determination of a specific cause is beyond the scope of this work. As transition from sand sheet to water ice deposition is a clear indicator of change, we believe that climatic influence likely contributed to the depocenter shift. While a depocenter shift can also be influenced by the feedback of local topography, we believe a climatic contribution cannot be ignored.

1.5.3 BU morphological irregularities: hypothesis and implications for cavi unit

The BU high is immediately poleward of a prominent, arcuate depression. In contrast to the nearly uniform 0.1° - 0.4° slopes found elsewhere on the BU surface, the depression is defined by an equator-facing slope that varies from ~ 2.5 ° - 4.0°. This value is comparable to the ~ 3° slopes of modern spiral troughs prevalent in this region [*Smith et al*., 2013; *Smith and Holt*, 2015]. In radargrams the depression appears to truncate the BU (Figure 11), suggesting it is erosional in nature. Any explanation for the BU morphology in this region must describe the genesis of the BU high, the steep slope defining its equatorward edge, the trough found at its base, and the relatively thick, flat, BU surface extending between the trough and the modern margin of the unit. Here our use of the word trough is intended only to describe the quasi-linear topographic low directly equatorward of the BU high, and is not intended to imply that this BU feature is equivalent in origin to the modern spiral troughs (although it could have initiated subsequent trough formation in the NPLD).

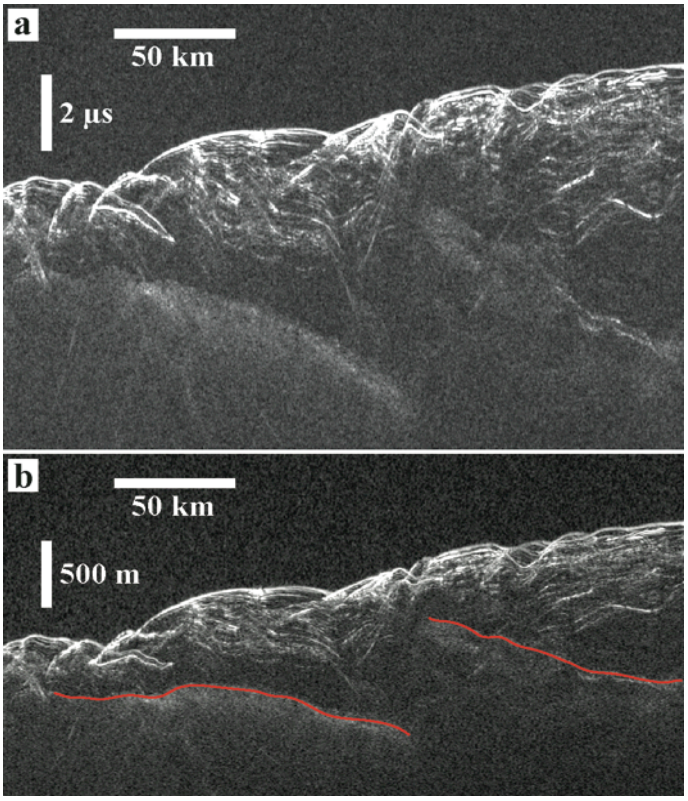

Figure 11. Radargram 521402000 enlarged to show BU truncation on the west side of the high. See **Figure 6** for context. Part (a) is in one-way time while (b) has been depth corrected using a real permittivity of 3.15. Red line denotes the interpreted transition from NPLD to BU material.

Our explanation for the BU high assumes that it was originally the center of rupes deposition, that asymmetric aeolian erosion resulting from material differences led to the differences between eastern and western regions. This hypothesis takes into account the aeolian origin of the basal unit [*Tanaka et al*., 2008], offering explanation for both genesis and location of cavi material. We suggest the BU high has always been the thickest part of the deposit. Observations of BU outcrops around Planum Boreum have noted the presence of impact-related deposits on the western exposures, but not the eastern [*Tanaka et al*., 2008]. An approximately 100 km poleward extension of these impact events in the western half of the deposit would have resulted in the formation of additional armored ejecta, which can retard erosion [*Arvidson et al*., 1976]. We additionally posit that no armoring was present on the BU high. The rupes unit, in particular, is known to have undergone extensive erosion with ~ 1 vertical km or more of material removed along Rupes Tenuis [*Tanaka et al*., 2008].

The large extent of rupes erosion becomes important when considering the potential role of armored deposits in influencing BU morphology. Erosion of the unarmored BU surface adjacent to armored deposits would have been irregular. Furthermore, asymmetry in the distribution of impact deposits would have led to deposit-wide asymmetric erosional patterns as has been observed for the south polar layered deposits [*Kolb and Tanaka*, 2006].

Both local and regional characteristics, including the trough and the drastically different morphologies of the western and eastern halves of the BU surface, can be explained by our hypothesis (illustrated in Figure 12). Beginning with a pre-existing high resulting from depositional patterns, katabatic winds shed off the high to the west would have encountered both armored and unarmored deposits. It is feasible that the trough originated as a zone of easily-eroded, unarmored sediment. Topographically enhanced through continued erosion, it continued to evolve into the current feature, characterized

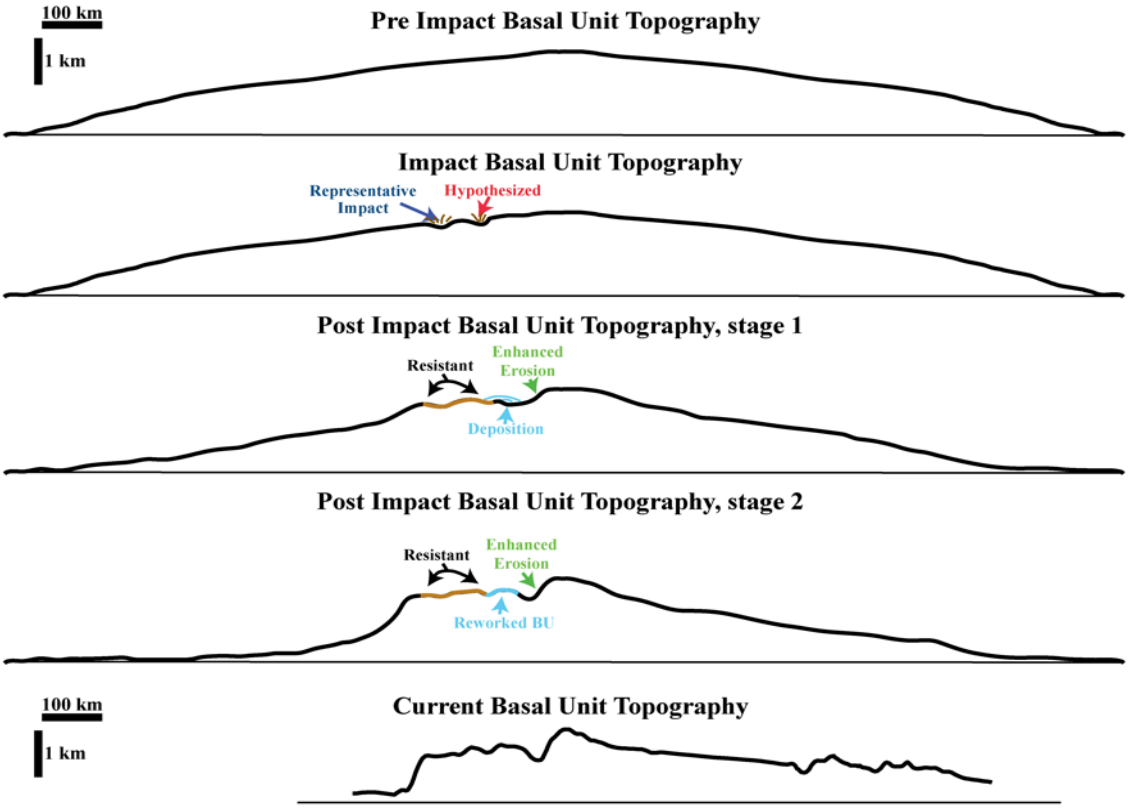

Figure 12. Hypothesized evolution of the BU topography. Transect is coincident with radar observation 521402000 and the location is shown in **Figure 2** (red line). Known impact events along Rupes Tenuis are labeled along with the location of our hypothesized impact. The impacts result in ejecta armoring and a resistant layer. Katabatic winds and differential erosion, resulting from the impact armoring, dictate landform evolution in the post-impact BU figures.

by an equator-facing slope of magnitude comparable to modern slopes of the wind and sediment transport-driven spiral troughs. The broad, relatively flat feature between the trough and the deposit margin can be explained as the result of flow deceleration out of the trough and the deposition of eroded sediments in this region. Katabatic winds shed off the high to the east, however, encountered no such irregularities in surface properties that modify erosion. In the absence of armored ejecta deposits, material was eroded and distributed more uniformly, generating asymmetry in the gross morphology of the BU surface (Figure 7, Figure 8, Figure 12).

Our proposed hypothesis posits initial homogeneity of the rupes unit material. However, if the rupes unit has large heterogeneities in composition and strength, it becomes possible to generate the basal unit high without impact ejecta armoring. While fundamentally the same processes, it is no longer necessary that the surface becomes fully armored. Instead, where we posit an impact event there would need to be compositionally or structurally distinct rupes unit material. Inhomogeneity of the rupes unit, enhanced cohesion or weathering resistance where we posit armoring, could inherently explain the different morphology of the basal unit deposit from 0ºE to 180ºE when compared to morphology from 180ºE to 360ºE. However, it is our preference to expand on the observed impact phenomena rather than rely on hypothetical compositional variation of rupes unit.

Optical and SHARAD based mapping of the distribution of cavi unit supports the proposed hypothesis. Estimated to be Middle Amazonian in age, the cavi unit represents a transitional member between the BU and overlying NPLD that was deposited during

and/or after erosion of the rupes unit [*Tanaka et al*., 2008]. It is reasonable to assume that the substantial erosion of the rupes unit provided the loose sediment needed to accumulate the cavi. Therefore, the cavi's distribution is intimately related to rupes morphology and the distribution of armored impact ejecta. Mapping in SHARAD data has distinguished two types of returns from the top of the BU: sharp and diffuse. Notably, sharp BU returns exist primarily in the vicinity of the BU high as well as in the western half of the deposit, while diffuse returns dominate the eastern half and the flat area directly equatorward of the trough (Figure 13). The lateral segregation of sharp and diffuse reflectors corresponds with the hypothesized locations of, respectively, wind-scoured rupes and deposition of eroded material as part of the cavi unit. Given the different depositional styles of the rupes and cavi units [*Herkenhoff et al*., 2007; *Tanaka et al*., 2008] and resultant implications for radar returns [*Putzig et al*., 2009], this hypothesis is reasonable. Rupes unit is exposed along the Rupes Tenuis scarp and it is at this location that the radar return is bright and sharp (Figure 4 and Figure 13). Locales with exposed cavi unit are generally diffuse, however, there can be inconsistencies between radargrams and the diffusivity appears to be less of an indication for composition than the sharp radar return.

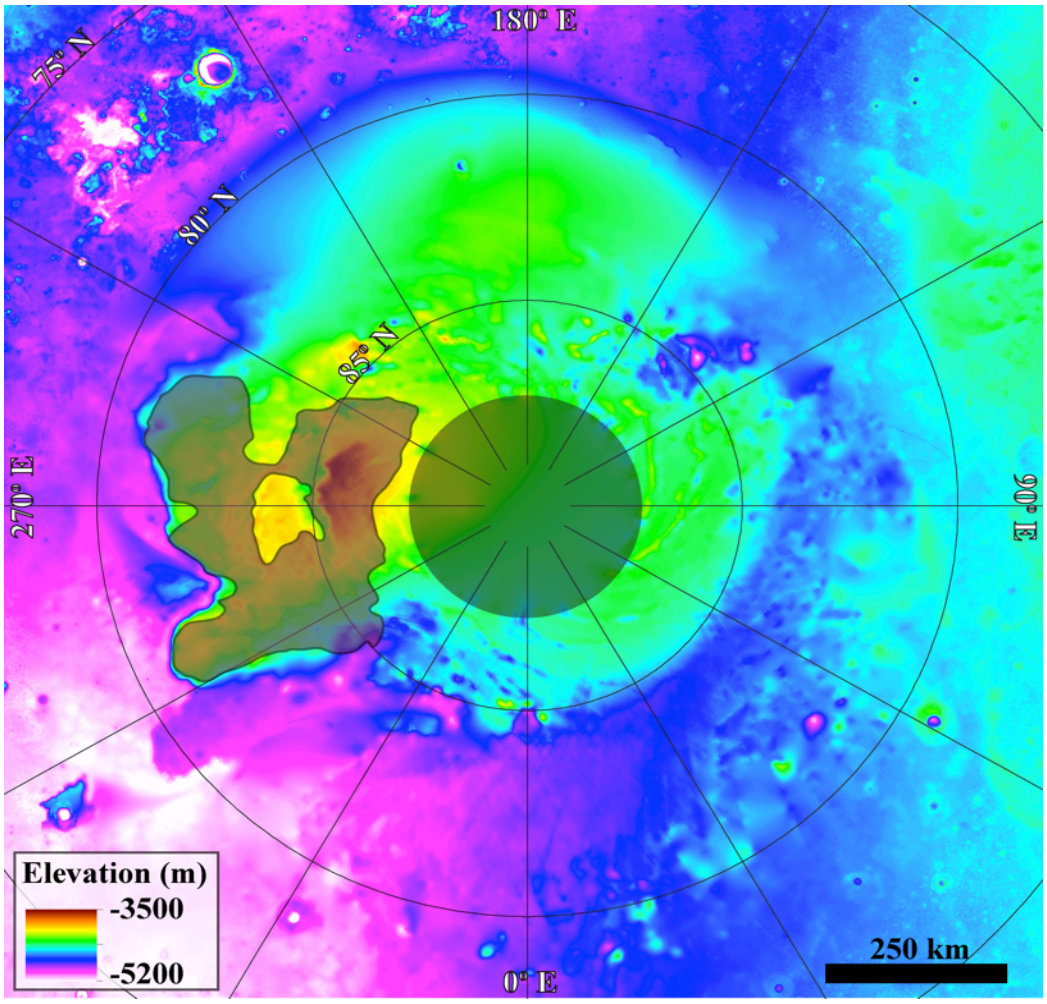

Figure 13. The extent of sharp SHARAD BU radar returns is shown by the semi-transparent black polygon overlapping colorized BU topography. Our work hypothesizes that the sharp radar return is from rupes unit without cavi. The lack of a sharp return downwind of the BU topographic high is likely the result of deposited, reworked, rupes material downwind of erosion.

Additional support for the subsurface distribution of rupes and cavi resulting from patterns of deposition and erosion is provided by image analysis of Planum Boreum's margins. Notably, the greatest occurrences of cavi unit, a product of rupes erosion, are in Olympia Cavi [*Tanaka et al*., 2008], which exists in the eastern half of the BU deposit, and proximal to our mapped diffuse SHARAD BU returns. In these locations the lack of

armored deposits and local topographic influence due to the presence of armored deposits, respectively, led to an increase of cavi deposition. This is comparable to the known formation mechanism of cavi outlier beneath Abalos Mensa, where erosion of the Rupes Tenuis scarp in combination with local wind patterns led to the accumulation of the wedge-shaped mound of sediment [*Brothers et al*., 2013].

The hypothesis presented here for the distinct morphology of the BU is significantly different from prior hypotheses. Initial investigation of the BU high explained its existence by a single impact event directly over the high point, which subsequently armored the high from erosion while the unarmored material around it was eroded and transported away [*Putzig et al*., 2009]. In this hypothesis the modern morphology of the BU results solely from the occurrence of a single impact event. Additionally, this hypothesis should result in symmetrical erosion around the BU high along the N 270° E meridian, inconsistent with BU mapping results. Given the intricacies of aeolian systems, it seems more likely that the morphology was driven by a combination of initial depositional and later erosional processes. Provided an antecedent topography resulting from regional depositional patterns, katabatic winds from the depositional high in conjunction with asymmetrically-distributed armored impact ejecta are able to explain not only the irregular local topographic features of the BU, but also its nonuniform surface morphology (Figure 12).

1.5.4 Analysis of the three major reentrants in the BU deposit

In addition to BU irregularities due to offset of the depocenter from 90° latitude and asymmetric erosion, the unit also contains three prominent reentrants that result in further morphologic irregularity. These cutbacks into the BU deposit are variable in size and morphology. As only three substantial reentrants have been uncovered, it would also appear that they are not representative of typical processes in the BU and required special circumstances to form. Mapped reentrants clearly impact overlying deposition and provide additional information about the nature of ice deposition following BU emplacement.

One major reentrant is in the Abalos region and bounded by the modern Rupes Tenuis scarp (Figure 2 and Figure 10). As SHARAD data for this feature were analyzed in a prior publication [*Brothers et al*., 2013], it will only be mentioned briefly here. The topography of Abalos has been heavily influenced by this reentrant – everything from dune deposits radiating away from the ice cap to the isolated wedge of cavi unit and NPLD forming Abalos Mensa are the result of the reentrant and the Rupes Tenuis scarp. The dune field along the eastern edge of Abalos Mensa has sand hypothesized to be of BU origin [*Byrne and Murray*, 2002; *Tanaka et al*., 2008], and it is feasible that all of this sand might have been sourced from the BU reentrant that created Rupes Tenuis. We estimate the volume of material removed from the Abalos reentrant and compare that to the volume of material present in the dune field. Dune field volume was obtained using MOLA topography and a base constructed by interpolating between elevation points. The subtraction of the interpolated base from the MOLA top is the volume we use for our

dune field. Our results indicate that Abalos basal unit erosion is more than sufficient to supply the local dune field. Only 30% of the eroded material must remain if rupes is 50% sand by volume (Table 2). The excess sand was likely transported to another portion of the circumpolar erg.

	Eroded BU Ice (km^3)	Sediment in nearby features (km^3)	Sediment/ Eroded Ice (%)
AC	3383.39	522.8	15.45
CB	3654.46	3315.82	90.73

Table 2. Volumetric analysis of BU material. Eroded ice is calculated via interpolation as described in Section 3.4. The ratio of sediment to eroded ice should not exceed 50% if basal unit material is responsible for the analyzed landform.

A second reentrant is not readily apparent in Planum Boreum's modern topography. This reentrant is located at ~300° E longitude and extends from the northwestern wall of present-day Chasma Boreale to 87°N (Figure 7 and Figure 14a,b). It measures approximately 110 km wide and 150 km long, and is larger than the Abalos reentrant. Using the same methodology as with the Abalos reentrant, the volume of BU material removed to create this reentrant was calculated (assuming it is entirely erosional). The result of this erosion is likely either the lobe of material that is Hyperborea Lingula (Figure 1), or dunes within Chasma Boreale, resting on top of Hyperborea Lingula. Unlike in the Abalos region, the dunes that exist in Chasma Boreale are less clearly linked to the reentrant. We estimate that nearly all of the BU sediment removed from this reentrant would have needed to remain as Hyperborea Lingula to account for the lobe's volume (Table 2). This result is in a stark contrast to the Abalos reentrant and an unlikely scenario; however, studies have indicated that Hyperborea Lingula may in fact be partially preserved rupes unit [*Tanaka et al*., 2008] Alternatively,

if the reentrant within Chasma Boreale is only responsible for the dunes atop Hyperborea Lingula, then just a small fraction of the sediment is required, which could potentially be sourced directly from erosion of the reentrant. It is also important to note that given long enough exposure time, eroded BU material may have been removed via saltation and transported into the circumpolar erg [*Tanaka and Hayward*, 2008].

Another interesting morphology associated with the reentrant adjacent to Chasma Boreale is an aligned series of deflections and terminations of spiral troughs forming a roughly linear ridge in the modern NPLD topography above the southern edge of the reentrant. This topographic ridge directly overlays the reentrant boundary (Figure 14a,b). While the fate of the removed sandy material is still unresolved, it is evident that the reentrant, and therefore BU topography, impacted deposition of the overlying NPLD at this location, creating a linear scarp aligned with the reentrant's border. This is a clear example of BU topography being directly responsible for modern ice cap features.

A third reentrant is located at ~132° E, 85° N (Figure 7 and Figure 14c,d). This reentrant differs from the first two because there is no evidence for an associated circumpolar deposit. There are, however, several cavi unit exposures nearby in the Olympia Cavi region. The presence of cavi unit near a reentrant is consistent with hypotheses that eroded rupes unit forms Planum Boreum cavi unit. This reentrant is nearly circular with an opening at the southern edge. While the nearest unconsolidated

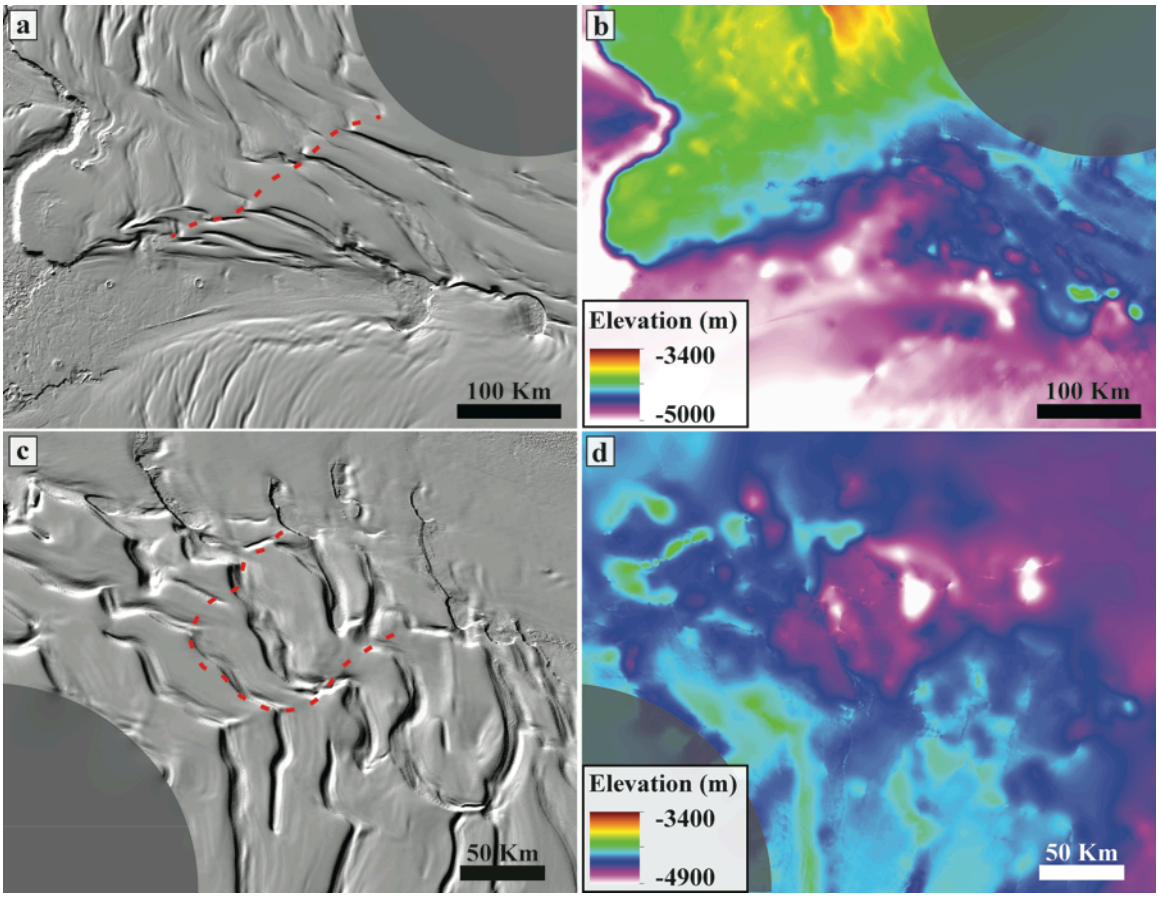

Figure 14. (a) Shaded-relief image created from MOLA topography showing the edge of the reentrant adjacent to Chasma Boreale with a dashed red line. Note how this line follows a linear ridge in the modern topography. (b) Colorized BU topography for the reentrant within Chasma Boreale. (c) MOLA-derived, shaded-relief image showing Olympia Cavi reentrant outline in dashed red. The outline of the reentrant is coincident with irregular trough morphology. (D) Colorized BU topography for the Olympia Cavi reentrant. Location for a,b and b,c is given in **Figure 2**.

sedimentary deposit is Olympia Undae, which may or may not have been sourced in part by the creation of this reentrant, this feature does have a visible impact on the overlying NPLD, similar to the reentrant adjacent to Chasma Boreale. At the northern edge of this reentrant, the NPLD exhibits a similar pattern of concentric ridges that follow the reentrant outline (Figure 14c). Prior work based on imagery mapped surface features similar to grabens in this location [*Tanaka et al*., 2008]. A graben-like surficial signature has not been identified elsewhere on Planum Boreum [*Tanaka et al*., 2008], yet is found in direct proximity to a BU reentrant. Therefore, it is possible that relief associated with the subsurface BU reentrant at this locale is responsible for unique NPLD deposition and surface features. Of the nine mapped graben features in *Tanaka and Fortezzo* (2012) seven are within the bounds of this reentrant while the remaining two are nearby to the southwest. BU reentrants appear to alter NPLD deposition, creating features found nowhere else on Planum Boreum. In addition, the observed vertical translation of antecedent topography is consistent with aeolian rather than glacial processes.

1.5.5 Katabatic wind modeling with BU topography

Investigation of Planum Boreum's BU has revealed features commonly associated with erosion, such as reentrants and steep troughs. We have attributed this erosion to wind, as modern processes indicate wind is actively reworking the NPLD [*Howard*, 2000; *Smith and Holt*, 2015]. However, this claim can be tested, or at least qualitatively verified by modeling winds as influenced by basal unit topography. A unique application

of our detailed BU mapping has therefore been the modeling of paleo-wind regimes. Assuming modern atmospheric conditions, the modeled winds using BU topography (Figure 9) generally agree with modern wind vectors [*Spiga et al*., 2011a]. It is important to remember that the BU topography used in this modeling is the result of substantial erosion and has likely evolved with aeolian forces. A few important differences between our BU wind maps and modern wind maps do exist, however, and these are primarily above the BU reentrants.

As discussed by *Brothers et al*. (2013), modeled paleo-winds over Abalos where the Abalos Mensa deposit now exists are almost nonexistent, in stark contrast to the modern wind fields that are strongly influenced by the current Abalos Mensa mound. Modern wind fields show katabatic winds flowing down and away from Abalos Mensa [*Spiga et al*., 2011a]. Without the mound's presence the model does not produce these additional katabatic winds. Another difference is along Chasma Boreale. As the chasma had not yet been constructed at the time of BU deposition [*Holt et al*., 2010], the winds through this region are not deflected down the chasma but are instead deflected through a reentrant within the BU, until they later follow the boundary that becomes the chasma. However, the deflection caused by the BU reentrant is minor and most of the wind is still traveling parallel to modern Chasma Boreale even at this stage in deposition. Thus, it is possible that conditions for creating a chasma at this location (by reducing or preventing accumulation) were already in place once BU reworking ceased. An outstanding question, however, is why the large reentrant adjacent to Chasma Boreale was completely filled in by NPLD deposition.

Wind maps created using this paleo-surface provide a test for our depositional scenarios. In addition, the modeled winds here offer a direct comparison to modern wind regimes. An interesting discovery has been that modeled ancient winds dominantly agree with modern winds and thus modern topographic features. Although we have used modern atmospheric parameters, winds are likely dominated by the topography. Therefore, while local variations exist, it is unlikely that the dominant drivers of deposition and evolution of Planum Boreum have undergone significant change since the time of BU reworking. While a few depressions and reentrants have been filled, they have likely been filled by aeolian processes and reflect local climatic or atmospheric effects.

1.6 CONCLUSIONS

Detailed radar-derived stratigraphic mapping of Planum Boreum's BU has revealed it to be a highly asymmetric mound of ice- and lithic-rich material containing at least three major reentrant-like features. It is our conclusion that the large-scale asymmetry and the reentrant-like features are erosional in origin, likely occurring at the same geologic time as the major rupes erosion hypothesized by *Tanaka et al*. (2008), and coincident with cavi unit deposition.

The thickest mapped location for BU is offset from the thickest NPLD, and hence offset from the modern depocenter of Planum Boreum. While no explanation for the offset is offered in our work, we do offer a plausible hypothesis for the creation of the

irregular BU morphology, derived solely from katabatic winds and impact ejecta armoring.

To qualitatively investigate the role of winds in forming modern and ancient Planum Boreum, we modeled paleo-winds with a mesoscale atmospheric model and studied the NPLD surface expression above BU reentrants. The BU reentrants deflect and funnel katabatic winds. The deflection of winds caused by reentrants has left a signature in modern ice deposits. Ice at each location has unique aligned series of spiral trough deflections and terminations associated with the outline of the underlying BU reentrant. In addition, these features are concentrated around the BU reentrants; similar features are seldom found elsewhere. As there exists correlation between a unique subsurface topography and modern topography, we hypothesize that the same wind-based parameters for ice deposition have been ongoing since the end of rupes unit erosion. This is supported by the extensive geological evidence for aeolian influence in the cavi [*Herkenhoff et al*., 2007; *Tanaka et al*., 2008; *Kocurek and Ewing*, 2012].

The results of this work emphasize that current Planum Boreum depositional processes involving the NPLD are very similar, if not the same as, older depositional processes involving the BU. Reentrants exist in both deposits, as do unique morphologies that correlate between the two. Detailed BU mapping has provided new insights into ancient topography that controlled katabatic winds and thus heavily influenced the deposition of water ice on Mars' north pole. The results of this study provide constraints for the evolution of Planum Boreum, and hypothesize a regime where

wind is the primary force mobilizing and reworking material to generate the modern ice cap from the top of the BU until the present.

Chapter 2: Orbital radar, imagery, and atmospheric modeling reveal an aeolian origin for Abalos Mensa, Mars[2]

2.1 INTRODUCTION

Abalos Mensa is a lobate wedge of material near the martian north pole, directly south of Rupes Tenuis at the edge of Planum Boreum (PB) at 285°E longitude. This feature measures ~180 km across and is separated from PB by a narrow chasmata on the east and a broad chasmata containing dune fields on the west (Figure 15a). Based on limited visible exposures of its stratigraphy, Abalos Mensa has been assumed to be composed of icy north polar layered deposits (NPLD) and both sand-rich members of the "basal unit," a term that combines the rupes and PB cavi units [*Byrne and Murray*, 2002; *Tanaka et al*., 2008]. The stratigraphic column for this region starts below the ice cap with the regional "basement," Vastitas Borealis Formation, and then begins incorporating icy material (Figure 3). The oldest ice-rich unit is the rupes unit, followed by the PB cavi unit [*Tanaka et al*., 2008]. These two units comprise what is often referred to as the "basal unit" [*Byrne and Murray*, 2002]. Following the basal unit is the NPLD material. The basal unit material is only visible on the western flank of Abalos Mensa [*Tanaka et al*., 2008].

Abalos Mensa is unique as an anomalously large, isolated mound proximal to PB. It has a morphology that has invoked multiple, distinct processes to explain its formation. Understanding its history is therefore key to evaluating past climate and constraining both the nature and timing of processes that have occurred on Mars.

---

[2] The material presented in this chapter is a modified version of the Geophysical Research Letters publication: Brothers, T. C., J. W. Holt, and A. Spiga (2013), Orbital radar, imagery, and atmospheric modeling reveal an aeolian origin for Abalos Mensa, Mars, Geophys. Res. Lett., 40, 1334–1339, doi:10.1002/grl.50293.

Prior work on ascertaining the origin of Abalos Mensa can be broken into two major hypotheses. The first is based on geomorphology; it ascribes this landform and the surrounding features to subglacial volcanoes, i.e. interactions of volcanoes/geothermal heat sources with ice [*Fishbaugh and Head*, 2002; *Hovius et al*., 2008]. Either the mound was deposited as a result of slumping following ice melt, or the mound is in-place but carved from a more extensive deposit via fluvial action, with the chasmata representing former flow channels [*Fishbaugh and Head*, 2002; *Hovius et al*., 2008]. To support this argument, nearby conical landforms have been compared to terrestrial shield volcanoes [*Garvin*, 2000b], streamlined mounds have been identified in the western chasmata [*Hovius et al*., 2008], and the morphology of channels in the chasmata has been characterized as sinuous [*Fishbaugh and Head*, 2002]. These hypotheses suggest that Abalos

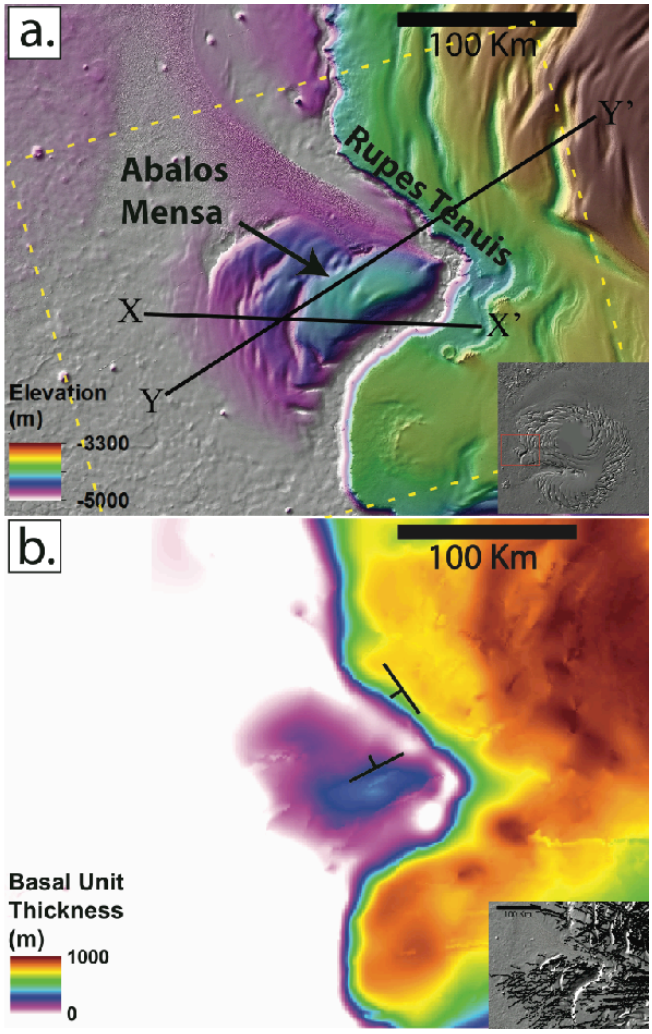

Figure 15. (a) Context map for study area including Abalos Mensa and Rupes Tenuis with the location of the two radargrams shown in **Figure 16**. Inset shows location on Planum Boreum. Dashed yellow box is location for **Figure 19**, the modeling results. (b) Thickness map of basal unit derived from subtracting surrounding plains elevation (-4900m) from a gridded basal unit elevation map. Note the steep scarp and small isolated deposit of basal unit material. Strike and dip symbols show average strike for basal unit layers at both Rupes Tenuis and Abalos Mensa. Inset shows SHARAD data points used in mapping basal unit topography.

Mensa is relatively recent (Middle to Late Amazonian), with *Hovius et al*. (2008) prescribing a maximum age of 20,000 years, since Abalos Mensa could have only formed after significant NPLD deposition.

The second hypothesis is based on visible stratigraphy, in particular the presence of basal unit beneath NPLD within Abalos Mensa. In this scenario, the rupes unit (the lower member of the "basal unit" as described by [*Byrne and Murray*, 2002]) was more extensive in this region (i.e., a continuous deposit across the location of present-day Abalos Mensa) prior to the widespread erosion that created Rupes Tenuis [*Tanaka et al*., 2008; *Warner and Farmer*, 2008b; *Kneissl et al*., 2011]. Impact shielding at the location of Abalos Mensa as well as along Rupes Tenuis locally prevented the rupes material from eroding away. Impact shielding causes the material surrounding an impact crater, often covered by ejecta, to become armored and erosionally resistant [*Arvidson et al*., 1976]. The shielding of Abalos Mensa and additional impact shielding along Rupes Tenuis left an isolated mound and the steep scarp [*Tanaka et al*., 2008]. Later deposition of NPLD added to this mound. This implies that the shielded rupes unit should underlie most, if not all, of the deposit [*Tanaka et al*., 2008] and requires Abalos Mensa to be an Early Amazonian deposit (i.e. much older than assumed in the fluvial hypothesis).

Both hypotheses require a pre-existing deposit in order to form Abalos Mensa, yet involve vastly different processes and timing. Melting, fluid flow and possibly slumping isolate the deposit in the first hypothesis, while impact shielding combined with aeolian erosion is responsible in the second. This work challenges these hypotheses by examining the internal structure and stratigraphy of Abalos Mensa using a combination of high-resolution imagery, orbital radar sounding, digital elevation models (DEMs), and atmospheric modeling. Internal stratigraphy was unavailable in previous studies and gives additional constraints on formation mechanisms. The result is a new hypothesis,

based solely on atmospheric processes, for both the timing and mechanism of Abalos Mensa formation. This scenario has important implications for the role played by the atmosphere in the evolution of polar landforms on Mars.

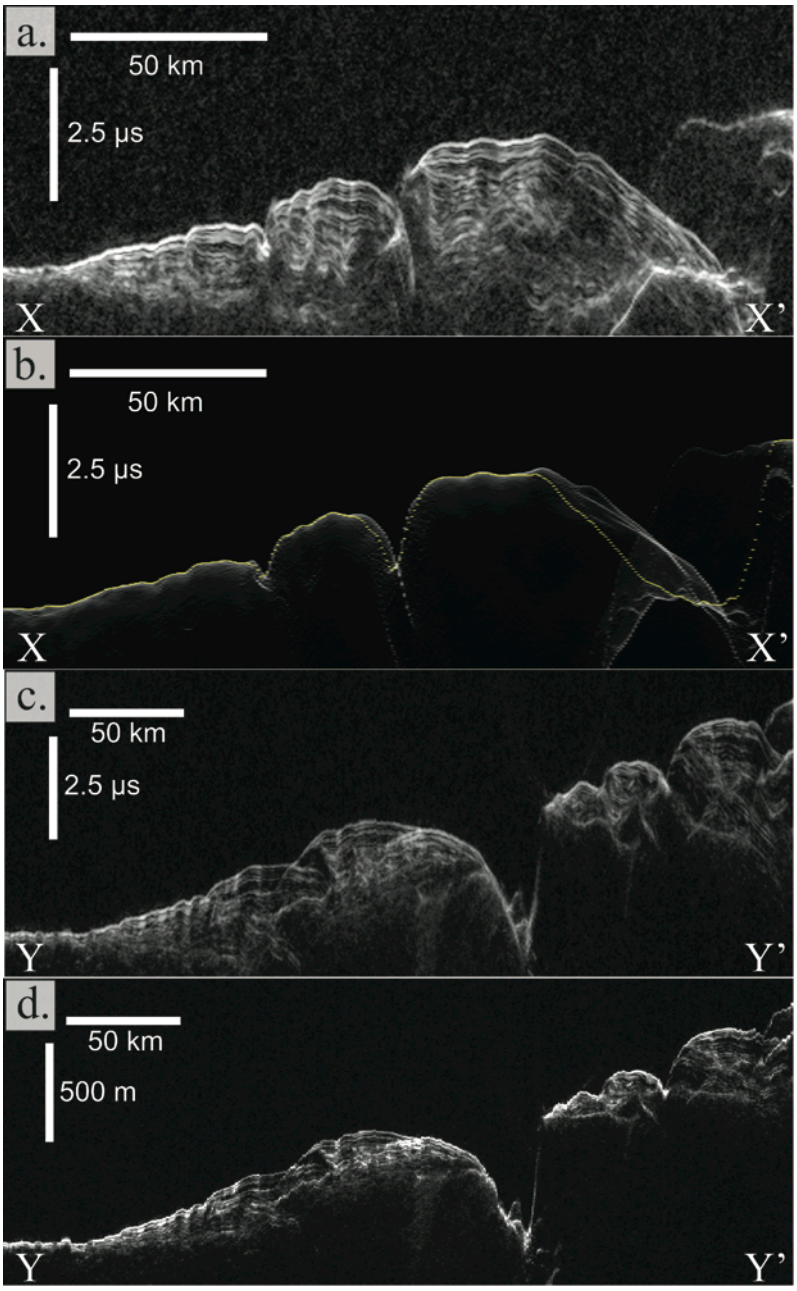

Figure 16. Mars (a) SHARAD observation 1612601000 in time delay. Only NPLD is visible in this radargram. Note reflector downlap onto Vastitas Borealis Formation both near the chasmata and on opposite side. (b) Radar surface clutter simulation for SHARAD track 1612601000. Yellow line shows calculated position of echo from ground track based on MOLA topography. This simulation demonstrates that the reflectors within Abalos Mensa are not generated from off nadir surface echoes. (c) SHARAD observation 622902000 in time delay. This is located very near the thickest part of the mapped basal unit deposit (Fig. 1b) within Abalos Mensa. NPLD layers truncate onto the basal unit and no additional reflectors are visible within the basal unit. (d) SHARAD observation 622902000 in depth using a dielectric constant of 3.15 to convert from time. Note how the reflector geometry is altered when correcting for depth.

2.2 DATA AND METHODS

A relatively new tool in planetary exploration is orbital radar sounding. The Shallow Radar (SHARAD) on Mars Reconnaissance Orbiter provides a detailed subsurface view of PB (see Figure 16) including internal stratigraphy that has provided important new insights into polar cap structure [*Phillips et al*., 2008; *Putzig et al*., 2009] and stratigraphy [*Holt et al*., 2010; *Smith and Holt*, 2010]. We used SHARAD data to examine the internal stratigraphy of Abalos Mensa and to map the upper surface of the basal unit across Planum Boreum, including Abalos Mensa. SHARAD is centered at 20 MHz frequency with 10 MHz bandwidth, yielding a theoretical vertical resolution of 8.4 m in pure water ice [*Seu et al*., 2007]. Horizontal resolution is typically 0.3-1 km along track, and 3-6 km across track. SHARAD has dense coverage on the north pole, with more than 3000 SHARAD observations over PB and approximately 150 observations that cross Abalos Mensa. In order to confirm radar reflectors as representing subsurface interfaces, we compared radargrams to forward simulations of surface clutter (Figure 16b) [*Holt et al*., 2006]. These forward simulations were based on DEMs of the surface derived from the Mars Orbiter Laser Altimeter (MOLA) on Mars Global Surveyor [*Smith et al*., 2001]. To create a DEM of the polar paleo-topography, mapping results from the SHARAD data were exported, geographically positioned, and then gridded. To convert radar echo time delays to depth below the surface, we assumed a dielectric constant of 3.15, consistent with the water ice composition determined for the bulk NPLD [*Phillips et al*., 2008; *Grima et al*., 2009]. However, changing the dielectric constant will not significantly affect the relative geometries of layers, only their total thickness values. To illustrate this idea I model Abalos Mensa's internal structure with different permittivities [*Phillips et al*., 2011; *Lauro et al*., 2012] in Matlab and include those results in Figure 17. The code used to generate this figure is included in Appendix A.

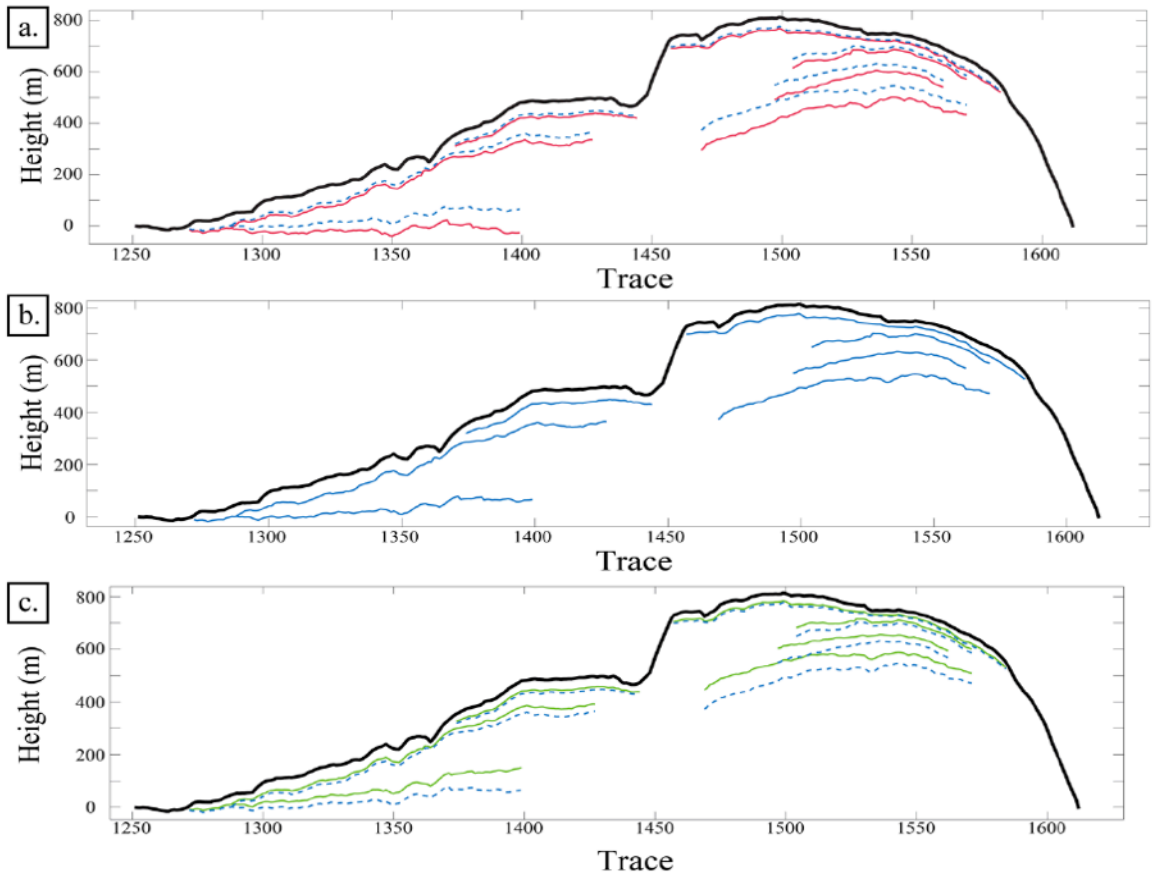

Figure 17. Stratigraphy interpreted from SHARAD radargram 622902 showing the influence of dielectric constant when converting SHARAD stratigraphy to depth. Location of this orbit can be found in **Figure 15**, **Figure 16** includes additional information. a) Stratigraphy shown in red was converted using a dielectric constant of 2.11 (~CO_2 ice [*Phillips et al.*, 2012]) while the background dashed blue lines show the conversion using a dielectric of 3.15 (water ice). b) Conversion to depth using a dielectric constant of 3.15, the same used in this study's results. c) Green stratigraphy show a depth conversion using a dielectric of 5, an estimate for the basal unit material [*Lauro et al.*, 2012], the dashed blue line is the conversion using 3.15.

While SHARAD detects NPLD stratigraphy and the underlying basal unit topography, it does not typically detect bedding within the basal unit. Therefore, imagery from the High Resolution Imaging Science Experiment (HiRISE) [*McEwen et al.*, 2007] and Context Camera (CTX) [*Malin et al.*, 2007] on MRO was used to map basal unit layering on exposed surfaces. Layers were chosen based on continuity, visibility resulting from albedo contrast, distance of exposure, and topographic expression.

Preference was given to layers with higher albedo contrast and greater resistance to erosion. Imagery was geo-located and draped on DEMs from both MOLA and the High Resolution Stereo Camera (HSRC) on Mars Express [*Neukum and Jaumann*, 2004].

Bouding Surface	**Image**	**DEM**	**Longitude**	**Latitude**	**Elevation**
009367-1	PSP_009367_2620_RED	HRSC	282.745321	81.693448	-4725
009367-1	PSP_009367_2620_RED	HRSC	282.743214	81.694279	-4739
009367-1	PSP_009367_2620_RED	HRSC	282.742252	81.696438	-4721
009367-1	PSP_009367_2620_RED	HRSC	282.732124	81.700365	-4742
009367-1	PSP_009367_2620_RED	HRSC	282.722553	81.701948	-4742
009367-1	PSP_009367_2620_RED	HRSC	282.726336	81.703627	-4746
009367-1	PSP_009367_2620_RED	MOLA	282.74395	81.693762	-4611.25
009367-1	PSP_009367_2620_RED	MOLA	282.740103	81.697497	-4627.5
009367-1	PSP_009367_2620_RED	MOLA	282.722619	81.701897	-4649.25
009367-1	PSP_009367_2620_RED	MOLA	282.726381	81.703588	-4616.75
009367-2	PSP_009367_2620_RED	HRSC	282.74934	81.742235	-4749
009367-2	PSP_009367_2620_RED	HRSC	282.734861	81.743195	-4769
009367-2	PSP_009367_2620_RED	HRSC	282.740575	81.745518	-4752
009367-2	PSP_009367_2620_RED	HRSC	282.759023	81.740334	-4725
009367-2	PSP_009367_2620_RED	MOLA	282.748942	81.742226	-4652.75
009367-2	PSP_009367_2620_RED	MOLA	282.735036	81.743239	-4674
009367-2	PSP_009367_2620_RED	MOLA	282.739991	81.74537	-4659.5
009367-2	PSP_009367_2620_RED	MOLA	282.759023	81.740334	-4627
009367-3	PSP_009367_2620_RED	HRSC	282.738381	81.743314	-4769
009367-3	PSP_009367_2620_RED	HRSC	282.744482	81.76772	-4747
009367-3	PSP_009367_2620_RED	HRSC	282.678581	81.777951	-4755
009367-3	PSP_009367_2620_RED	MOLA	282.738818	81.743353	-4652.75
009367-3	PSP_009367_2620_RED	MOLA	282.744562	81.767739	-4671.75
009367-3	PSP_009367_2620_RED	MOLA	282.67881	81.777941	-4657.5
010646-1	PSP_010646_2620_RED	HRSC	276.808252	81.737996	-4722
010646-1	PSP_010646_2620_RED	HRSC	276.910357	81.750049	-4658
010646-1	PSP_010646_2620_RED	HRSC	276.951978	81.758158	-4594
010646-1	PSP_010646_2620_RED	MOLA	276.809616	81.73811	-4654.75
010646-1	PSP_010646_2620_RED	MOLA	276.910481	81.750029	-4656.25
010646-1	PSP_010646_2620_RED	MOLA	276.952378	81.75819	-4619.5
010646-2	PSP_010646_2620_RED	HRSC	276.369349	81.70548	-4645

Table 3. continued next page.

010646-2	PSP_010646_2620_RED	HRSC	276.434832	81.710363	-4677
010646-2	PSP_010646_2620_RED	HRSC	276.484288	81.713073	-4669
010646-2	PSP_010646_2620_RED	HRSC	276.498565	81.714197	-4683
010646-2	PSP_010646_2620_RED	MOLA	276.369349	81.70548	-4548.25
010646-2	PSP_010646_2620_RED	MOLA	276.434832	81.710363	-4559.25
010646-2	PSP_010646_2620_RED	MOLA	276.484288	81.713073	-4584.25
010646-2	PSP_010646_2620_RED	MOLA	276.498565	81.714197	-4584.5

Table 3. Data used in basal unit layering calculations at Abalos Mensa and Rupes Tenuis scarp.

Basal unit optical layer analysis						
HiRISE Image	Location	MOLA Aspect	HRSC Aspect	MOLA Dip	HRSC Dip	Line Length
009367-1	Abalos Mensa	335	347	18.3	5.5	530 m
009367-2	Abalos Mensa	340	338	14.1	13.5	421 m
009367-3	Abalos Mensa	*(330)*	322	2.3	1.9	2,300 m
010646-1	Rupes Tenuis	223	239	14.2	12.3	597 m
010646-2	Rupes Tenuis	233	225	18.5	8.9	1,710 m

Table 4. Optical basal unit bedding analysis results. Boundary layer dip and dip direction measurements derived from HiRISE imagery draped on MOLA 512 pixel per degree and HRSC H1264_0000_DA4 DEMs. Parenthetical number indicates low confidence in the measurement, as single pixel changes for elevation points noticeably affect this value.

HRSC data were necessary because of the comparatively low resolution of smoothed MOLA data. Both report resolutions near 100 meters per pixel in the northern regions (HRSC is 125 meters per pixel and MOLA is 512 pixels per degree), but MOLA smoothing made an obvious difference between the two products. Large features that are apparent in the imagery are missing from MOLA DEMs and present in their HRSC counterpart. While layering picks on the imagery spanned many pixels, they often did not cover more than one or two changes in MOLA elevation. It is for this reason that results are reported for both the HRSC DEM and the MOLA DEM independently. Elevation data is included for each mapped layer in Table 3. The extracted elevation data were then gridded to calculate bedding attitude for each layer (Table 4).

To complement observational data analysis, the mesoscale atmospheric model of *Spiga and Forget* (2009) was used to qualitatively evaluate winds possibly involved in the formation of Abalos Mensa. We assume that winds are fundamental to the erosion and/or deposition of dust and ice particles at the surface. Recent observations posit this mechanism is at play [*Smith and Holt*, 2010; *Appéré et al*., 2011]. Whether the removal process is mechanical erosion or enhanced sublimation is an open question; furthermore, thresholds of wind velocity for either erosion or deposition depend on many unconstrained parameters. Such determinations are beyond the scope of this study; however the relative magnitude and the spatial pattern of modeled winds provides useful information relevant to those processes. It is certainly clear that with stronger near-surface winds, erosion would be enhanced and deposition less likely.

The mesoscale model simulates atmospheric circulation with a horizontal resolution of approximately 5-10 kilometers, suitable to assess typical regional wind regimes in the vicinity of Abalos Mensa. The model was run over a domain encompassing the north polar region (see section 7.2 in [*Spiga et al*., 2011b]). Present-day obliquity and conditions were assumed, except that modern topography was replaced with the ancient SHARAD derived basal unit topography (Figure 7). No spurious effects in model predictions arise from this change, given the method employed to produce a high-resolution initial state from low-resolution global climate runs (cf. section 2.3.4 in Spiga and Forget 2009). Running a polar mesoscale model in present-day conditions except for the topography is a simple approach, closer to idealized modeling than real-case numerical weather prediction. However, it allows us to obtain results quantitative to the first order and to model, for the first time, paleo-wind conditions from a geophysically-derived paleo-surface on Mars. This is possible because near-surface regional winds in polar regions are primarily controlled by slope-induced acceleration

and Coriolis forcing, as shown both by mesoscale modeling and frost streak mapping [*Howard*, 2000; *Massé et al*., 2012].

2.3 RESULTS

The radar analysis of Abalos Mensa, and PB in general, provides a clear and unprecedented demarcation of basal unit extent beneath the overlying NPLD. The radar returns in the NPLD show distinct, bright, laterally continuous reflectors with very little echo power between reflectors [*Phillips et al*., 2008]. Where basal unit underlies NPLD, there is generally a sharp transition to diffuse scattering at the base of the NPLD, presumably due to increased complexity at the wavelengths of SHARAD (Figure 16) [*Putzig et al*., 2009].

The NPLD radar reflectors within Abalos Mensa exhibit clear downlap onto the underlying Vastitas Borealis Formation (Figure 16a). Radar layers have maximum thickness near the center of Abalos Mensa and gradually thin as they downlap onto either the Vastitas Borealis Formation or the basal unit. Abalos Mensa radargrams show NPLD downlap directly onto Vastitas Borealis Formation both near the chasmata and at the southernmost edge, this is most apparent in radargrams lacking basal unit (Figure 16).

SHARAD mapping also shows that basal unit extent beneath Abalos Mensa is much more limited than was hypothesized in prior work [*Tanaka et al*., 2008] and found primarily beneath the north-western half of Abalos Mensa (Figure 15b). The only basal unit identified in imagery at Abalos Mensa is a small deposit on the western half [*Tanaka et al*., 2008]. The basal unit is near maximum thickness here based on the radar data. At

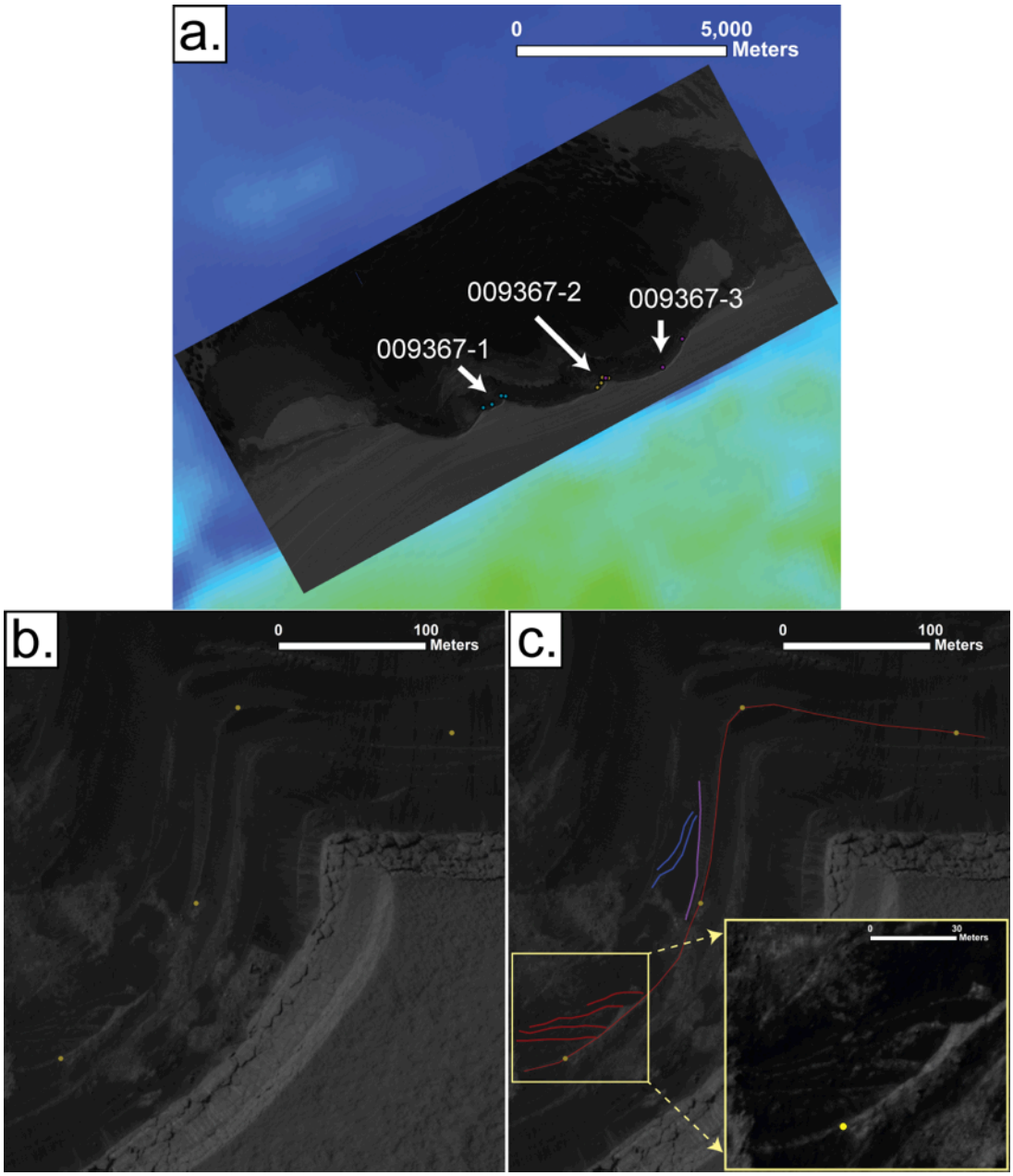

Figure 18. Mars (a) Context for HiRISE image PSP_009367_2620_RED on top of HRSC DEM H1264_0000_DA4. Arrows point to three bounding surfaces on this image that were interpreted and gridded within GIS software. (b) Zoom on bounding surface 009367-2 with data points from Auxiliary Table 1 in yellow. (c) Interpreted bounding surface 009367-2 shown connecting the yellow data points. Cross-strata intersecting the bounding surface and typical of cavi unit [Herkenhoff et al. 2007; Tanaka et al. 2008] are mapped in bright red. An additional layer reminiscent of a preserved dune form that intersects the red bounding surface is show in purple. Internal to the purple layer are additional strata mapped in blue. The boxed inset magnifies cross-strata and has been enhanced to aid in identification of bedforms. Bedforms such as these aided in reaffirming the classification of this outcrop as cavi unit.

this location the exposed basal unit has been identified as cavi using optical data [*Tanaka et al*., 2008]. No identification of rupes unit has been made using imagery at Abalos Mensa. Within HiRISE image PSP_009367_2620 there are clear examples of cross bedding and preserved bedforms in the basal unit deposit (Figure 18). This stratigraphy is consistent with the cavi unit and inconsistent with the rupes unit [*Herkenhoff et al*., 2007; *Tanaka et al*., 2008].

Our analysis of HiRISE and CTX data shows that bedding attitudes of bounding surfaces within the basal unit dip away from scarp exposures at both Rupes Tenuis and Abalos Mensa (Figure 15b and Table 4). This attitude is consistent with the overlying NPLD, which clearly downlap onto the Vastitas Borealis Formation. Additionally, the dip directions of basal unit layering in the western edge of Abalos Mensa are offset as compared with those exposed across the chasmata within the rupes unit exposed by Rupes Tenuis (Figure 19). This indicates that deposition was influenced by localized processes rather than continuous across the region prior to a hypothesized erosion event.

The wind modeling results (Figure 20) show sustained katabatic winds flowing downward across Rupes Tenuis, changing to low velocity in the region where Abalos Mensa now exists. The change in wind velocity is sudden, with winds leaving the scarp at ~ 10 m/s then slowing to only a few m/s where Abalos Mensa is located. These wind patterns are typical of those taking place during the whole day throughout the year at the edges of Martian polar caps; their amplitudes could however vary with large-scale weather conditions and surface ice cover.

2.4 DISCUSSION

Based on these new observations, the previous hypotheses do not adequately explain Abalos Mensa formation and evolution. Under the impact-shielding hypothesis, the majority of the deposit should be underlain with rupes basal unit material. However,

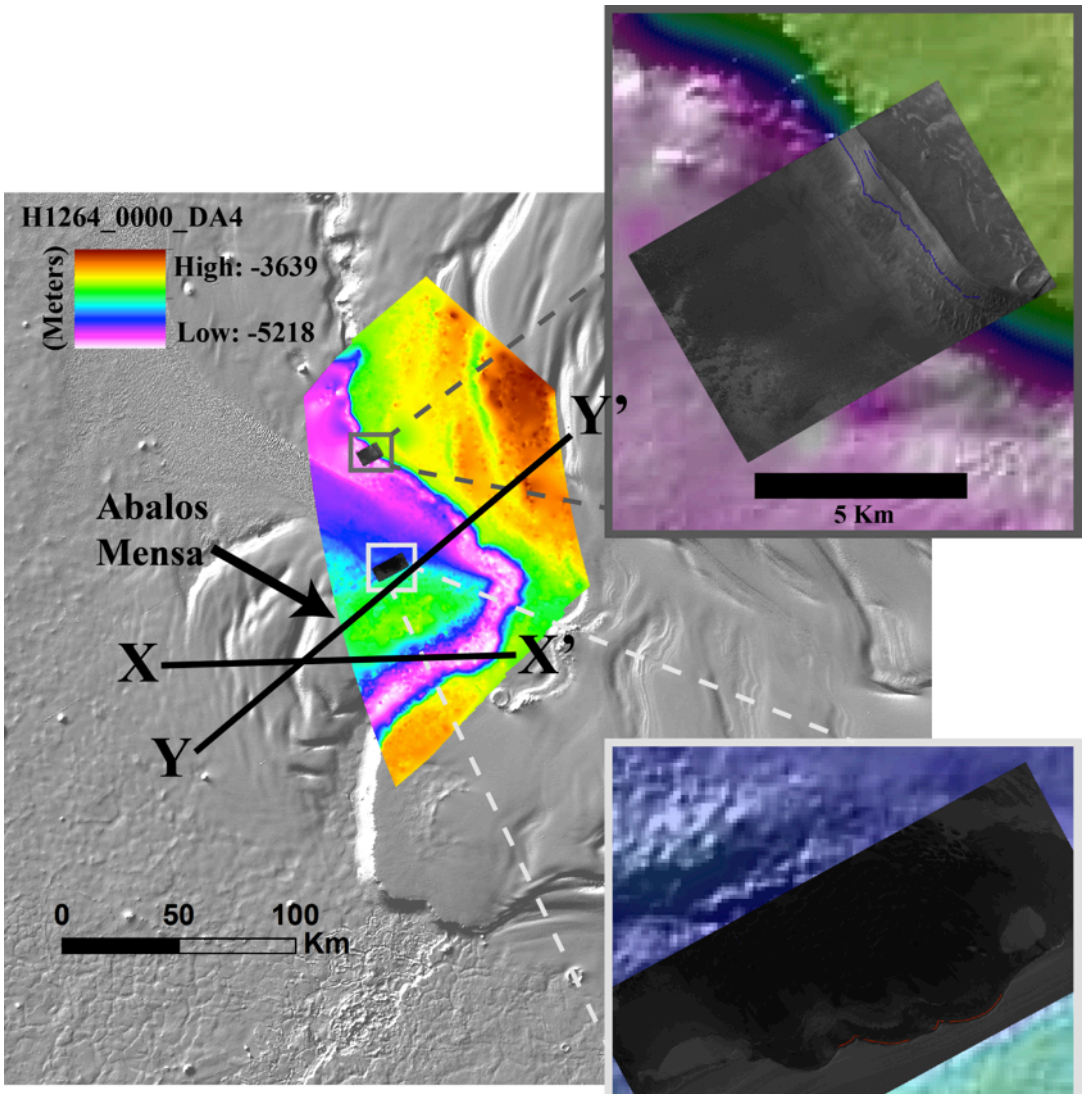

Figure 19. Location map of the HRSC DEM H1264_0000_DA4 used in this study. The locations of the HiRISE images used for bedding attitude analysis at both Rupes Tenuis and Abalos Mensa are also shown. Expanded view of HiRISE images show examples of picked bounding surfaces used to calculate layer attitudes.

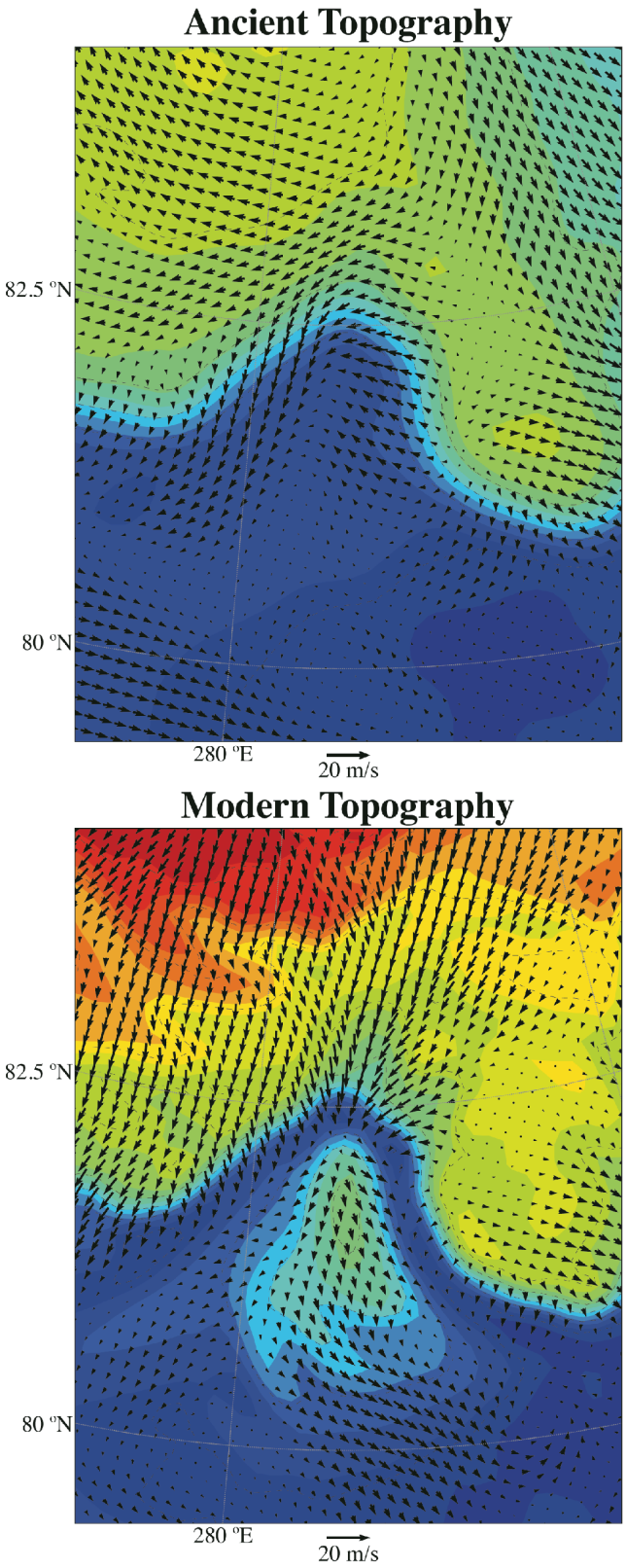

along the basal unit exposure on the western side of Abalos Mensa, no rupes was identified, only the younger basal unit member, PB cavi unit. Furthermore, the SHARAD-detected basal unit is nearly at maximum thickness along this exposure and its areal extent is small relative to the entire Abalos Mensa formation. While we cannot exclude the possibility of any rupes unit existing beneath Abalos Mensa, we have confidence that if it does exist, it must be very thin, likely below the resolution of SHARAD, and limited

Figure 20. Mars Orbiter Laser Altimeter color shaded elevation map of Mars' north pole. Large features of interest have been labeled. (a) Wind modeling results from paleotopography showing local winds descending across Rupes Tenuis, before slowing down where the modern Abalos Mensa is located. The displayed area is a zoom on the Rupes Tenuis / Abalos Mensa region; the simulation domain encompasses the northern polar region with a horizontal resolution of approximately 7 kilometers. (b) Identical wind simulation but with modern topography instead of the SHARAD derived paleotopography.

in extent. This suggests that the entire basal unit deposit beneath Abalos Mensa is likely PB cavi unit. If no rupes unit is present beneath Abalos Mensa, then the formation is not contemporaneous with the rupes unit exposed in Rupes Tenuis, and the impact-shielding hypothesis is therefore insufficient.

The geometry of bedding, as indicated by HiRISE analysis of the cavi unit and SHARAD for the NPLD, is inconsistent with both the fluid flow and impact-shielding hypotheses. Both of these hypotheses assume that layers were once continuous across Rupes Tenuis and should therefore have very similar bedding attitudes. However, layers within basal unit material on each side of Rupes Tenuis are significantly offset rather than parallel or subparallel. While a melt scenario may explain a difference in dip and perhaps a small difference in strike, it does not account for large offset in layer strike. This further supports our contention that these are not the same units. Additionally, the NPLD is downlapping onto either Vastitas Borealis Formation or basal unit material. In an erosional scenario, one would expect visible SHARAD reflector truncation along the chasmata, yet the relationship is clearly dominated by depositional downlap. Therefore, as neither hypothesis is consistent with these new data, a new formation hypothesis appears necessary. We first review the critical observations.

The stratigraphy in Abalos Mensa from the NPLD and into the basal unit is consistent with localized deposition. Within the NPLD the radar data show clear downlap onto Vastitas Borealis, indicating in-place deposition. The underlying cavi unit has this same bedding attitude as overlying NPLD, indicating it formed in place as well. In general, the cavi unit exhibits a gradational contact with the NPLD [*Tanaka et al.*, 2008] and therefore deposition was likely continuous across the boundary of cavi to NPLD material at Abalos Mensa. The consistent bedding attitudes within Abalos Mensa support this relationship.

The mesoscale atmospheric model results, using the ancient basal unit topography and modern atmospheric conditions, are also qualitatively consistent with in-place formation and deposition of material in Abalos Mensa. The model shows katabatic winds, capable of material transport, descending across Rupes Tenuis toward modern Abalos Mensa where a significant drop in wind velocity occurs. The drop in velocity would reduce the wind's carrying capacity at the location of Abalos Mensa, making deposition feasible. Interestingly, mesoscale simulations with modern topography (section 7.2 of *Spiga et al*. 2011) show that, once the deposit reaches sufficient altitude above the surrounding surface, Abalos Mensa itself influences the local wind regime, which tends to mitigate the effects of atmospheric deposition that could have given birth to it.

This integration of new observational data from SHARAD, HiRISE, and HRSC combined with atmospheric modeling suggests an alternative explanation (Figure 21). We hypothesize that Abalos Mensa formed in place, essentially as it appears today, following the construction of Rupes Tenuis. As hypothesized in previous work, widespread erosion of rupes caused hundreds of kilometers of polar cap retreat [*Tanaka et al*., 2008; *Warner and Farmer*, 2008a; *Kneissl et al*., 2011]. However, erosion was inhibited along Rupes Tenuis due to impact shielding there, a hypothesis supported by the presence of partially buried impact craters [*Tanaka et al*., 2008]. This scarp locally amplified katabatic winds as they flowed down and away from the center of PB. However, once in the Abalos region, the winds lost velocity and thus their ability to carry ice and sediment. This caused deposition of cavi unit material, some of which may have been eroded directly from Rupes Tenuis. Rupes Tenuis and the Abalos chasmata are actively scoured by these katabatic winds keeping the chasmata open. As described by others [*Herkenhoff et al*., 2007; *Tanaka et al*., 2008] the cavi unit locally exhibits a

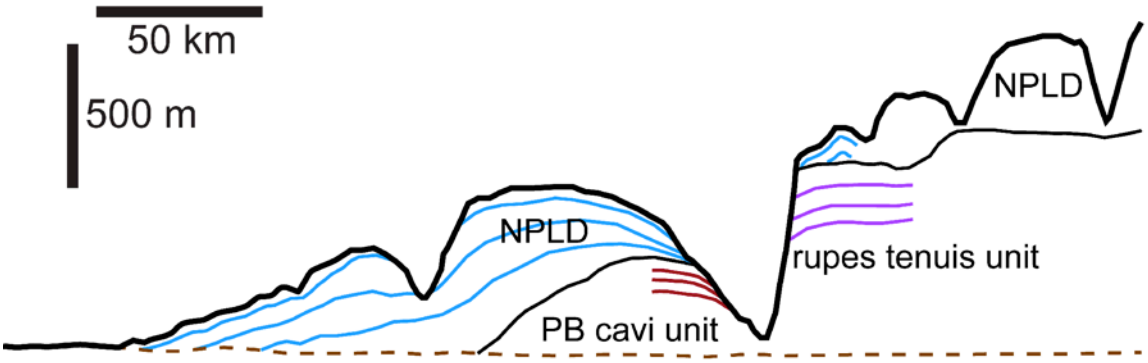

Figure 21. Interpretative cross section based on SHARAD observation 622902000 and basal unit layer attitudes derived from HiRISE imagery draped on HRSC DEM (see **Figure 19** and **Table 4**). Layers within both basal unit exposures dip away from their scarps and the thickest region of basal unit, indicating in-place deposition.

gradational contact with NPLD. Hence, the entire deposit was likely formed in an essentially continuous manner following widespread erosion of the rupes unit. As supported by the geologic transition from sand and ice stratigraphy to nearly pure ice stratigraphy, the end of rupes deposition and transition to cavi is also likely to represent a climatic change for this region. Therefore, the creation of Abalos Mensa occurred during a transitional period for Mars north pole deposits and possibly climate. This hypothesis will require further examination and atmospheric modeling to account for atmospheric compositions and obliquities in Mars' past, yet this explanation is consistent with a recent finding that nearby Chasma Boreale is a constructional feature that formed after regional basal unit erosion, rather than being created from the erosion of NPLD [*Holt et al.*, 2010].

Based on our results, the geological processes required for the formation of Abalos Mensa are essentially the same as those recently active at Mars' north pole: deposition, erosion, and atmospheric transport of material. No exotic processes are necessary to explain the formation of Abalos Mensa. This also indicates that at least since the time of widespread rupes erosion and subsequent cavi and NPLD deposition, estimated at ~ 1 Ga [*Tanaka et al.*, 2008], climate-related processes and resulting landform evolution at the north pole of Mars have likely undergone little change, at least

for this region on Planum Boreum. The present is therefore likely the key to the past, and we can learn much about paleoclimate and the long-term evolution of Mars landforms by further examining the processes active today.

Chapter 3: The timing and stability of north polar crater ice, Korolev Crater, Mars

3.1 Introduction and Background

The martian north pole is covered by a massive layered deposit of relatively pure water ice [*Howard et al*., 1982; *Malin and Edgett*, 2001; *Phillips et al*., 2008; *Grima et*

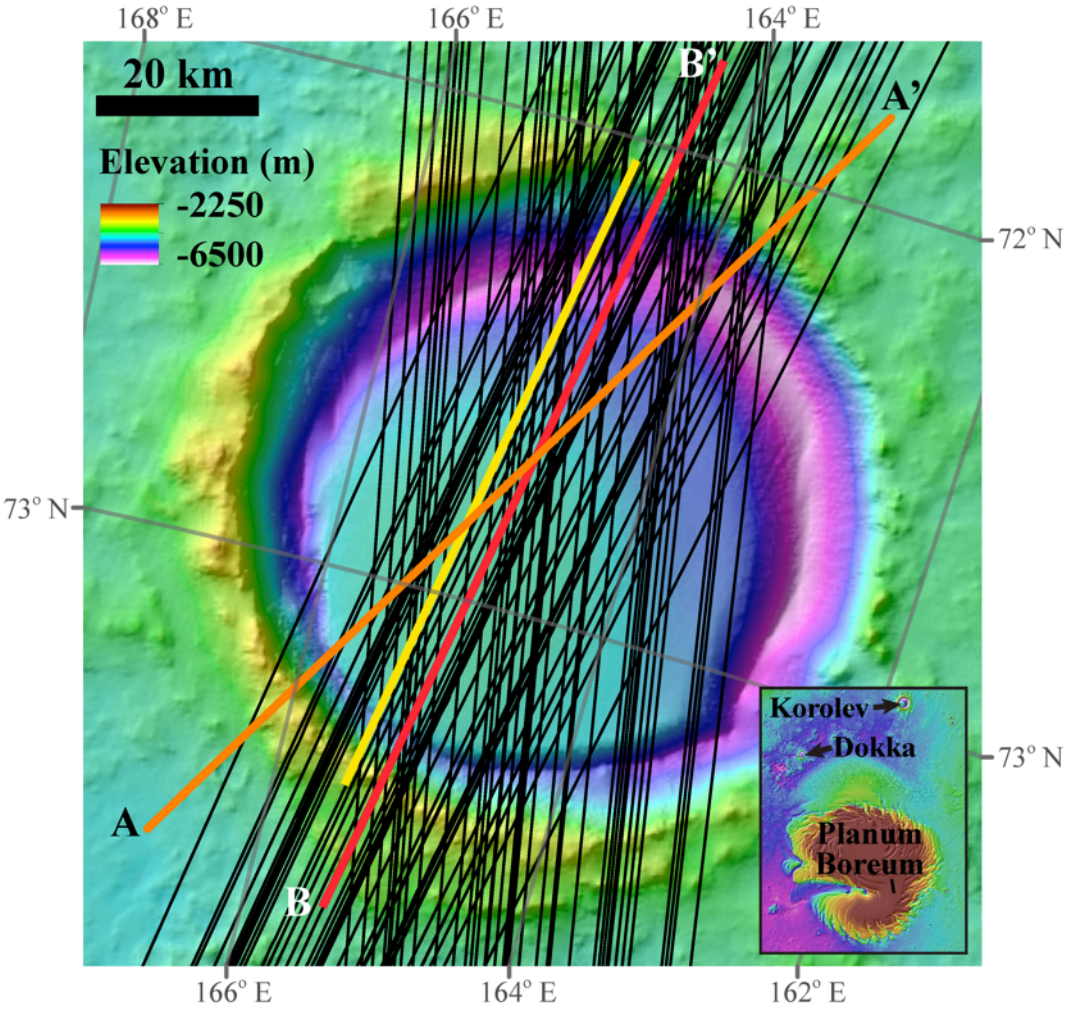

Figure 22. Topographic map of Korolev crater, based on Mars Orbiter Laser Altimeter data. The 69 radar observations used in the study are shown here as well as locations for the radargram shown in **Figure 23** (B-B', red line), the gridded reflector cross section shown in **Figure 26** (A-A', orange line), and the Korolev and NPLD packages shown in **Figure 28** (yellow line and small black line on Planum Boreum inset).

al., 2009]. Radar studies have used the stratigraphy of this deposit to further our understanding of its evolution and genesis [*Putzig et al*., 2009; *Selvans et al*., 2010; *Christian et al*., 2013]. These studies have revealed that many features of Planum Boreum are constructional, meaning they have been built from largely depositional processes [*Holt et al*., 2010; *Smith and Holt*, 2010; *Brothers et al*., 2013; *Smith et al*., 2013]. Emphasizing depositional rather than erosional conditions for Mars' northern ice makes it necessary to reassess the origin of circumpolar ice deposits such as those found in Korolev and Dokka craters (Figure 22). This work investigates whether circumpolar crater ice is more likely a remnant of a previous geologic epoch with a more extensive ice cap, or a relatively recent feature built by *in situ* deposition [*Fishbaugh and Head*, 2000; *Garvin*, 2000a; *Tanaka et al*., 2008; *Conway et al*., 2012]. Each scenario should have a unique stratigraphic signature that can be analyzed with radar sounding.

Current climatic conditions permit stable water ice at the surface on Mars' north pole; however, south of 90º ice stability decreases [*Levrard et al*., 2004; *Madeleine et al*., 2009]. The latitudinal dependence of ice stability has been used as evidence to support an ancient origin for circumpolar ice [*Fishbaugh and Head*, 2000], which, it is argued could not have formed in the modern regime. Located at 72.7º N, 164.5º E, 600 km south of Planum Boreum's edge, the Korolev impact crater falls nearly on but south of the perennial ice stability line, which at 72.7º N 164.5º E is at approximately 74º N [*Levrard et al*., 2004]. The presence of water ice in Korolev [*Kieffer and Titus*, 2001; *Armstrong et al*., 2005] has therefore been regarded as enigmatic. As a result, distinction between ancient and modern Korolev ice has two end members. If the ice is older than the last 5 million years, current hypotheses suggest it was part of a widespread icecap [*Fishbaugh and Head*, 2000] and the internal stratigraphy will reflect that; however, if the ice is modern it must be stable in the current climate regime and could not have formed as part

of a massive ice cap expansion. If modern conditions permit ice deposition in circumpolar landforms, it is unnecessary to invoke ancient remnant ice. This study uses orbital sounding radar to map the stratigraphy of the nearly 2 km thick water ice deposit in Korolev crater [*Moore et al*., 2012] in order to analyze the stratigraphic architecture of Korolev and assess its origin.

In addition to radar analysis, this study uses a scaled modeling experiment to assess the stability of water ice at Korolev. Hypothetically, such modeled constraints for ice deposition in circumpolar deposits are not limited to Korolev but are also inclusive of other landforms such as Dokka crater (Figure 22). These results are therefore relevant to Mars' global water cycle: is ice no longer stable in Korolev, or are we in a regime still favorable to ice deposition or preservation? This study addresses our fundamental understanding of ice on Mars and conducts a modeling experiment at Korolev crater to unveil additional constraints for circumpolar ice deposits.

3.2 Data and Methods

Radar data for this study are from Shallow Radar (SHARAD) on Mars Reconnaissance Orbiter. SHARAD is an orbital radar sounder centered on 20 MHz frequency with a 10 MHz bandwidth [*Seu et al*., 2007]. SHARAD penetrates the surface of icy martian deposits, reflecting from subsurface permittivity variations. These reflectors create time delay surfaces representative of isochrons. While SHARAD reflectors do not map directly to optical layers, they have been shown to strongly correlate with optical layering [*Christian et al*., 2013]. The theoretical vertical resolution of SHARAD is 8.4 m in water ice and SHARAD's spatial footprint is 3-6 km across track, and compressed to 0.3-1 km in the along-track direction via focusing [*Seu et al*.,

2007].

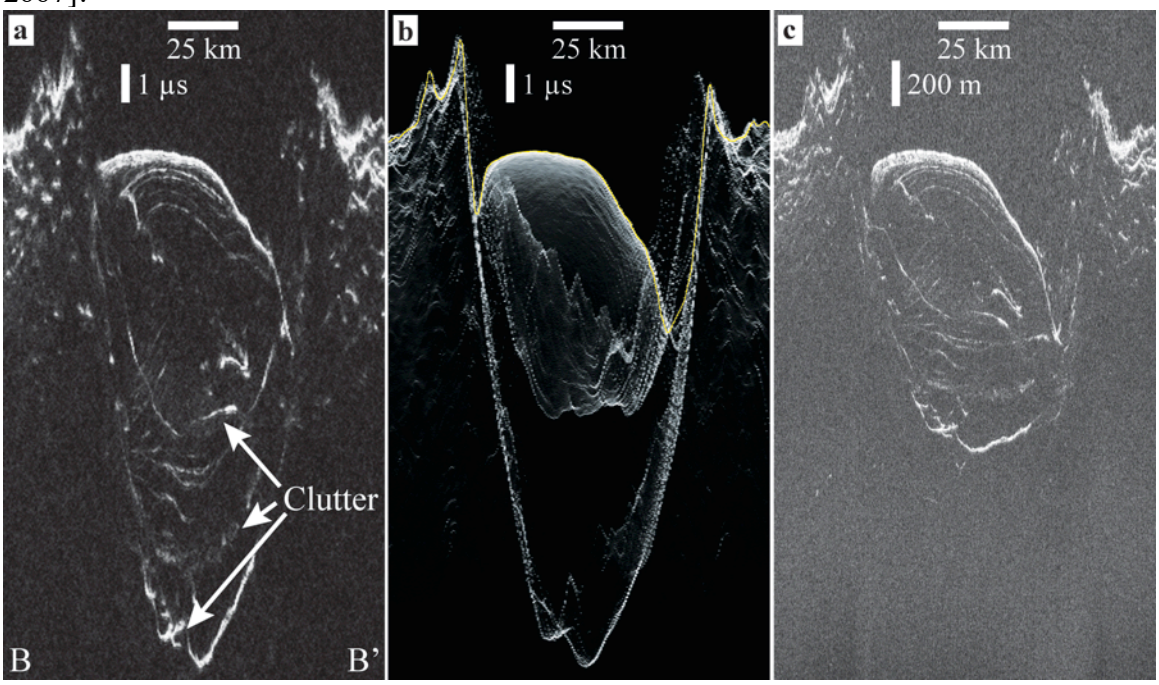

Figure 23. Radar observation 2342201000 crossing Korolev. Location for this radargram is given by the red line in Figure 22. North is to the left. (a) Time-delay radargram with bright near-surface reflectors and several deep reflectors. Time is shown in one-way travel. (b) Clutter simulation showing echoes resulting only from surface topography. All reflectors in radargram matching those in this simulation are not subsurface and must be avoided when mapping reflectors. (c) Depth corrected radargram using the permittivity of water ice (3.15). Notice how the geometry of the radar reflectors at depth drastically changes after conversion to the depth domain.

SHARAD data have been acquired since 2007 with more than 15,000 observations recorded. Over 100 orbits have acquired data over Korolev crater's central mound (Figure 23). Maps for this study were constructed using 69 of the observations crossing Korolev (Figure 22). Orbits were excluded from mapping based on data quality, orientation of the observation, and conflicts with surface clutter.

A fundamental complication with interpreting orbital radar sounding data is off-nadir surface echoes (clutter). Rimmed crater deposits are particularly difficult due to their size and shape. Reflections from the rims and general geometry create surface clutter at time delays where a subsurface signal is expected. To mitigate these effects,

this study makes heavy use of a coherent echo simulation model developed by the University of Texas at Austin [*Choudhary et al*., in prep.]. The clutter simulation uses a topographic model to predict surface echoes and create a radargram derived only from possible surface echoes, and hence the "cluttergram" is void of subsurface signals. In order to map subsurface signals, comparisons between cluttergrams and radargrams were performed for each radar observation (Figure 23). Mapping was conducted in time delay using commercially available seismic software. The seismic software provided the ability to combine multiple radargrams into a single image while mapping. This technique allowed consistent radar reflectors mapping across all 69 orbits in this study (Figure 24). Data were then exported, depth corrected using a dielectric constant of 3.15, a value appropriate for water ice, positioned using the first return algorithm developed by the University of Texas at Austin, and converted into a geographical information science (GIS) compatible shapefile. Gridding of the data was performed using ESRI's ArcGIS software and the natural neighbor interpolation algorithm.

In addition to the stratigraphy, mesoscale climate modeling was employed to

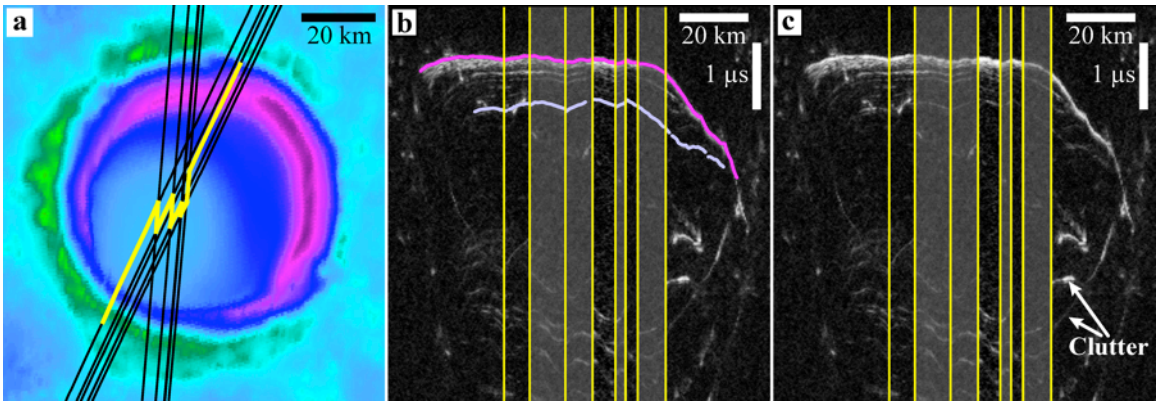

Figure 24. An example of combining crossing radargrams to consistently map radar reflectors across the Korolev ice mound. (a) Nadir track of the 9 radar orbits used for mapping is shown in bright yellow on this shaded topography map of Korolev crater. (b) Radar compilation including interpretation of both the surface and a subsurface reflector. The gridded version of this reflector is panel g in Figure 25. (c) Radar compilation without interpretation. Notice how the clutter does not often align between crossing radargrams, as expected due to changing geometry.

analyze the stability of water ice in the modern climate regime. The methodology used here was comparable to a previous radar based study analyzing Abalos Mensa [*Brothers et al*., 2013]. Paleotopography, topography representative of an empty or nearly empty Korolev crater, was created from a combination of SHARAD and Mars Orbiter Laser Altimeter (MOLA) data. SHARAD data were used over Korolev crater and the deepest visible SHARAD reflector was chosen to represent the crater's base. The GIS data shapefile for Korolev's deepest reflector was combined with MOLA shotpoint data for the crater rim and surrounding terrain.

The data were then gridded and exported for use in the Laboratoire de Météorologie Dynamique (LMD) global circulation model (GCM). The GCM was run with our constructed paleotopography in a three-part nest. The nest was used to create a high-resolution model consistent with studying a smaller landform like Korolev. The resolution of the model ranged from 30 km by 30 km to only 3.33 km by 3.33 km in the final nest. The area of Korolev crater is approximately 5300 km^2, so our final nest gives approximately 477 model cells within Korolev crater.

3.3 RESULTS

SHARAD reflector mapping in Korolev crater has revealed domal reflector geometry. Perhaps more significantly, it has revealed that this geometry has not changed by any appreciable amount through time. From the base upwards, the layers have a distinct asymmetry, southward dip, and domal shape. These general mapping results are consistent with the findings of *Conway et al*. (2012) derived from optical layer mapping. While small-scale fluctuations in morphology do exist, as well as local reflector truncations, the regional reflector trend is consistent.

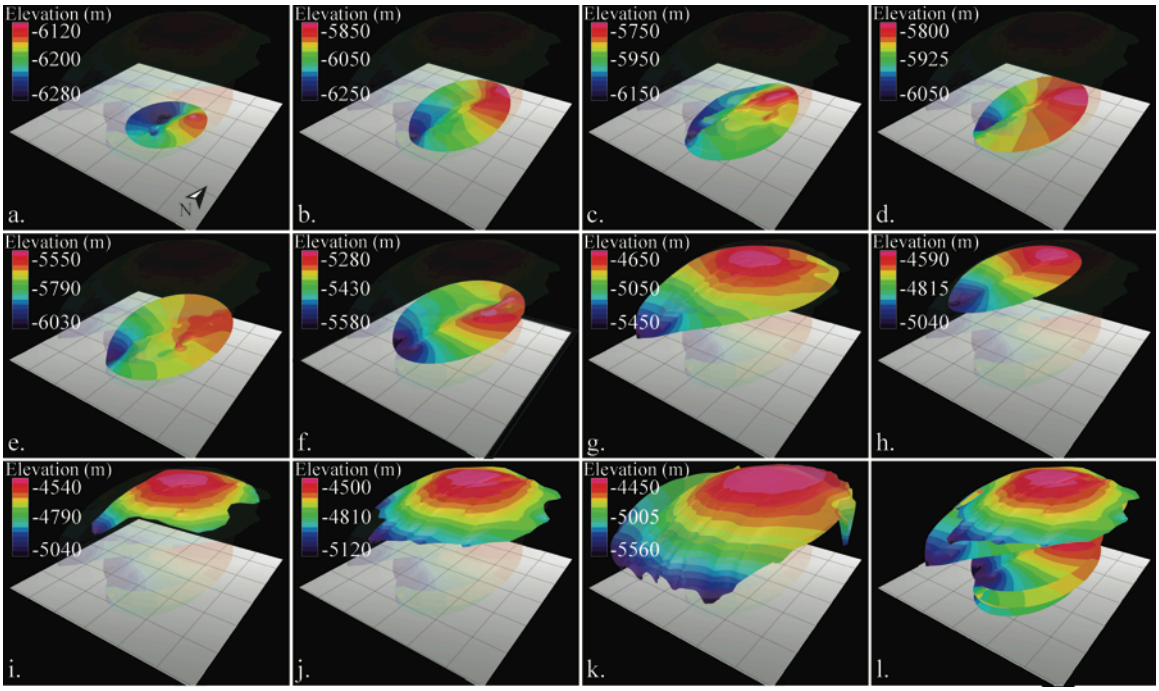

Figure 25. Gridded results for each of the 10 mapped horizons from the deepest to shallowest (a-j). Transparency for other layers is used to reveal the relative position of each gridded reflector. (k) Surface of the deposit as mapped by SHARAD. (l) All mapped subsurface reflectors.

Using SHARAD mapping results, ten of Korolev's internal reflectors were gridded. While several additional reflectors exist, these ten were the most distinct and continuous, giving the highest confidence in their reconstructed morphologies (Figure 25). The chosen reflectors range from shallow to deep and are therefore representative of the entire vertical column of ice. Using a stepped volumetric calculation, this study finds a minimum ice volume of 1424 km^3 contained in Korolev. The volume approximation was done by subtracting the elevation value between adjacent reflectors, upper reflector minus lower, and using only their overlapping region to approximate volume. As lower reflectors generally span less area, this stepped calculation is under estimating ice volume. Off nadir clutter prevents reflector mapping adjacent to the crater wall and attenuation or scattering of the radar signal prevents definitive mapping of the crater base (discussed below).

While our mapped reflectors do span the entire column of Korolev's ice, reflector spacing is variable. There is a high density of reflectors very near the surface to a depth of approximately 250 meters. However, directly below this reflector-dense region is a zone with very few to no reflectors (Figure 23). The thickness of this reflector-free region can reach upwards of 550 meters. Following the reflector-free zone we enter another zone of dense radar reflectors, which is greater than 100 meters of thickness. This general reflector pattern is repeated, creating three to four packages of material with varying thickness. A similar pattern has been found in the nearby NPLD of Planum Boreum [*Phillips et al*., 2008]. It is important to note the variability of reflector-free zones both at Korolev and over Planum Boreum. These regions are not consistently reflector free, but instead reflector dim. Radargrams will often show variability in this zone even when they are processed with the same parameters and nearly identical ground tracks. While the lack of strong reflectors is likely a material property, it is also very

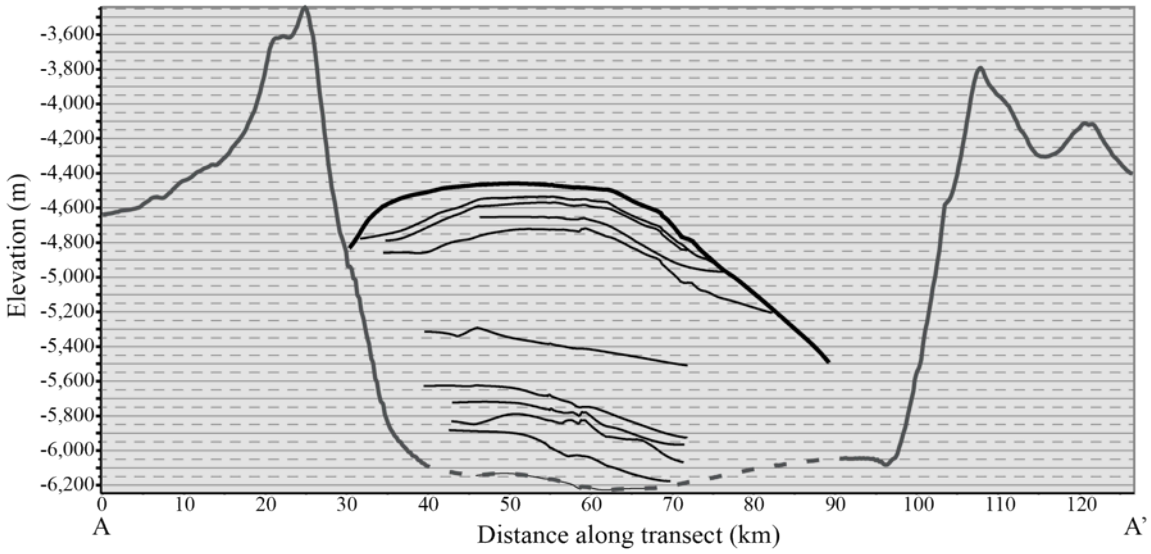

Figure 26. Transect across the gridded reflectors from A-A' in **Figure 22**. The bottom of the crater is a gridded result using our deepest SHARAD reflector but shown with a dashed line to indicate our uncertainty. Notice the reflectors truncating into the surface near 80-90 km transect distance. Additionally, all reflectors are dipping southeast with a maximum elevation shifted north of the crater's center.

dependent on signal to noise ratios (i.e, the detectability of possible weak reflectors), making this a qualitative observation.

Mapped reflectors in Korolev have consistent morphology, with a dominant southern dip. The magnitude of dip does change but the orientation remains consistent. In addition, the reflectors have a distinct asymmetry with thicker material on the north-facing slope and less on the south-facing (Figure 26). All mapped reflectors, except the hypothesized base, have a roughly domal shape. The deepest mapped reflector is nearly flat with only 0.5° mean slope. This reflector is approximately 1.8 km deep and is used as our approximated crater bottom. While we refer to this feature as the crater bottom, it would be inaccurate to use this number as a pristine crater depth and compare our number to estimates derived from depth to diameter ratios. While our base does represent the bottom of the ice deposit, it likely does not represent the base of a sediment-free Korolev. If Korolev's ice is young, less than 5 million years old, the crater has likely been exposed for a great deal of time, ample time for significant infilling, especially given its location near the circumpolar dune fields. Being both discontinuous and faint, our deepest reflector has limited mapping coverage and was only identified in 8 of the 69 observations used for this study.

The results from atmospheric modeling with an empty Korolev crater indicate that ice is stable within Korolev crater even during the warm summer months. At L_s 81 the maximum temperature at Korolev is under 240° K while the surface pressure remains near 1000 Pascals. The modeled overnight temperatures drop significantly, reaching 205° K. At maximum temperature time step the nearby terrain is approximately 25° warmer than the crater's bottom (Figure 27). Additionally, in the highest resolution model nest, the difference in temperature from crater wall to crater floor can exceed 10° K.

3.4 DISCUSSION

Reflector geometry can be used to assess the two hypotheses for the origin of ice in Korolev crater. If the ice was originally part of a regional ice sheet formed during a previous glacial regime, we would expect the internal reflectors to either continue laterally across the crater with very little dip or possibly be concave upward as ice gradually filled the depression, or as the result of large-scale flow, as found with terrestrial ice sheets [*Robin et al*., 1969; *Pattyn et al*., 2008]. However, the reflector geometry in Korolev neither mimics hypothesized basal topography nor continues unperturbed laterally across the crater. The topography instead forms a mounded deposit offset north from the crater's center (Figure 25 and Figure 26).

While the domed deposit alone is insufficient to disprove localized deposition during an ancient regime widespread ice regime, it does indicate that the processes controlling accumulation of ice in Korolev are locally derived. If the ice were part of an ancient regime one would expect unconformities consistent with those found within the

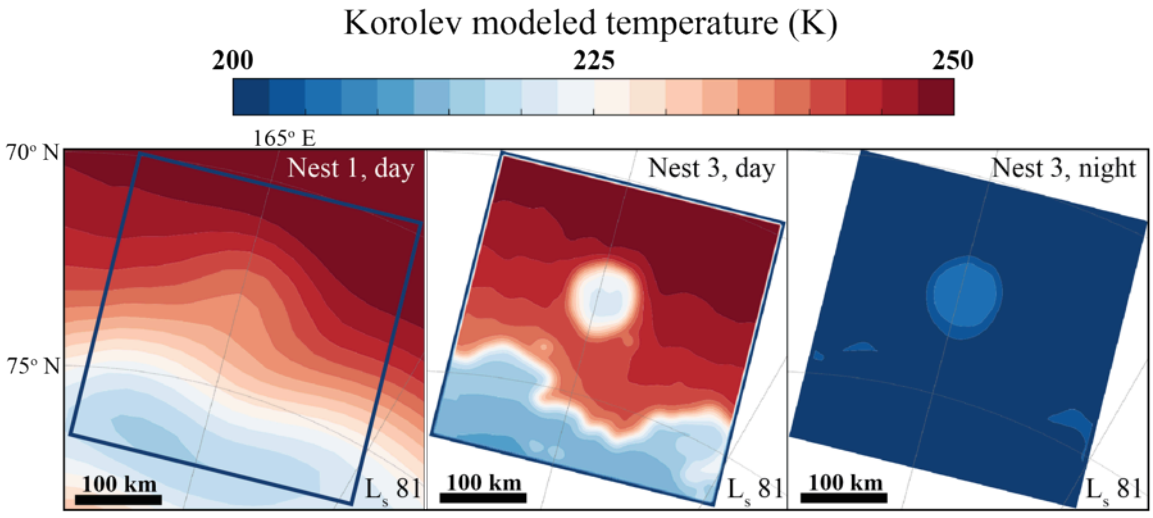

Figure 27. Modeled temperatures for Korolev crater generated by a 3-part, nested global circulation and mesoscale atmospheric model. The coarsest resolution, nest 1, barely shows the impact of Korolev on surface temperatures while the higher resolution nest 3 clearly shows Korolev and the relatively low internal temperature. The position of nest 3 is given by the dark blue box on nest 1. These results are for Ls 81, early summer.

basal unit of Planum Boreum. Exposed surface ice at the Mars' north pole during large obliquity variation should have suffered substantial sublimation and removal. The unconformity separating the Hesperian rupes unit from overlying Amazonian cavi unit and NPLD [*Tanaka et al*., 2008] should therefore also be evident in Korolev. As this event removed hundreds of meters of ice and sand on Planum Boreum, we expect to find a comparatively large unconformity at Korolev. In addition to reflector truncation, this epoch likely mobilized a great deal of sediment, some of which should have been deposited in Korolev, creating an easily observed reflector unconformity. No analyzed radargrams to date have shown a large-scale unconformity in Korolev crater. The only observed reflector unconformities in Korolev are in the upper 500 meters and constrained to the southern edge. For these reasons, we believe that ancient or Hesperian ice is inconsistent with our observations of Korolev's central mound.

The depositional offset and domed reflector shape support the second hypothesis, that Korolev's central mound was formed by in-place deposition, a finding consistent with optical layer mapping results [*Conway et al*., 2012]. However, in-place deposition does not resolve the timing for ice deposition. While our results help confirm that Korolev's material was not sourced from a regional ice sheet extending from the pole, the timing of localized deposition still remains unknown. Therefore, ancient ice forming in a colder regime is still possible. Further analysis and comparison of the stratigraphy of the NPLD and Korolev crater ice deposits, however, helps to constrain timing on Korolev ice deposition.

As mentioned in the results, the radar reflectors do not have regular vertical spacing. In fact, the reflectors can best be approximated as stepped packages of reflector-dense and reflector-sparse zones. There are three such packages of material that share this pattern with possibly a fourth very near the base of Korolev (Figure 28). This

qualitative reflector trend closely follows the observed reflector density variations for the NPLD [*Phillips et al*., 2008].

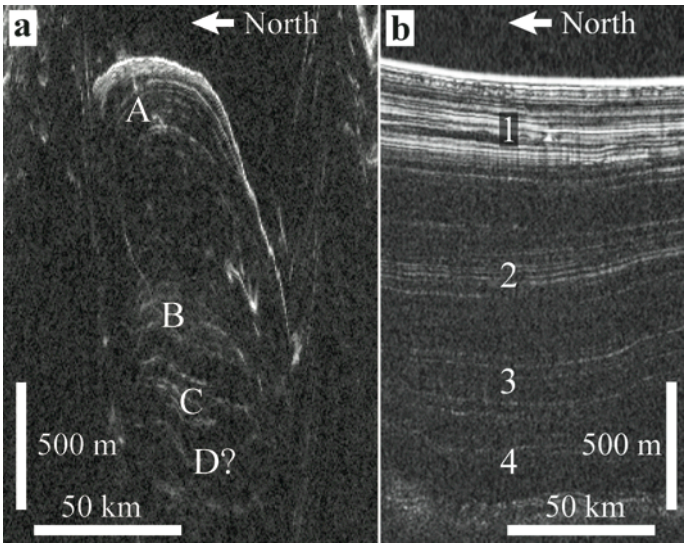

Figure 28. A comparison of radar reflector packaging in Korolev and Planum Boreum. Location is shown on **Figure 22**. (a) Korolev crater radargram 554201000. Three packages of reflector dense and reflector sparse material are present with a tentative fourth package near the base. (b) Radargram 529701000 with NPLD reflector packages as mapped by Phillips et al. (2008).

The reflectors in Korolev share additional similarities to those of the NPLD. The uppermost section of ice has the highest reflector density and within these dense reflectors exist unconformities. The unconformities are truncations of radar reflectors as pinchouts, downlap, or angular unconformities. Both Korolev crater and the NPLD share these shallow unconformities [*Tanaka*, 2005; *Tanaka et al*., 2008]. In addition to similar reflector density and stratigraphic patterns, the overall thickness of Korolev's ice is comparable to that of the NPLD. The maximum thickness at Korolev is just over 1.8 km while the maximum thickness of the NPLD is approximately 2.3 km [*Brothers and Holt*, 2015]. The maximum thickness of the NPLD ice may be greater than Korolev but the average NPLD thickness is only 1.1 km with a standard deviation of 540 m. This means that the upper thickness range for the NPLD, one standard deviation above the mean, is still below the maximum thickness at Korolev. The similarity of each deposit's thickness, reflector packaging and unconformity relationships supports a shared genetic relationship between the NPLD and Korolev's ice. Therefore, stratigraphic

similarity between the deposits in Korolev and the ice of the NPLD suggests, that it is likely that ice was deposited contemporaneously in both locations.

While similar stratigraphic architecture suggests coeval deposition of the deposits in Korolev and the NPLD, it does not address previous results suggesting that ice should be unstable in Korolev and therefore must be a relict deposit. Unlike at Korolev, timing for deposition of the NPLD has been constrained by global climate modeling [*Levrard et al*., 2007; *Greve et al*., 2010] and orbital parameters, chiefly obliquity [*Laskar et al*., 2004]. These results indicate that the ice in the NPLD can be no older than 5 million years and is likely only 4 million years old [*Greve et al*., 2010]. As our data provide evidence for in-place deposition of Korolev's ice, linking the deposit to the polar layered deposits would alleviate a major uncertainty concerning the timing of its genesis. We therefore modeled the atmospheric and surface conditions at Korolev to assess the stability of water ice in the current regime. Unstable conditions would indicate that Korolev's ice is likely different from the NPLD where we believe deposition is still occurring. These modeling results are for current martian conditions and do not represent the variability of the past 5 Myr, thus they are only useful as a qualitative analysis of relative stability.

Our modeling found that without high-resolution nested model runs of Korolev crater, the ice is predicted to be unstable. However, at the resolution of our final nest, 3.33 km by 3.33 km, stable conditions are modeled for L_s 81 within Korolev crater. Modeling done using the coarsest resolution estimated temperatures above 240° K at the crater's midpoint. The middle nest, 10 by 10 km, modeled the temperature as 225° K while the highest resolution nest modeled the temperatures at 222° K. The change of nearly 20° K in estimated temperatures is more than enough to account for prior claims of ice instability at Korolev crater with modern obliquity and climate. Instead, we find the

model results support stable ice at Korolev crater in the modern regime. Korolev crater is a small anomalous feature in Thermal Emission Spectrometer and Thermal Emission Imaging System data [*Kieffer and Titus*, 2001; *Armstrong et al*., 2005], it is therefore consistent that this feature requires high resolution modeling for temperature prediction. The albedo, lower elevation, and crater rim shading likely all contribute to lower temperatures within Korolev.

3.5 CONCLUSIONS

Korolev crater's central mound is a 1.8 km thick domed water-ice deposit. Reflector geometry in the deposit remains consistent with very little change through time. This suggests that the conditions for ice deposition remained stable as the deposit grew in place. SHARAD-derived reflector geometry within Korolev crater supports the claim for in-place deposition of the central mound; this deposit was not part of a regional ice sheet that has since been eroded. Additionally, modeling results indicate that the current climate regime can support ice at Korolev crater during summer; therefore, it is not necessary for the ice to be a remnant of previous climatic conditions.

This work also finds that Korolev's central deposit is likely coeval to Planum Boreum's NPLD. Similar thickness, stratigraphic relationships, and radar packaging support our hypothesis that these two deposits are likely genetically related and formed during the same time period. Furthermore, the striking similarity of radar reflectors between Korolev and the NPLD lends credence to early work suggesting that the polar layered deposits record regional climatic conditions [*Cutts and Lewis*, 1982; *Laskar et al*., 2002]. This work provides evidence that the climatic signal responsible for the NPLD is widespread and not limited to Planum Boreum. The same signal preserved in

Planum Boreum is likely also recorded in Korolev's central mound. This work hypothesizes a link between circumpolar depositional features and Mars' NPLD, it indicates that same signal was preserved by these 600 km separated deposits. Martian polar climate can best be deciphered through a unified study of Planum Boreum and circumpolar ice features, a study made possible with orbital radar sounding.

CONCLUSION

The use of orbital sounding radar results has enabled this new morphologic and stratigraphic study of Planum Boreum and nearby deposits. While at first glance our mapping results seem to indicate variability where homogeneity was once assumed, the variability itself appears consistent. The reentrant-like features, as well as the irregular high and its associated trough, can be thoroughly explained using known aeolian processes. For simplicity, our BU hypothesis begins with a homogenous mound of sand and ice. However, homogeneity as shown by this work is unlikely and initial inhomogeneity could further strengthen our formation scenarios. Where we require impacts into the BU to create armored and erosionally resistant material, we could instead have resistant BU material and no longer require impact ejecta armoring. Given sufficient time and wind the basal unit deposit developed its modern morphology with distinct reentrants and complex topography.

This work also finds that the morphology of the martian BU as mapped by SHARAD does not support claims for polar water ice melting scenarios. While one cannot conclusively negate melting, there exist no obvious features in the martian BU to support its role in the evolution of the polar layered deposits and north pole ice. Therefore, this study concludes that the processes observed on the north pole of Mars today, such as avalanching [*Herkenhoff et al.*, 2007; *Russell et al.*, 2008], wind driven erosion [*Smith et al.*, 2013], grain saltation and transport to the polar erg [*Byrne and Murray*, 2002; *Tanaka et al.*, 2008; *Kocurek and Ewing*, 2012], and sublimation of icy

material [*Ivanov and Muhleman*, 2000; *Dundas and Byrne*, 2010] are the primary processes responsible for the evolution of the polar cap following emplacement of the planar-laminated rupes unit.

An extension of the BU work was conducted at a proximal and arguably younger ice deposit, Abalos Mensa. As Abalos Mensa has been speculated to contain both rupes unit and cavi unit, we analyzed its stratigraphy and tested formation scenarios [*Fishbaugh and Head*, 2005; *Hovius et al.*, 2008; *Tanaka et al.*, 2008; *Warner and Farmer*, 2008] against radar reflectors and optical layering. With the understanding derived from the BU study, we were able to formulate a new hypothesis for the formation of Abalos Mensa. The hypothesized scenario used only wind and paleotopography to construct Abalos Mensa. Collaborative wind modeling work was qualitatively able to support this aeolian formation hypothesis. Once more, the results provided something unexpected. Winds in the ancient, pre-Abalos Mensa and post-Rupes Tenuis scarp period, are different enough from the modern to allow in-situ formation of Abalos Mensa (Figure 20 and Figure 21).

With SHARAD data we have been able to emphasize the impact of winds on polar ice deposits to simplify polar evolution assumptions. Our analysis has unified seemingly disparate features. As the ice and sand of Planum Boreum have been shown dominantly aeolian, the nearby landform Abalos Mensa also aeolian, we analyzed one additional deposit farther removed from the north pole. The transition away from Planum Boreum investigates claims for a more expansive ancient ice cap, and tests formation scenarios and accompanying stratigraphic signature in additional regions. If icy stratigraphy preserves a climatic signal, a regional atmospheric signal should also be preserved in circumpolar deposits. Locally impacted processes such as sublimation wind

influenced ablation are less likely to be comparable in circumpolar deposits and Planum Boreum.

This study's analysis of Korolev crater indicated once more in-situ deposition of ice material consistent with the findings of *Conway et al*. (2012). In addition, we showed that the gross properties of the radar signal, such as the concentration of reflections, were very similar between the NPLD and Korolev. We find that the ice in Korolev crater contains a similar or perhaps the same climate signal as the nearby NPLD. This finding is fundamental for Mars' polar science, as it indicates that the circumpolar deposits can in fact be used as climate proxies for Mars' north pole. Additionally, this finding supports coeval deposition of Korolev ice and the NPLD. Therefore, this circumpolar ice is likely not an ancient feature but instead less than 5 million years old [*Greve et al*., 2010].

The unification of the results presented in this dissertation marks a transition for Mars' polar science. Planum Boreum and the circumpolar deposits need to be analyzed together within an aeolian framework. While modeling results have indicated that various processes can account for both the general morphology and stratigraphy of the polar layered deposits [*Ivanov and Muhleman*, 2000; *Greve et al*., 2010; *Hvidberg et al*., 2012], observations [*Howard*, 2000] and data lend credence to the notion that wind related processes should be of primary focus. Additionally, the findings in Korolev support the idea that latitude-based models are insufficient; topography needs to be incorporated for accurate prediction of ice deposition.

The study presented here began at the oldest ice deposit, nearly centered on Mars' north pole and transitioned to circumpolar features. The results indicate circumpolar deposits and Planum Boreum and intimately related; their stratigraphy and morphology are comparable. We hypothesize that this trend will continue in additional circumpolar features, as we see no reason that it should be limited to the two features analyzed in this

dissertation. Future polar science can lean on this finding to predict via modeling and further analyze the stratigraphy of circumpolar ice deposits, as new data or techniques become available. This research provides additional modeling constraints for attempts to reconstruct Planum Boreum's climate and ice deposits. Korolev, Abalos Mensa, and Planum Boreum have similar yet locally influenced stratigraphy, their ice appears intimately linked to regional parameters. We determined that wind, with related ablation, deposition and temperature, appears sufficient to control ice deposition on Mars' north pole. This study offers a method for analyzing local ice deposition while incorporating results into a more complete Mars' north pole framework.

Appendix A: Matlab Dielectric Script

```
%Script to read in horizon file with surface data and subsurface
%data, the data is then differenced to get a time delay and corrected with
%varying permitivity values
clear all

c=299792458;  %speed of light in m/s
E=3.15;       %permittivity value

%sample_LM=2*10^-3;
%sample_Real=.1746*10^-9;

%read in all the data from text files, trace is column 1, time is column 2
srf_all=importdata('AbalosSurf.txt');
srf_data=[srf_all.data(:,1),srf_all.data(:,2)];
srf_data_time=nan(max(srf_data(:,1)),1);
time_step=1;
   for i=min(srf_data(:,1)):max(srf_data(:,1));
      srf_data_time(i,1)=srf_data(time_step,2);
      time_step=time_step + 1;
   end

base_all=importdata('AbalosBase.txt');
base_data=[base_all.data(:,1), base_all.data(:,2)];
base_data_time=nan(max(srf_data(:,1)),1);
time_step=1;
   for i=min(base_data(:,1)):max(base_data(:,1));
      base_data_time(i,1)=base_data(time_step,2);
      time_step=time_step + 1;
   end

abalos_bu1_all=importdata('abalos_bu1.txt');
abalos_bu1_data=[abalos_bu1_all.data(:,1), abalos_bu1_all.data(:,2)];
abalos_bu1_data_time=nan(max(srf_data(:,1)),1);
time_step=1;
   for i=min(abalos_bu1_data(:,1)):max(abalos_bu1_data(:,1));
      abalos_bu1_data_time(i,1)=abalos_bu1_data(time_step,2);
      time_step=time_step + 1;
   end
```

```
abalos2_all=importdata('abalos2.txt');
abalos2_data=[abalos2_all.data(:,1), abalos2_all.data(:,2)];
abalos2_data_time=nan(max(srf_data(:,1)),1);
time_step=1;
   for i=min(abalos2_data(:,1)):max(abalos2_data(:,1));
      abalos2_data_time(i,1)=abalos2_data(time_step,2);
      time_step=time_step + 1;
   end

abalos3_all=importdata('abalos3.txt');
abalos3_data=[abalos3_all.data(:,1), abalos3_all.data(:,2)];
abalos3_data_time=nan(max(srf_data(:,1)),1);
time_step=1;
   for i=min(abalos3_data(:,1)):max(abalos3_data(:,1));
      abalos3_data_time(i,1)=abalos3_data(time_step,2);
      time_step=time_step + 1;
   end

abalos4_all=importdata('abalos4.txt');
abalos4_data=[abalos4_all.data(:,1), abalos4_all.data(:,2)];
abalos4_data_time=nan(max(srf_data(:,1)),1);
time_step=1;
   for i=min(abalos4_data(:,1)):max(abalos4_data(:,1));
      abalos4_data_time(i,1)=abalos4_data(time_step,2);
      time_step=time_step + 1;
   end

abalos5_all=importdata('abalos5.txt');
abalos5_data=[abalos5_all.data(:,1), abalos5_all.data(:,2)];
abalos5_data_time=nan(max(srf_data(:,1)),1);
time_step=1;
   for i=min(abalos5_data(:,1)):max(abalos5_data(:,1));
      abalos5_data_time(i,1)=abalos5_data(time_step,2);
      time_step=time_step + 1;
   end

abalos6_all=importdata('abalos6.txt');
abalos6_data=[abalos6_all.data(:,1), abalos6_all.data(:,2)];
abalos6_data_time=nan(max(srf_data(:,1)),1);
time_step=1;
   for i=min(abalos6_data(:,1)):max(abalos6_data(:,1));
      abalos6_data_time(i,1)=abalos6_data(time_step,2);
      time_step=time_step + 1;
```

```
    end

%The find statement allows me to find the position in the matrix where the
%start of one field tr_min matches up with the surface, at which position
%in the matrix
%All subsurface data will start at 1, but the surface pick won't

srf_ele=nan(max(srf_data(:,1)),1);
base_ele=nan(max(srf_data(:,1)),1);
base_diff=nan(max(srf_data(:,1)),1);
abalos2_diff=nan(max(srf_data(:,1)),1);
abalos3_diff=nan(max(srf_data(:,1)),1);
abalos4_diff=nan(max(srf_data(:,1)),1);
abalos5_diff=nan(max(srf_data(:,1)),1);
abalos6_diff=nan(max(srf_data(:,1)),1);

%Calculate the surface pick elevation in meters, force it to start at 0
s_step=1;
for s=min(srf_data(:,1)):max(srf_data(:,1));
    srf_ele(s,1)= -1*(c*srf_data(s_step,2)*10^-8/(2*sqrt(1)) - 17222); %made data
zero'd and visually correct "
    s_step=s_step+1;
end

%Calculate the time differences for each surface
%Now calculate differences, this puts us with a (-) time

for i=1:size(srf_data_time,1);
    if base_data_time(i,1)==NaN
        continue
    end
    base_diff(i,1)=srf_data_time(i,1)- base_data_time(i,1);
end

for i=1:size(srf_data_time,1);
    if abalos_bu1_data_time(i,1)==NaN
        continue
    end
    abalos_bu1_diff(i,1)=srf_data_time(i,1)- abalos_bu1_data_time(i,1);
end

for i=1:size(srf_data_time,1);
    if abalos2_data_time(i,1)==NaN
```

```
      continue
   end
   abalos2_diff(i,1)=srf_data_time(i,1)- abalos2_data_time(i,1);
end

for i=1:size(srf_data_time,1);
   if abalos3_data_time(i,1)==NaN
      continue
   end
   abalos3_diff(i,1)=srf_data_time(i,1)- abalos3_data_time(i,1);
end

for i=1:size(srf_data_time,1);
   if abalos4_data_time(i,1)==NaN
      continue
   end
   abalos4_diff(i,1)=srf_data_time(i,1)- abalos4_data_time(i,1);
end

for i=1:size(srf_data_time,1);
   if abalos5_data_time(i,1)==NaN
      continue
   end
   abalos5_diff(i,1)=srf_data_time(i,1)- abalos5_data_time(i,1);
end

for i=1:size(srf_data_time,1);
   if abalos6_data_time(i,1)==NaN
      continue
   end
   abalos6_diff(i,1)=srf_data_time(i,1)- abalos6_data_time(i,1);
end

%Begin depth conversion process, all times are in landmark milliseconds
%where 1 LM time unit is really 10^-8 seconds, all these units are in
%two way travel time (need to divide by two for depth)

for E=[1:10]
   for k=1:size(base_diff,1)
      if base_diff(k,1) == NaN
         continue
      end
      base_depth(k,E)=(base_diff(k,1)*10^-8)/2*c/sqrt(E);
```

```
      base_ele(k,E)= base_depth(k,E) + srf_ele(k,1);
   end
end
for E=[1:10]
   for k=1:size(abalos_bu1_diff,1)
      if abalos_bu1_diff(k,1) == NaN
         continue
      end
      abalos_bu1_depth(k,E)=(abalos_bu1_diff(k,1)*10^-8)/2*c/sqrt(E);
      abalos_bu1_ele(k,E)= abalos_bu1_depth(k,E) + srf_ele(k,1);
   end
end
for E=[1:10]
   for k=1:size(abalos2_diff,1)
      if abalos2_diff(k,1) == NaN
         continue
      end
      abalos2_depth(k,E)=(abalos2_diff(k,1)*10^-8)/2*c/sqrt(E);
      abalos2_ele(k,E)= abalos2_depth(k,E) + srf_ele(k,1);
   end
end
for E=[1:10]
   for k=1:size(abalos3_diff,1)
      if abalos3_diff(k,1) == NaN
         continue
      end
      abalos3_depth(k,E)=(abalos3_diff(k,1)*10^-8)/2*c/sqrt(E);
      abalos3_ele(k,E)= abalos3_depth(k,E) + srf_ele(k,1);
   end
end
for E=[1:10]
   for k=1:size(abalos4_diff,1)
      if abalos4_diff(k,1) == NaN
         continue
      end
      abalos4_depth(k,E)=(abalos4_diff(k,1)*10^-8)/2*c/sqrt(E);
      abalos4_ele(k,E)= abalos4_depth(k,E) + srf_ele(k,1);
   end
end
for E=[1:10]
   for k=1:size(abalos5_diff,1)
      if abalos5_diff(k,1) == NaN
         continue
```

```
        end
        abalos5_depth(k,E)=(abalos5_diff(k,1)*10^-8)/2*c/sqrt(E);
        abalos5_ele(k,E)= abalos5_depth(k,E) + srf_ele(k,1);
    end
end
for E=[1:10]
    for k=1:size(abalos6_diff,1)
        if abalos6_diff(k,1) == NaN
            continue
        end
        abalos6_depth(k,E)=(abalos6_diff(k,1)*10^-8)/2*c/sqrt(E);
        abalos6_ele(k,E)= abalos6_depth(k,E) + srf_ele(k,1);
    end
end
%plot(t_min:t_max,depth(t_min:t_max,1))

figure
plot(srf_ele, 'k')
xlabel('Trace','FontSize', 16)
ylabel('Height (m)','FontSize', 16)
hold on
plot(base_ele(:,3), 'b')
plot(abalos_bu1_ele(:,3), 'b')
plot(abalos2_ele(:,3), 'b')
plot(abalos3_ele(:,3), 'b')
plot(abalos4_ele(:,3), 'b')
plot(abalos5_ele(:,3), 'b')
plot(abalos6_ele(:,3), 'b')
%hold off
%figure
%plot(srf_ele, 'k')
%xlabel('Trace','FontSize', 16)
%ylabel('Meters','FontSize', 16)
%hold on
plot(base_ele(:,5), 'm')
plot(abalos_bu1_ele(:,8), 'm')
plot(abalos2_ele(:,8), 'm')
plot(abalos3_ele(:,8), 'm')
plot(abalos4_ele(:,8), 'm')
plot(abalos5_ele(:,8), 'm')
plot(abalos6_ele(:,8), 'm')
```

Bibliography

Appéré, T., B. Schmitt, Y. Langevin, A. Spiga, S. Douté, A. Pommerol, F. Forget, B. Gondet, and J. P. Bibring (2011), Katabatic Winds, Geysers and Seasonal Water Frost During Northern Spring on Mars, *LPI Contrib.*, *1323*, 6037.

Armstrong, J. C., T. N. Titus, and H. H. Kieffer (2005), Evidence for subsurface water ice in Korolev crater, Mars, *Icarus*, *174*(2), 360–372, doi:10.1016/j.icarus.2004.10.032.

Arvidson, R. E., M. Coradini, A. Carusi, A. Coradini, M. Fulchignoni, C. Federico, R. Funiciello, and M. Salomone (1976), Latitudinal variation of wind erosion of crater ejecta deposits on Mars, *Icarus*, *27*(4), 503–516, doi:10.1016/0019-1035(76)90166-4.

Brothers, T. C., and J. W. Holt (2015), Planum Boreum basal unit topography: irregularities and insight from SHARAD, *Icarus*, ?

Brothers, T. C., J. W. Holt, and A. Spiga (2013), Orbital radar, imagery, and atmospheric modeling reveal an aeolian origin for Abalos Mensa, Mars, *Geophys. Res. Lett.*, *40*(7), 1334–1339, doi:10.1002/grl.50293.

Byrne, S., and B. C. Murray (2002), North polar stratigraphy and the paleo-erg of Mars, *J. Geophys. Res.*, *107*(E6), 11–1, doi:10.1029/2001JE001615.

Campbell, B. A., N. E. Putzig, L. M. Carter, and R. J. Phillips (2011), Autofocus Correction of Phase Distortion Effects on SHARAD Echoes, *IEEE Geosci. Remote Sens. Lett.*, *8*(5), 939–942, doi:10.1109/LGRS.2011.2143692.

Carter, L. M. et al. (2009), Shallow radar (SHARAD) sounding observations of the Medusae Fossae Formation, Mars, *Icarus*, *199*(2), 295–302, doi:10.1016/j.icarus.2008.10.007.

Choudhary, P., J. W. Holt, S. D. Kempf, and D. A. Young (in prep.), Surface clutter and echo location analysis for the interpretation of SHARAD data from Mars,

Christian, S., J. W. Holt, S. Byrne, and K. E. Fishbaugh (2013), Integrating radar stratigraphy with high resolution visible stratigraphy of the north polar layered deposits, Mars, *Icarus*, *226*(2), 1241–1251, doi:10.1016/j.icarus.2013.07.003.

Conway, S. J., N. Hovius, T. Barnie, J. Besserer, S. Le Mouélic, R. Orosei, and N. A. Read (2012), Climate-driven deposition of water ice and the formation of mounds

in craters in Mars' north polar region, *Icarus*, *220*(1), 174–193, doi:10.1016/j.icarus.2012.04.021.

Cutts, J. A. (1973), Nature and origin of layered deposits of the Martian polar regions, *J. Geophys. Res.*, *78*(20), 4231–4249, doi:10.1029/JB078i020p04231.

Cutts, J. A., and B. H. Lewis (1982), Models of climate cycles recorded in Martian polar layered deposits, *Icarus*, *50*(2–3), 216 – 244, doi:http://dx.doi.org/10.1016/0019-1035(82)90124-5.

Dundas, C. M., and S. Byrne (2010), Modeling sublimation of ice exposed by new impacts in the martian mid-latitudes, *Icarus*, *206*(2), 716 – 728, doi:http://dx.doi.org/10.1016/j.icarus.2009.09.007.

Fishbaugh, K. E., and J. W. Head (2000), North polar region of Mars: Topography of circumpolar deposits from Mars Orbiter Laser Altimeter (MOLA) data and evidence for asymmetric retreat of the polar cap, *J. Geophys. Res. Planets*, *105*(E9), 22455–22486, doi:10.1029/1999JE001230.

Fishbaugh, K. E., and J. W. Head (2002), Chasma Boreale, Mars: Topographic characterization from Mars Orbiter Laser Altimeter data and implications for mechanisms of formation, *J. Geophys. Res.*, *107*(E3), doi:10.1029/2000JE001351.

Fishbaugh, K. E., and J. W. Head (2005), Origin and characteristics of the Mars north polar basal unit and implications for polar geologic history, *Icarus*, *174*(2), 444–474, doi:10.1016/j.icarus.2004.06.021.

Garvin, J. (2000a), North Polar Region Craterforms on Mars: Geometric Characteristics from the Mars Orbiter Laser Altimeter, *Icarus*, *144*(2), 329–352, doi:10.1006/icar.1999.6298.

Garvin, J. (2000b), Topographic Evidence for Geologically Recent Near-Polar Volcanism on Mars, *Icarus*, *145*(2), 648–652, doi:10.1006/icar.2000.6409.

Greve, R., B. Grieger, and O. J. Stenzel (2010), MAIC-2, a latitudinal model for the Martian surface temperature, atmospheric water transport and surface glaciation, *Planet. Space Sci.*, *58*(6), 931–940, doi:10.1016/j.pss.2010.03.002.

Grima, C., W. Kofman, J. Mouginot, R. J. Phillips, A. Hérique, D. Biccari, R. Seu, and M. Cutigni (2009), North polar deposits of Mars: Extreme purity of the water ice, *Geophys. Res. Lett.*, *36*(3), doi:10.1029/2008GL036326.

Herkenhoff, K. E., S. Byrne, P. S. Russell, K. E. Fishbaugh, and A. S. McEwen (2007), Meter-Scale Morphology of the North Polar Region of Mars, *Science*, *317*(5845), 1711–1715, doi:10.1126/science.1143544.

Holt, J. W., M. E. Peters, S. D. Kempf, D. L. Morse, and D. D. Blankenship (2006), Echo source discrimination in single-pass airborne radar sounding data from the Dry Valleys, Antarctica: Implications for orbital sounding of Mars, *J. Geophys. Res. Planets*, *111*(E6), doi:10.1029/2005JE002525.

Holt, J. W. et al. (2008), Radar Sounding Evidence for Buried Glaciers in the Southern Mid-Latitudes of Mars, *Science*, *322*(5905), 1235–1238, doi:10.1126/science.1164246.

Holt, J. W., K. E. Fishbaugh, S. Byrne, S. Christian, K. Tanaka, P. S. Russell, K. E. Herkenhoff, A. Safaeinili, N. E. Putzig, and R. J. Phillips (2010), The construction of Chasma Boreale on Mars, *Nature*, *465*(7297), 446–449, doi:10.1038/nature09050.

Hovius, N., A. Leacox, and J. Turowski (2008), Recent volcano–ice interaction and outburst flooding in a Mars polar cap re-entrant, *Icarus*, *197*(1), 24–38, doi:10.1016/j.icarus.2008.04.020.

Howard, A. D. (2000), The Role of Eolian Processes in Forming Surface Features of the Martian Polar Layered Deposits, *Icarus*, *144*(2), 267–288, doi:10.1006/icar.1999.6305.

Howard, A. D., J. A. Cutts, and K. R. Blasius (1982), Stratigraphic Relationships within Martian Polar Cap Deposits, *Icarus*, *50*, 161–215.

Hvidberg, C. S., K. E. Fishbaugh, M. Winstrup, A. Svensson, S. Byrne, and K. E. Herkenhoff (2012), Reading the climate record of the martian polar layered deposits, *Icarus*, *221*(1), 405 – 419, doi:http://dx.doi.org/10.1016/j.icarus.2012.08.009.

Ivanov, A. B., and D. O. Muhleman (2000), The Role of Sublimation for the Formation of the Northern Ice Cap: Results from the Mars Orbiter Laser Altimeter, *Icarus*, *144*(2), 436 – 448, doi:http://dx.doi.org/10.1006/icar.1999.6304.

Kieffer, H. H., and T. N. Titus (2001), {TES} Mapping of Mars' North Seasonal Cap, *Icarus*, *154*(1), 162 – 180, doi:http://dx.doi.org/10.1006/icar.2001.6670.

Kneissl, T., S. Van Gasselt, L. Wendt, C. Gross, and G. Neukum (2011), Layering and degradation of the Rupes Tenuis unit, Mars - a structural analysis south of

Chasma Boreale, *Geol. Soc. Lond. Spec. Publ.*, *356*(1), 257–279, doi:10.1144/SP356.13.

Kocurek, G., and R. C. Ewing (2012), Source-To-Sink: An Earth/Mars Comparison of Boundary Conditions for Eolian Dune Systems, in *Sedimentary Geology of Mars*, vol. 102, pp. 151–168, Society for Sedimentary Geology.

Kolb, E. J., and K. L. Tanaka (2006), Accumulation and erosion of south polar layered deposits in the Promethei Lingula region, Planum Australe, Mars, *Int. J. Mars Sci. Explor.*, 1–9, doi:doi:10.1555/mars.2006.0001.

Laskar, J., B. Levrard, and J. F. Mustard (2002), Orbital forcing of the martian polar layered deposits, *Nature*, *419*(6905), 375–377, doi:10.1038/nature01066.

Laskar, J., A. C. M. Correia, M. Gastineau, F. Joutel, B. Levrard, and P. Robutel (2004), Long term evolution and chaotic diffusion of the insolation quantities of Mars, *Icarus*, *170*(2), 343–364, doi:10.1016/j.icarus.2004.04.005.

Lauro, S. E., E. Mattei, F. Soldovieri, E. Pettinelli, R. Orosei, and G. Vannaroni (2012), Dielectric constant estimation of the uppermost Basal Unit layer in the martian Boreales Scopuli region, *Icarus*, *219*(1), 458–467, doi:10.1016/j.icarus.2012.03.011.

Levrard, B., F. Forget, F. Montmessin, and J. Laskar (2004), Recent ice-rich deposits formed at high latitudes on Mars by sublimation of unstable equatorial ice during low obliquity, *Nature*, *431*(7012), 1072–1075, doi:10.1038/nature03055.

Levrard, B., F. Forget, F. Montmessin, and J. Laskar (2007), Recent formation and evolution of northern Martian polar layered deposits as inferred from a Global Climate Model, *J. Geophys. Res.*, *112*(E6), doi:10.1029/2006JE002772.

Madeleine, J.-B., F. Forget, J. W. Head, B. Levrard, F. Montmessin, and E. Millour (2009), Amazonian northern mid-latitude glaciation on Mars: A proposed climate scenario, *Icarus*, *203*(2), 390–405, doi:10.1016/j.icarus.2009.04.037.

Malin, M. C., and K. S. Edgett (2001), Mars Global Surveyor Mars Orbiter Camera: Interplanetary cruise through primary mission, *J. Geophys. Res.*, *106*(E10), 23,429–23,570.

Malin, M. C. et al. (2007), Context Camera Investigation on board the Mars Reconnaissance Orbiter, *J. Geophys. Res. Planets*, *112*(E5), doi:10.1029/2006JE002808.

Massé, M., O. Bourgeois, S. L. Mouélic, C. Verpoorter, A. Spiga, and L. L. Deit (2012), Wide distribution and glacial origin of polar gypsum on Mars, *Earth Planet. Sci. Lett.*, *317–318*(0), 44 – 55, doi:http://dx.doi.org/10.1016/j.epsl.2011.11.035.

McEwen, A. S. et al. (2007), Mars Reconnaissance Orbiter's High Resolution Imaging Science Experiment (HiRISE), *J. Geophys. Res. Planets*, *112*(E5), doi:10.1029/2005JE002605.

Moore, M. W., J. W. Holt, and B. A. Campbell (2012), Internal structure of the domed deposit within Korolev Crater, Mars from radar sounding, *43rd Lunar Planet. Sci. Conf.*

Morgan, G. A., B. A. Campbell, L. M. Carter, J. J. Plaut, and R. J. Phillips (2013), 3D Reconstruction of the Source and Scale of Buried Young Flood Channels on Mars, *Science*, *340*(6132), 607–610, doi:10.1126/science.1234787.

Neukum, G., and R. Jaumann (2004), HRSC: The high resolution stereo camera of Mars Express, in *Mars Express: The Scientific Payload*, vol. 1240, pp. 17–35.

Pattyn, F. et al. (2008), Benchmark experiments for higher-order and full Stokes ice sheet models (ISMIP-HOM), *Cryosphere Discuss.*, *2*(1), 111–151.

Phillips, R. J. et al. (2008), Mars North Polar Deposits: Stratigraphy, Age, and Geodynamical Response, *Science*, *320*(5880), 1182–1185, doi:10.1126/science.1157546.

Phillips, R. J. et al. (2011), Massive CO2 Ice Deposits Sequestered in the South Polar Layered Deposits of Mars, *Science*, *332*(6031), 838–841, doi:10.1126/science.1203091.

Picardi, G., D. Biccari, R. Seu, J. Plaut, W. T. K. Johnson, R. L. Jordan, A. Safaeinili, D. A. Gurnett, R. Huff, and R. Orosei (2004), MARSIS: Mars advanced radar for subsurface and ionosphere sounding, *Mars Express Sci. Payload*, 51–69.

Putzig, N. E., R. J. Phillips, B. A. Campbell, J. W. Holt, J. J. Plaut, L. M. Carter, A. F. Egan, F. Bernardini, A. Safaeinili, and R. Seu (2009), Subsurface structure of Planum Boreum from Mars Reconnaissance Orbiter shallow radar soundings, *Icarus*, *204*(2), 443–457.

Robin, G. D. Q., S. Evans, and J. T. Bailey (1969), Interpretation of Radio Echo Sounding in Polar Ice Sheets, *Philos. Trans. R. Soc. Lond. Math. Phys. Eng. Sci.*, *265*(1166), 437–505, doi:10.1098/rsta.1969.0063.

Russell, P. et al. (2008), Seasonally active frost-dust avalanches on a north polar scarp of Mars captured by HiRISE, *Geophys. Res. Lett.*, *35*(23), n/a–n/a, doi:10.1029/2008GL035790.

Selvans, M. M., J. J. Plaut, O. Aharonson, and A. Safaeinili (2010), Internal structure of Planum Boreum, from Mars advanced radar for subsurface and ionospheric sounding data, *J. Geophys. Res. Planets 1991–2012*, *115*(E9).

Seu, R. et al. (2007), SHARAD sounding radar on the Mars Reconnaissance Orbiter, *J. Geophys. Res.*, *112*(E5), 1715–1718, doi:10.1029/2006JE002745.

Sibson, R. (1981), A brief description of natural neighbour interpolation, in *Interpreting multivariate data*, pp. 21–36, John Wiley & Sons, New York.

Smith, D. E. et al. (2001), Mars Orbiter Laser Altimeter: Experiment summary after the first year of global mapping of Mars, *J. Geophys. Res. Planets*, *106*(E10), 23689–23722, doi:10.1029/2000JE001364.

Smith, I. B., and J. W. Holt (2010), Onset and migration of spiral troughs on Mars revealed by orbital radar, *Nature*, *465*(7297), 450–453, doi:10.1038/nature09049.

Smith, I. B., and J. W. Holt (2015), Spiral Trough Diversity on the North Pole of Mars, as Seen by SHARAD, *J. Geophys. Res. Planets*, doi:10.1002/2014JE004720.

Smith, I. B., J. W. Holt, A. Spiga, A. D. Howard, and G. Parker (2013), The spiral troughs of Mars as cyclic steps, *J. Geophys. Res. Planets*, *118*(9), 1835–1857, doi:10.1002/jgre.20142.

Spiga, A., and F. Forget (2009), A new model to simulate the Martian mesoscale and microscale atmospheric circulation: Validation and first results, *J. Geophys. Res.*, *114*(E2), doi:10.1029/2008JE003242.

Spiga, A., F. Forget, J.-B. Madeleine, L. Montabone, S. R. Lewis, and E. Millour (2011a), The impact of martian mesoscale winds on surface temperature and on the determination of thermal inertia, *Icarus*, *212*(2), 504–519, doi:10.1016/j.icarus.2011.02.001.

Spiga, A., F. Forget, J.-B. Madeleine, L. Montabone, S. R. Lewis, and E. Millour (2011b), The impact of martian mesoscale winds on surface temperature and on the determination of thermal inertia, *Icarus*, *212*(2), 504–519, doi:10.1016/j.icarus.2011.02.001.

Tanaka, K., J. Rodriguez, J. Skinner, M. Bourke, C. Fortezzo, K. Herkenhoff, E. Kolb, and C. Okubo (2008), North polar region of Mars: Advances in stratigraphy,

structure, and erosional modification, *Icarus*, *196*(2), 318–358, doi:10.1016/j.icarus.2008.01.021.

Tanaka, K. L. (2005), Geology and insolation-driven climatic history of Amazonian north polar materials on Mars, *Nature*, *437*(7061), 991–994, doi:10.1038/nature04065.

Tanaka, K. L., and C. M. Fortezzo (2012), Geologic map of the north polar region of Mars, *US Geol. Surv. Sci. Investig., Map 3177*.

Tanaka, K. L., and R. K. Hayward (2008), Mars' North Circum-polar dunes: Distribution, Sources, and Migration History, *Planetar Dunes Workshop Rec. Clim. Change*, *LPI Contribution No. 1403*(Lunar and Planetary Institute, Houston), 69–70.

Warner, N. H., and J. D. Farmer (2008a), Importance of aeolian processes in the origin of the north polar chasmata, Mars, *Icarus*, *196*(2), 368 – 384, doi:http://dx.doi.org/10.1016/j.icarus.2007.08.043.

Warner, N. H., and J. D. Farmer (2008b), The origin of conical mounds at the mouth of Chasma Boreale, *J. Geophys. Res.*, *113*(E11), doi:10.1029/2007JE003028.

Zurek, R. W., and S. E. Smrekar (2007), An overview of the Mars Reconnaissance Orbiter (MRO) science mission, *J. Geophys. Res. Planets*, *112*(E5), n/a–n/a, doi:10.1029/2006JE002701.